The Hong Kong Polytechnic University

Department of Mechanical Engineering

Hybrid Passive/Active Duct Noise Control by Using Micro-perforated Plates

WANG Xiaonan

A thesis submitted in partial fulfillment of the requirements for the Degree of Doctor of Philosophy

Mar, 2013

CERTIFICATE OF ORIGINALITY

I hereby declare that this thesis is my own work and that, to the best of my knowledge and belief, it reproduces no material previously published or written, nor material that has been accepted for the award of any other degree or diploma, except where due acknowledgement has been made in the text.

(Signed)

Wang Xiaonan (Name of student)

Department of Mechanical Engineering

The Hong Kong Polytechnic University

Hong Kong, China

Mar, 2013

ABSTRACT

Mitigation of duct noise is an important and challenging research topic which finds wide applications. Our previous work led to a so-called plate silencer, consisting of an expansion chamber with two side-branch cavities covered by plates. Working in a purely reactive manner, the device can produce a wide stopband from low to medium frequencies provided the plate is extremely light and stiff, to ensure a strong reflection of acoustic sound wave upstream in the duct. However, a plate with a slightly weak bending stiffness will result in non-uniform transmission loss (TL) spectrum with narrowed stopband, which is detrimental for broadband noise control.

In this study, a hybrid passive and active silencer is proposed by following two steps. First, micro-perforation is introduced into the plate silencer. Drilled with sub-millimetre holes, the micro-perforated plate aims to elicit the sound absorption in order to compensate for the deficiency in the passband caused by the insufficient sound reflection in a certain frequency range due to weaker plate stiffness. To this end, a theoretical model, capable of dealing with the strong coupling between the vibrating micro-perforated plate and the sound fields inside the cavity and the duct, is developed. Through proper balancing between sound absorption and reflection, the plate silencer with micro-perforation provides a more flattened and uniform TL and a widened stopband by more than 20% while relaxing the harsh requirement on the

bending stiffness of the plate by about 20%. Theoretical predictions are validated by experimental data, with phenomena explained through numerical analyses.

Furthermore, piezoelectric actuator is introduced to the system of the plate silencer with micro-perforations, leading to a so-called hybrid passive and active noise control system. The aim for adding the active part is to further broaden the effective range of the plate silencer with micro-perforation to even lower frequencies. To realize the goal, an additional plate attached with piezoelectric actuators is inserted to the duct wall adjacent to the original micro-perforated plate and backed by an independent rigid cavity. A theoretical model, capable of characterizing vibro-acousto-electromechanical coupling of the entire system, is established. The hybrid system is investigated under passive and active operation modes. Numerical analyses reveal the influences of major parameters, providing guidance for the design. It is shown that the lower limit of the working range of the plate silencer with micro-perforation can be further extended to the low frequency with a reasonable control voltage under relatively simple control strategy.

PUBLICATIONS ARISING FROM THE THESIS

Journal article：

Xiaonan Wang, Yat-Sze Choy and Li Cheng. “Hybride Noise Control in a Duct Using Light Micro-perforated Plate”, J. Acoust. Soc. Am. 132(6), 3778-3787, 2012.

Conference paper：

Xiaonan Wang, Yat-Sze Choy and Li Cheng. “Hybrid Noise Control in Duct by Using Micro-Perforated Plate”, *Proceeding of Inter-noise* 2012, New York, USA.

Xiaonan Wang, Yat-Sze Choy and Li Cheng. “Hybrid Passive Noise Control on a Plate Silencer with Micro-Perforations”, The 14th Asia Pacific Vibration Conference, 2011, Hong Kong, China.

Xiaonan Wang, Yat-Sze Choy and Li Cheng. “Hybrid silencer by using micro-perforated plate with side-branch cavities”, the 164 meeting of the Acoustical Society of America, 22-26, October, 2012.

ACKNOWLEDGEMENTS

I would like to express deepest appreciation to my supervisors, Professor Cheng Li and Dr. Choy Yat-Sze for their thoughtful insight and warm encouragement to me. I thank them for giving me the opportunity to learn so many things at The Hong Kong Polytechnic University. The study will not be successful without their invaluable guidance and support.

I would also like to take this opportunity to thank Dr. Liu Yang, Yang Cheng, Xi Qiang and Hu Qi for their kind assistance and discussion during the past three years. I would also like to thank all the staff and technicians in the laboratories and offices for their supports.

Finally, I would like to thank my parents for their love and supports. Without their consideration and understanding, this journey would be too hard for me. Special thanks go to Mr. Wang Xu for his support and help during my study.

TABLE OF CONTENTS

CERTIFICATE OF ORIGINALITY ..... **I**

ABSTRACT ..... **II**

PUBLICATIONS ARISING FROM THE THESIS ..... **IV**

ACKNOWLEDGEMENTS ..... **V**

TABLE OF CONTENTS ..... **VI**

LIST OF FIGURES ..... **IX**

NOMENCLATURE ..... **XIV**

CHAPTER 1 INTRODUCTION **1**

1.1 Literature review 1

1.1.1 Passive noise control 2

1.1.2 Active noise control 9

1.1.3 Hybrid noise control 11

1.2 Motivations and objectives 14

1.3 Outline 16

CHAPTER 2 THEORETICAL STUDIES OF PLATE SILENCER WITH MICRO-PERFORATION **20**

2.1 Introduction 20

2.2 Theoretical modelling 21

2.2.1 Air-plate interaction 22

2.2.2 Fluid loading on MPP in the duct 25

2.2.3 Fluid loading on MPP in the cavity 26

2.2.4 Vibration matrix and transmission loss 27

2.3 Simulation with finite element method 29

2.3.1 Setup of the model 29

2.3.2 Comparison between the analytical and FEM results 33

2.4 Summary 33

CHAPTER 3 NUMERICAL RESULTS AND ANALYSES.....35

3.1 Introduction 35

3.2 Performance analyses.....36

3.2.1 Results of default configurations 37

3.2.2 Noise reduction mechanism 38

3.3 Analysis of the TL spectrum.....40

3.3.1 TL peaks 41

3.3.2 Absorption coefficient of the peaks.....46

3.3.3 Structural impedance 47

3.4 Optimization of TL performance.....49

3.4.1 Structural properties.....50

3.4.2 Perforation parameters.....55

3.4.3 Pressure difference 58

3.4.4 Optimal bending stiffness and perforation parameters 60

3.5 Summary.....62

CHAPTER 4 EXPERIMENTAL INVESTIGATION.....64

4.1 Introduction 64

4.2 Experimental set-up.....65

4.2.1 Two-load method.....65

4.2.2 TL measurement 67

4.3 Material investigation 71

4.4 Results and analysis 75

4.5 Summary.....79

CHAPTER 5 HYBRID PASSIVE AND ACTIVE NOISE CONTROL SYSTEM 80

5.1 Introduction 80

5.2 Modelling of the hybrid noise control system.....82

5.2.1 Plate vibration with piezoelectric actuators attached.....85

5.2.2 Working mechanism of two plates in series as a side branch in a duct 93

5.2.3 Configuration of the hybrid noise control system 98

5.3 Comparison between the analytical and FEM results 102
5.4 TL criterion 105
5.5 Parametric studies of the hybrid system in passive mode 107
5.5.1 Length 107
5.5.2 Mass 109
5.5.3 Bending stiffness 111
5.6 Optimization for the hybrid silencer in passive mode 111
5.7 Performance of the hybrid system in active mode 115
5.7.1 Control strategy 116
5.7.2 Model Truncation 118
5.7.3 Evaluation of the coupling between the first two vibration modes 120
5.7.4 Structure impedance of plate II and the driving force 125
5.8 Summary 134
CHAPTER 6 CONCLUSION AND FURTHER STUDY 136
6.1 Conclusion 136
6.2 Further study 140
APPENDIX 142
REFERENCES 147

LIST OF FIGURES

Fig.2.1 Theoretical model of the plate silencer with micro-perforation in a rectangular cavity. 22

Fig.2.2 Configuration of plate silencer for FEM simulation 29

Fig.2.3 Velocity distribution along the micro-perforated plate 31

Fig.2.4 TL comparison between the theoretical prediction and FEM simulation, B=0.063 , m=1, τ =0.04, d=0.005, $\sigma = 0.5\%$ 33

Fig.3.1 Transmission loss of the plate silencer with different plates: plate (m=1, B=0.07) without perforations (dotted line), plate (m=1, B=0.057) without perforations (dashed line); plate (m=1, B=0.057) with micro-perforations(τ = 0.04, d = 0.007, $\sigma = 0.7\%$) (solid line).....37

Fig.3.2 Comparison between plate with and without perforations.(a)Transmission loss (TL) (b) reflection coefficient β and (c) absorption coefficient α 39

Fig.3.3 Variation in pressure difference Δp over the plate. (a) is the amplitude and (b) is the phase 42

Fig.3.4 Modal Analysis. The first column is the modal amplitude $|\overline{V}_j|$ and the second column is the modal reflection $|\overline{V}_j R_j|$, j=1,2,3.....43

Fig.3.5 Decomposition of the air velocity $\overline{v}_0$, plate velocity v_p and the overall velocity along the plate surface $\overline{v}$ .The first and second rows show the amplitude and phase respectively.....45

Fig.3.6 Total reactance of the first two modes. (a) Im(Z_{11}); (b)Im (Z_{22}) for which zero reactance is marked by an open circle……..46

Fig.3.7 Equivalent structural impedance $Z_{struc\_eq,j}$ for the first two modes, j=1,2. (1a) the resistant part of the 1st mode; (1b) reactant part of the 1st mode;(2a) resistant part of the 2nd mode; (2b) reactant part of the 2nd mode……48

Fig.3.8 Variation of TL with different bending stiffnesses 51

Fig.3.9 Variations of f_1 and f_2/f_1 with B 52

Fig.3.10 Variation in TL spectra with different mass ratios and different bending stiffnesses.....53

Fig.3.11 Parameters variation with mass ratio of the plate silencer with micro-perforation. (a) optimal bending stiffness B_{opt}; (b) the corresponding lower band limit f_1. (c) the corresponding working bandwidth f_2/f_1……...54

Fig.3.12 TL spectra with different diameters of hole.....56

Fig.3.13 TL spectra with different perforation ratios of the hole.....57

Fig.3.14 Variation of reflection coefficient and absorption coefficient with plate vibration excluded.....58

Fig.3.15 Variation in pressure differences at different perforation ratios 59

Fig.3.16 Optimization curve for different bending stiffnesses. The percentage on each point shows the perforation ratio to achieve the optimal f_2/f_1 with corresponding diameter.....60

Fig.4.1 Configuration of two-load method……66

Fig.4.2 Experimental set-up 68

Fig.4.3 Image of the plate silencer 69

Fig.4.4 Performance of the expansion chamber. 70

Fig.4.5 Composite plate: (a) method of adhering CF to PMI plate, (b) image of PMI plate reinforced by CFs.....72

Fig.4.6 (a) Configuration of the three-point bending test; (b) a result from the test.73

Fig.4.7 Mass ratio and bending stiffness of the composite plate.....74

Fig.4.8 Cross-section of the plate installation 75

Fig.4.9 Experimental results for validating the theoretical predictions 76

Fig.4.10 Experimental results from poor installation. (a) Transmission loss; (b) Reflection coefficient; (c) Absorption coefficient. 77

Fig.4.11 PMI plate and millimetre hole checked by microscope: (a) the surface of the PMI plate, (b) actual shape of the hole 78

Fig.5.1 Configuration of the hybrid noise control system……..83

Fig.5.2 Two-dimensional plate with general boundary conditions. 86

Fig.5.3 Configuration of a plate with two identical piezoelectric atuators attached symmetrically.....91

Fig.5.4 Displacement of a segment of the plate with piezoelectric actuators attached. 91

Fig.5.5 Comparison between the theoretical results and FEM simulation.....103

Fig.5.6 Comparison of TL spectra between the silencer with two plates ($B_{b1} = B_2^{'} =$ 0.129, $m_{b1} = m_2^{'} = 1$ and $L_{b1} = L_{b2} = 5$) and the silencer with only one plate ($B_{b1} = 0.129$, $m_{b1} = 1$ and $L_{b1} = 5$). 104

Fig.5.7 TL performance of the hybrid system in passive mode both without (dashed line) and with (solid line) micro-perforations in plate I.....105

Fig.5.8 TL performance of one-side-branch silencer and two-side-branch silencer with the plate of m=1, B=0.129 and L=5…….106

Fig.5.9 Variation of TL with the length of $L_{b2.}$ 108

Fig.5.10 Model amplitudes of plate I and plate II, with different $L_{b2.}$.....109

Fig.5.11 Variation of TL with $m_2^{'}$. 110

Fig.5.12 Variation of TL with different $B_2^{'}$. 111

Fig.5.13 TL performance under three configurations for the system with only plate I. Dashed linem_{b1}=1, B_{b1}=0.129 and L_{b1}=5, without perforations; Solid line: m_{b1}=1, B_{b1}=0.105 and L_{b1}=5, with perforations; Solid line with cross: m_{b1}=1, B_{b1}=0.105, L_{b1}=5,d_{b1}=0.005, σ_{b1}=0.5%,and $\tau_{b1}=0.04$ ……113

Fig.5.14 Variation of TL with different L_{b2} under two different sets of plate II. (a) $m_2^{'}$=1 and $B_2^{'}$=0.129; (b) $m_2^{'}$=20 and $B_2^{'}$=1. ……114

Fig.5.15 Solution of (x,y) and (x_w,y_w).....118

Fig.5.16 TL spectrum with different numbers of vibration modes involved. Dashed line: N=25; Solid line with cross: N=4; Solid line: N=2. 119

Fig.5.17 TL performance under three conditions. Dashed line: N=25 with all the modes coupled; Dotted line: N=2 with the two modes coupled; Solid line: N=2 with the two modes decoupled.....122

Fig.5.18 Amplitude and phase of $F_{piezo,1}$. Dashed line: results from the assumption. of the first two modes decoupled . Solid line: results from the accurate model. (1a)

amplitude of $F_{piezo,1}$, and (1b) phase of $F_{piezo,1}$ with $m_2^{'}=1$ and $B_2^{'}=0.129$;(2a) amplitude of $F_{piezo,1}$, and (2b) phase of $F_{piezo,1}$ with $m_2^{'}=100$ and $B_2^{'}=2$ ……...124

Fig.5.19 TL performance of the hybrid system driven by $F_{piezo,1}$. Dashed line: $F_{piezo,1}$ is calculated from the accurate model by involving 25 coupling modes; Solid line: $F_{piezo,1}$ is calculated from the model with first two decoupling modes…….124

Fig.5.20 Amplitude of term 1 and term 2 of Eq.(5.83), with (a) $m_2^{'}=1$ and $B_2^{'}=0.1$ (b) $m_2^{'}=90$ and $B_2^{'}=0.5$ 126

Fig.5.21 Resistant and reactant part of $Z_{dc2,1}$.....127

Fig.5.22 (a) $\mathrm{Im}(L_{2,1}^{'}+Z_{dc2,1})$ with $m_2^{'}=10$; (b) the corresponding $|F_{piezo,1}|$.....128

Fig.5.23 (a) $\mathrm{Im}(L_{2,1}^{'}+Z_{dc2,1})$ with $B_2^{'}=0.03$; (b) the corresponding $|F_{piezo,1}|$. 129

Fig.5.24 Imaginary part of the structure impedance of plate II $\mathrm{Im}(L_{2,1}^{'})$ and the duct and cavity impedance $-\mathrm{Im}(Z_{dc2,1})$, for the first mode with $m_2^{'}=90$ and $B_2^{'}=0.4$. 130

Fig.5.25 Amplitude and phase of $F_{piezo,1}$ with $m_2^{'}=90$ and $B_2^{'}=0.4$ 131

Fig.5.26 Amplitude and phase of the external voltage $\Delta\varphi$ 132

Fig.5.27 Performance of the hybrid passive and active noise control system.....133

NOMENCLATURE

B^*	Bending stiffness of the plate (kg·m^3/s^2)
B	Normalized bending stiffness of the plate
c_0^*	Speed of sound in free space (m/s)
c_0	Normalized speed of sound in free space
c_n	Phase speed of the nth duct mode, normalized
c_{rs}	Phase speed of the (r,s)th cavity mode, normalized
d^*	Diameter of the hole (m)
d	Normalized diameter of the hole
e_{31}	Stress/ charge coefficient of a piezoelectric element
ε_{33}	Permittivity coefficient of a piezoelectric element
E_F	Work done by external force on a vibration structure
E_k	Kinetic energy of a vibrating structure
E_p	Potential energy of a vibrating structure
f^*	Frequency (Hz)
f	Normalized frequency
f_1	Normalized lower band limit of the TL spectrum
f_2	Normalized higher band limit of the TL spectrum
H	Total enthalpy density of a piezoelectric patch
h^*	Duct height(m)
h	Normalized duct height

h_c^*	Cavity height(m)
h_c	Normalized cavity height
I	Normalized second moment of inertia
I_j	Modal coefficient of the incident wave
k_0^*	Total wavenumber, defined as $k_0^* = \omega^* / c_0^*$
k_0	Total wavenumber, defined as $k_0 = \omega / c_0$
k_n	Modal wavenumber, defined as $k_r = \omega / c_r$
k_{rs}	Modal wavenumber, defined as $k_{rs} = \omega / c_{rs}$
L^*	Cavity length(m)
L	Normalized cavity length
L_j	Modal structure impedance of the plate
m^*	Mass ratio of the plate (kg/ m^2)
m	Normalized mass ratio of the plate
p_i^*	Incident plane wave (Pa)
p_i	Normalized incident plane wave in the duct
p_r^*	Reflected sound wave in the duct (Pa)
p_r	Normalized reflected sound wave in the duct
p_t^*	Transmitted sound wave in the duct (Pa)
p_t	Normalized transmitted sound wave in the duct
p_{duct}^*	Radiation sound pressure in the duct (Pa)
p_{duct}	Normalized radiation sound pressure in the duct
$p_{duct,j}$	Normalized radiation pressure in the duct induced by the jth modal

	vibration of unit amplitude
p_{cav}^{*}	Radiation sound pressure in the cavity (Pa)
p_{cav}	Normalized radiation sound pressure in the cavity
$p_{cav,j}$	Normalized radiation pressure in the cavity induced by the jth modal vibration of unit amplitude
R_j	Complex amplitude of the reflected sound by the induced vibration of the *j*th vibration mode
t^{*}	Time (s)
t	Normalized time
T_j	Complex amplitude of transmitted sound by the induced vibration of the jth vibration mode
TL	Transmission loss
TL_{cr}	TL criterion
$\overline{v}$	Normalized total velocity of the micro-perforation plate
$\overline{v}_0^{*}$	Velocity of the air along the plate surface (m/s)
$\overline{v}_0$	Normalized velocity of the air along the plate surface
$\overline{V}_{0,j}$	Vibration amplitude of the air motion along the plate surface
v_p^{*}	Velocity of the plate vibration (m/s)
v_p	Normalized velocity of the plate vibration
$V_{p,j}$	Vibration amplitude of the jth in vacuo mode of plate
x^{*}, y^{*}, z^{*}	Dimensional Cartesian coordinate
x, y, z	Normalized Cartesian coordinate

Y^*	Young's modulus(Pa)
Y	Normalized Young's modulus
Z_0	Complex acoustic impedance of one hole normalized by $\rho_0^* c_0^*$
$Z_{resist,0}$	Resistant part of Z_0
$Z_{react,0}$	Reactant part of Z_0
$Z_{cav,jl}$	Modal radiation impedance to the cavity on the *j*th vibration induced by the *l*th vibration mode
$Z_{duct,jl}$	Modal radiation impedance to the duct on the *j*th vibration induced by the *l*th vibration mode
α	Absorption coefficient
β	Reflection coefficient
ρ_0^*	Air density (kg/m^3)
ρ_0	Normalized air density
η_p^*	Displacement of the plate vibration (m)
η_p	Normalized displacement of the plate vibration
ℓ	Lagrangian for the Lagrange equation
ω^*	Angular frequency(rad/s)
ω	Normalized angular frequency
μ^*	Coefficient of viscosity (m^2/s)
μ	Normalized coefficient of viscosity
τ^*	Thickness of the plate (m)
τ	Normalized thickness of the plate

σ	Perforation ratio
φ_j	jth vibration mode of the plate
ϕ_n	nth duct acoustic mode
ψ_{rs}	(r,s)th cavity acoustic mode
υ	Velocity potential
Δp	Sound pressure difference
$\Delta\varphi$	Driving voltage on the piezoelectric element (V)

CHAPTER 1 INTRODUCTION

1.1 Literature review

Acoustic noise problems become more evident and serious with increasing industrial equipment such as engines, fans and compressors. Meanwhile, the growth of high-density housing increases the exposure of the population to various noises. In addition, mechanical vibration is another related type of noise that commonly creates problems in areas of transportation, manufacturing and many household appliances.

For a long time, duct acoustics has attracted continuous interest due to its theoretical and practical importance. Nowadays, the noise from wind tunnels, ventilation systems and turbo-machinery becomes more and more serious. Therefore, there is a need for developing an effective technique to control the noise.

For noise control strategy, there are basically three key elements. The first is to control the sound or vibration source, while the second element is to control the sound in propagation and the third is to reduce the noise at the receiver. The present study mainly focuses on noise propagation reduction. Therefore, for this purpose, the control methods can be categorized into two types: passive and active noise control. Generally, high frequency noise can be easily reduced via the use of sound absorbing material. However, low frequency noise is difficult to control, especially through passive methods.

1.1.1 Passive noise control

Passive noise control is further classified into dissipative and reactive noise control, depending on whether the sound energy is dissipated or reflected.

A. Dissipative noise control

A dissipative noise control device usually involves the use of sound absorbing materials such as foam, mineral wool or fibreglass. Due to the friction between the porous material and the oscillating air, sound energy can be converted to heat, and thus be dissipated. Porous material has been the backbone of almost all dissipative noise abatement techniques. Lining ducts with porous sound absorbing materials is a very mature and reliable technique which can tackle medium to high frequency noise (Ingard, 1994). The propagation of sound in a porous material is governed by physical characteristics, such as porosity, tortuosity, flow resistivity, viscous characteristic length and thermal characteristic length (Johnson *et al.*, 1987; Delany and Bazley, 1970; Champoux and Allard, 1979). In order to predict the noise reduction, the propagation constant and characteristic impedance of the absorptive materials should be determined first. Empirical formulas based on experimental results have been studied (Mechel, 1988; Bies *et al.*, 1980; Attenborough, 1983). However, there are two major concerns regarding the application of porous materials: 1) the sound absorption techniques are not effective in the low frequency range. The convention of acoustic energy into heat is effective mainly for high frequencies with short wavelengths. If the thickness of a porous absorber is less than one quarter of the acoustic wavelength, the

absorber usually has little effect; 2) there has been increasing concerns about the deposition and accumulation of dust in the pores of the porous material, which may lead to bacterial breeding in ventilation systems. Hence, an alternative method, which is clean and effective at low frequencies, is desirable.

B. Reactive noise control

Reactive noise control relies on reflecting sound waves due to the impedance mismatches. Expansion chamber and Helmholtz resonator are typical examples. In an expansion chamber, waves are reflected due to the sudden change in cross-sectional area of a duct. Waves reflected from the first junction will be superimposed on those from the second junction. If the chamber has a length of a quarter wavelength or its odd multiples, maximum transmission loss will occur as the two reflected waves have the same phase, while no transmission loss occurs when the chamber length is half wavelength as the two reflected waves are out of phase. Expansion chamber has broadband frequency characteristics, though the attenuation is not high. Connecting multiple chambers of different length can eliminate the passband to broaden the working band of a single expansion chamber (Ingard and Pridmore, 1951).

Helmholtz resonator has a different noise reduction mechanism. It is widely used in ducts, pipes and many other applications (Munjal, 1987; Fry, 1988). In a Helmholtz resonator, the air in the cavity acts as a spring, while the air in the neck works as a mass. The resonance frequency is determined by the stiffness provided by the cavity and the

mass of the air in the neck. At the resonance frequency, the air in the neck oscillates fiercely upon the excitation by the incident wave because the cavity stiffness is balanced by the air inertia. Such balance eliminates the acoustic impedance to incident waves and zero pressure is maintained at the mouth of the resonator. As an effective noise control method, a lot of efforts have been made regarding how to predict and improve the performance of such device. Ingard (1953) discussed the scattering and absorption from resonators in the free field and in an infinite wall. Helmhotz resonators with different geometries, boundaries and complicated arrangements have also been investigated (Selamet *et al.*, 2003; Tang, 2005; Li and Cheng, 2007). However, when frequencies slightly shift from the resonance frequency, the impedance increases sharply and as a result the working band is very narrow, which limits its applications. Helmholtz resonators are still very attractive due to their obvious transmission loss at one particular frequency. Therefore, many efforts have been made to extend their applications. One application is the resonator array comprising multiple resonators (Seo and Kim, 2005). Through serial and parallel arrangement of the resonators, broadband characteristics at low frequency can be realized. Furthermore, the arrangement of the resonators has been optimized that various transmission loss shape can be obtained.

Plate silencer is another example for the reactive noise control method, which is aimed at a compact and broadband noise control device. The plate silencer is traced back to previous work done by Huang (1999). Flexible panels are flush-mounted in a

rigid duct. Fluid compressibility gives way to wall compliance (Lighthill, 1978) when waves travel in a passage with cross-sectional dispensability. A wave speed less than the isentropic speed of sound in air is rendered by the flexible wall compliance. Thus scattering and reflection occur at the upstream edge of the panel and the same phenomenon happens downstream. The combination of wave reflection and dissipation results in low-frequency noise reduction. However, the effect of the air outside the flexible panel was excluded. Therefore, in order to explore the potential application for a real silencer, a cavity is added to prevent noise leakage (Huang, 2002); hence, it is a drum-like silencer. A drum-like silencer consists of two identical membranes backed by a cavity correspondingly. Theoretical study shows that the drum-like silencer works effectively over a relatively broad stopband in the low to medium frequency range when the membranes are under a certain high tension applied in the axial direction of the duct. Modal analysis is carried out to evaluate the strong coupling between the membrane, the duct and the cavity. Practically, a tensile machine stretching the membrane is required to be installed to apply tension. Experimental validation is conducted without (Choy and Huang, 2002) and with flow (Choy and Huang, 2005). The performance of the drum-like silencer can be maintained when the flow speed is less than 20 m/s, which is the maximum flow speed in most ventilation systems. Besides validating the theoretical prediction, the dissipation mechanism is also modelled and compared with experimental results, which are mainly from the damping of the surface and edges of membrane and cavity. Moreover, parametric study is carried out to determine the optimal geometry of the configuration and the properties of the

membrane (Huang, 2005). The membrane tension plays a delicate role in adjusting the intervals of adjacent peaks of the stopband. The mass ratio and the tension determine the structure impedance and thus the stopband shift.

However, it is difficult to implement the drum-like silencer in reality on the site such as the fine tuning the tension and the membrane relaxation. Therefore, the membrane is replaced by a simply supported plate (Huang, 2006). Theoretical investigation has shown that the proposed plate silencer can achieve a wider stopband than a drum-like silencer with the same cavity geometry owing to the acoustic interference between the odd and even *in vacuo* vibration modes of the plate. The plate's natural bending moment is used as the sole structural restoring force to make the installation of the plate silencer easier. A plate silencer with clamped boundary condition is studied (Wang and Huang, 2007), and the boundary condition is easier to implement in practice than the simply supported one. The role of the plate is to purely reflect the sound to the upstream side. Desirable performance with a wide stopband can be achieved if the plate is very light with very high bending stiffness. Therefore, the requirements for the manufacture of composite plates are extremely high. By adhering two high-rigidity thin sheets with a relatively thick and light foam core, a sandwich plate is manufactured to supplement the requirement of plate mass and bending stiffness (Wang *et al.*, 2008). It has been shown that the mathematical homogeneous model can provide satisfactory prediction on the performance of an inhomogeneous sandwich plate silencer. A three-dimensional plate silencer is simulated to complete the study (Wang and Huang, 2008). Reinforced

composite plate by adhering carbon fibre tows to polymathacrylimide (PMI) has been constructed and experimental validation is conducted to determine the optimal bending stiffness and corresponding working band (Choy *et al.*, 2012).

Besides the wide stopband, the drum-like silencer and plate silencer have several merits such as 1) a fibre-free solution is provided for duct noise control, which avoids the breeding of bacteria caused by porous duct lining; 2) The membrane/plate is flush-mounted, with no variation of the cross-sectional area, and thus the flow can pass smoothly without any pressure loss.

Micro-perforated plate has been used as an alternative to traditional porous sound absorbing materials for decades. A micro-perforated plate (MPP) consists of a thin plate perforated with orifices of sub-millimetre distributed along its surface. MPP is usually backed by a cavity to form a set of Helmholtz resonators. It was developed in the late 1960s. The propagation of sound waves in a tube was investigated (Rayleigh, 1929), and simplified for short tubes (Crandall, 1926). Maa initially proposed micro-perforated panels (Maa, 1975; Maa, 1998). During the calculation, the impedance of one hole is converted into a simple averaged value corresponding to the fraction of the perforated open area. It is noted that the effect of vibration of a perforated plate has been excluded during the calculation. Since then the modelling of MPP has been studied theoretically and experimentally in various ways. One method for calculating the impedance of an MPP (Takahashi, 1997) involves the effect of the

diffraction phenomena caused by impedance discontinuities of the boundary surface. The result is more accurate compared with the previous method but also more complex. This is why the previous method is still adopted widely. The vibration effect of MPP was first studied experimentally (Lee, 1992). An additional sound absorption peak occurs at low frequencies due to the effect of panel vibration. To solve this problem, flow continuity at the plate surface in a spatially mean sense has been introduced (Takahashi and Tanaka, 2002), with an analytical model to study the flexural vibration of an MPP backed by an air gap developed. An equivalent circuit method has been used (Lee, 2007) to simplify the calculation of a flexible MPP by adding the mass reactance of the MPP panel in parallel to the MPP impedance. By experimental validations, by selecting the parameters such as panel thickness, perforation ration and curvature, the vibration of the panel can widen the working band.

MPP has been extensively used in different areas such as room acoustics (Fuchs and Zha, 1997; Kang and Fuchs, 1999; Droltleff and Zhou, 2001), barrier design (Asdrubali and Pispola, 2007) and ducts (Wu, 1997; Guo and Allam, 2008; Masson and Kogan, 2008; Chiu and Chang, 2008). And the use of micro-perforated tubes or plates in a single expansion chamber (Wu, 1997; Guo and Allam, 2008) or multiple chambers (Masson and Kogan, 2008) has also been investigated, entirely for sound absorption with an acoustically rigid micro-perforated structure. Up to now, most of such studies have focused on the function of the MPP device itself without considering the vibration of the plate and its vibro-acoustic coupling with the sound field in a duct.

1.1.2 Active noise control

By introducing a cancelling “anti-noise” wave through an appropriate array of secondary sources, active noise control (ANC) is achieved. The secondary sources are connected through an electronic system using a specific signal processing algorithm. ANC has been applied to a wide variety of problems in manufacturing, industries and consumer products. The design of acoustic ANC utilizes an electronically driven loudspeaker and a microphone to generate a cancelling sound wave (Lueg, 1936). An ANC system is designed to be adaptive in order to cope with variations such as the non-stationary amplitude and phase of the undesired noise. Loudspeakers are widely used as the secondary source (Nelson and Elliot, 1993; Hansen and Synder, 1997; Kim *et al.*, 1998). However, this control method is limited in its application because of site constraints, maintenance problems and performance instability. Hence, piezoelectric transducer, which is more stable and compact, has drawn increasing attention in vibration control applications. They can be used both as sensors and actuators.

The piezoelectric effect describes the relation between mechanical stress and electrical voltage in solids. The piezoelectric transducers are reversible: they strain when exposed to a voltage and conversely generate a voltage when they are strained. Man-made polycrystalline ceramic materials, such as lead zirconate titanate (PZT) exhibit strong coupling between the mechanical and electrical domains. This enables them to produce comparatively large forces or displacements for relatively small applied voltages, or vice versa; therefore, they are widely used as transducers.

Piezoelectric transducers are widely used in the form of thin sheets that can be bonded to or embedded in composite structures. As actuators they are mainly used to generate moment in flexible structures, while as sensors they are used to measure strain. Piezoelectric actuators are also available in the form of “stacks” (Lee and Moon, 1990; Lee, 1990) to generate large forces but small displacements in the direction normal to the top and bottom surfaces. Note, in this study, “piezo” is used as an abbreviation of “piezoelectric element”.

Since piezoelectric transducers are available in small dimensions to provide an easy way to induce or detect strain with no encumbrance, an increasing number of studies have focused on the actuation and sensing of structural vibrations by piezoelectric transducers. A beam response due to piezoelectric actuation was conducted as one of the first complete studies (Crawley and de Luis, 1987). Two actuators were bonded symmetrically on each side of a beam. The two piezos could be driven in phase to induce pure extensional deformation or 180° out of phase to induce pure flexural deformation. The axial force or moment applied by the piezos was determined through static analysis. A two-dimensional configuration of a thin plate was used as the extension of the previous work (Dimitriadis *et al.*, 1991). The variation of the piezo locations was studied. It was shown that the strain induced in the plate by the two piezos driven out of phase was equivalent to a line moment applied to the periphery of the piezos. The location of actuator and excitation of vibration modes was also studied (Clark and Fuller, 1991). The vibration modes are suppressed or

excited as determined by the phase difference of the driving voltage for each actuator pair. However, a considerable number of relevant papers neglect the dynamic effects of the piezoelectric elements (Lee and Chiang, 1991; Gibbs and Fuller, 1992; Koshigoe and Mudock, 1993). Actually, when mechanical coupling between the piezoelectric elements and host structure become strong, an especially large number of actuators and sensors are needed, and the effect on the mass and stiffness may not be ignored. So a dynamic model was reviewed (Brennan, 1997) and extension work was performed using Lagrange principles (Proulx and Cheng, 1990; St-Amant and Cheng, 2000). An asymmetric transducer was also investigated (Charette *et al.*, 1994), which induces extensional and flexural strain simultaneously. By taking the mass and bending stiffness of piezoelectric material into account, the model is more accurate when calculating the resonance frequencies or describing the dynamics.

1.1.3 Hybrid noise control

In recent years, there has been increasing interest in the reduction of sound and/or vibrations by the use of hybrid noise control techniques. One typical control method uses both active and passive elements in either series or parallel. The passive device usually undertakes the primary vibration attenuation, while the active part is used to enhance the performance of the passive system or to overcome the limitations of the passive system (Cobo and Cuesta, 2007).

Guiking and Lorentz (1984) adopted the hybrid noise control method to reduce low

frequency noise. By replacing the rigid termination by a loudspeaker, the pressure in a microphone behind the material is minimized (pressure-release condition). This active absorber provides an absorption coefficient of 0.6-0.7 in the medium frequency range. A low frequency absorber was proposed (Furtoss *et al.*, 1997) to actively control the impedance at the input of a liner. This method has been applied to flow duct applications (Sellen *et al*., 2006). Another strategy for designing active absorbers (Beyene and Burdisso, 1997), is called “impedance matching condition”. It is designed to cancel the reflected sound inside the air gap at the rear face of the material. It was demonstrated (Cobe *et al*., 2003) that the performance of both approaches (pressure-release and impedance matching) depended on the properties of the material. The pressure-release condition affords higher absorption when the flow resistance of the porous layer is matched to the acoustic impedance of air. The porous material can also be substituted by a micro-perforated panel (Cobe *et al*., 2004) for easier practical implementation due to its lightweight. A hybrid passive and active absorber with a micro-perforated plate and a 5-cm air gap covers a wide frequency range of 100 to 1600 Hz with a very high absorption coefficient. However, these two strategies have been proved to be effective for broadband noise control by involving loudspeakers for active control, which result in a weight and space penalty that may limit their applications.

Another example of impedance control is smart foam which has been extensively studied as it is easier to implement with much less weight compared with

loudspeakers (Guigou and Fuller, 1998; Guigou and Fuller, 1999; Leroy and Atalla, 2009). A smart foam usually consists of cylindrically curved sections of a vinylidene fluoride (PVDF) polymer film embedded in partially reticulated polyurethane acoustic foam thereby forming a very thin, compact arrangement (Gentry *et al*., 1996). It integrates a lightweight distributed piezoelectric actuator between individual layers of sound absorbing foam. The goal of implementing smart foam is to modify the acoustic impedance exposed to the incident waves.

However, the approach for the hybrid is not limited to the combination of active and passive control; the combination of different structures which have different noise control mechanisms has also been studied (Sakagami *et al.*, 2009; Lee *et al.*, 2009). Micro-perforated plate, membrane and cavity are combined (Kang and Fuchs, 1999). The basic idea is to regard a micro-perforated membrane as a parallel connection of the membrane and apertures. An equivalent circuit is used to verify this idea and it has been shown that it can work efficiently over 3~4 octaves. A Helmholtz resonator (HR) with a compliant back plate shunted with an analog circuit is studied (Liu and Horowitz, 2003; Liu and Horowitz, 2007). The compliant plate adds additional mass and stiffness to the system and the shunting circuit tunes the resonance frequency of the HR. In general, the hybrid control mechanism can enlarge the working band or tune the working band of a single factor.

1.2 Motivations and objectives

Effort has been made to develop silencers comprising an expansion chamber with two side-branch cavities covered by membranes or plates (Huang, 2002; Wang *et al.*, 2007). The aim is to achieve a compact, broadband and relatively low frequency noise control performance. While the promises of this technique have been demonstrated, there still are limitations hampering its application, which are mainly twofold: 1) the plate should have a very high bending stiffness and a very low mass ratio. For example, to ensure a reasonable level of structural response induced by acoustic incident waves, the mass ratio of plate to air should be about unity. Meanwhile the dimensionless bending stiffness should be about 0.07 which is equivalent to an aluminium plate of 1.4 mm thick with the same width. However, a 1.4 mm thick aluminium plate has a mass ratio to air of approximately 25.3, which far exceeds the desirable mass ratio range. Failure to do so results in a significant reduction in both the Transmission Loss (TL) level and the stopband. 2). The performance of the silencer is highly non-uniform across the frequency range, as demonstrated by the drastic fluctuation as well as the existence of troughs (passband) in the medium frequency range of the TL curve. This not only directly contributes to narrowing the stopband of the device, but also limits the use of the device for broadband noise control.

The objectives of this study are to develop a more broadband plate silencer that can reduce low frequency duct noise effectively. In doing so, hybrid noise control is

proposed in two steps.

Firstly, a plate silencer with micro-perforations is modelled. Micro-perforations are introduced into a very light and moderately stiff plate. The purpose of the micro-perforations is to add sound absorptions to compensate for the deficiency in the passband caused by the insufficient sound reflection due to the plate with weaker strength to mass ratio. For the first step, there are three specific objectives:

1) To establish a theoretical vibro-acoustic model, by taking the vibration of the plate as well as the plate-air interaction into consideration;

2) To understand the underlying physics related to the sound reflection and absorption due to the use of micro-perforations and their impact on the silencer performance;

3) To propose guidelines for the optimal design of an effective plate silencer with micro-perforations.

And secondly, a piezoelectric actuator attached to an extra plate is added into the configuration of the plate silencer with micro-perforations. The extra plate is driven by the actuator in a predetermined way. By coupling with the original micro-perforated plate, the aim is to enhance TL performance at low frequencies beyond the range of the passive system. The overall system is so-called hybrid passive

and active noise control system. Three objectives are listed as:

1) To establish a theoretical vibroacoustic model, which takes into account the full coupling between the two plates, the MPP, the piezoelectric actuators and the sound field in ducts and cavities;

2) To conduct a parametric study to gain a thorough understanding of the working mechanism of the hybrid system;

3) To propose guidance for the possibility of practical applications, including how to tune the external voltage based on the structure impedance of the extra plate by properly selecting the material parameters, e.g. geometry, density and Young's modulus of the extra plate and the piezoelectric actuators.

Therefore, with these two steps, a hybrid passive and active noise control system is established and studied parametrically. Dissipative and reactive mechanism as well as the active control algorithm is integrated to achieve broadband noise control with good performance at low frequencies.

1.3 Outline

The thesis is organized into six chapters. Chapter 1 introduces the background of the

present work. Related previous work is reviewed and the motivations as well as objectives of this study are presented.

In Chapter 2, a two-dimensional theoretical model of a plate silencer with micro-perforations is established. It consists of an expansion chamber with two side-branch cavities covered by light but relatively stiff micro-perforated plate. An analytical model of the sound-plate interaction is studied. With the finite element method (FEM) as a supplementary tool, the performance derived both from the theoretical prediction and FEM are compared for validation.

In Chapter 3, the numerical analysis and parametric study of the plate silencer with micro-perforations are carried out. Perforation effects will be explained in the aspect of transmission loss, absorption and reflection. Also the three typical influences on transmission loss brought about by micro-perforation are explained, i.e. the TL peaks reduced, the TL trough lifted up and the working bandwidth expanded to higher frequencies. Furthermore, the relationship between TL spectrum and the perforation parameters are studied, and optimization is conducted consequently based on two criteria of a broader working bandwidth as well as a releasing requirement for bending stiffness.

Experiment is set up for validation in Chapter 4. The spectral peaks and shapes of the measured transmission loss, reflection coefficient and absorption coefficient are

compared with those calculated theoretically. Attempts are also made to manufacture the composite plate. Carbon fibre is adhered to PMI as the reinforcement. The number of carbon fibres and the amount of glue should be delicately controlled to balance the mass and bending stiffness of the composite plate. The three influences of micro-perforation on the system are validated by experiments. Moreover, the deviation between the experimental results and the theoretical model is analyzed, which is mainly due to the dissipative mechanism in reality but excluded from the prediction.

In Chapter 5, a hybrid passive and active noise control system is modelled. It integrates the plate silencer, micro-perforations and piezoelectric actuators. Two plates are used to undertake different tasks. A longer micro-perforated plate, denoted as plate I, works in a similar way as that in Chapters 2 and 3, with the working range of low to medium frequency. Besides, a shorter plate, denoted as plate II, is attached with piezoelectric actuators, designed to work at low frequencies beyond the working range of plate I. A theoretical model is established by involving the coupling between the two plates as well as the mass and bending stiffness of piezoelectric actuators, and thus the passive performance of the system and the active excitation provided by actuators can be derived. Through parametric study, the coupling between the two plates can be tuned by properly selecting the parameters of the two plates. Also a guideline for material selection for practical application is given.

Chapter 6 summarizes the conclusion drawn from the present work and provides suggestions for further work.

CHAPTER 2 THEORETICAL STUDIES OF PLATE SILENCER WITH MICRO-PERFORATION

2.1 Introduction

Aimed at a compact, broadband and relatively low frequency noise control device, a plate silencer comprising an expansion chamber with two side-branch cavities covered with plates is developed (Huang, 2002; Huang, 2006; Wang *et al.*, 2007). Working in a purely reactive manner, the plate, which is flush-mounted with the inner duct wall, reflects the sound to the upstream side, creating favourable interference with the incoming sound by a proper tuning of the plate parameters. With the proper selection of the structural properties of the plate, the device can work effectively from low to medium frequencies. However, there are limitations hampering its application ,which are: 1) the severe requirement for a plate of very light weight but with a very high bending stiffness; such a harsh requirement can hardly be satisfied by conventional materials, but failure to do so will result in non-uniform transmission loss (TL) spectra with a narrowed stopband; and 2) the performance of the silencer is highly non-uniform across the frequency range, as demonstrated by the drastic fluctuations as well as the existence of troughs (passbands) in the medium frequency range of the TL curve. This not only directly contributes to narrowing the stopband of the device, but also limits the use of the device for broadband noise control. In order

to achieve a wider stopband, micro-perforation is introduced to a light plate with moderate stiffness. The purpose of the micro-perforations is to add sound absorption to compensate for the deficiency in the passband caused by insufficient sound reflection due to a plate with a weaker strength to mass ratio. Therefore, in this chapter a theoretical model is established to deal with the strong coupling between the vibrating micro-perforated plate and the sound field in the duct and cavity. Modal expansion is adopted to solve the coupling dynamic equations. The fluid loading on the micro-perforated plate in both the duct and the cavity is also provided. Furthermore, simulation based on the finite element method is carried out for the purpose of comparison with the theoretical predictions.

2.2 Theoretical modelling

The configuration of a two-dimensional model of the plate silencer with micro-perforation is shown in Fig. 2.1. The geometry resembles a standard expansion chamber with a main duct of height h^*, and two identical rectangular cavities of length L^* and depth h_c^*. The asterisks denote the dimensional variables, while the corresponding dimensionless ones are introduced shortly without asterisks. Two micro-perforated plates are used to cover the cavities, with the ends clamped. A plane incident sound wave is assumed to come from the left to right with unit amplitude

$$p_i^* = e^{i(\omega^* t^* - k_0^* x^*)} \tag{2.1}$$

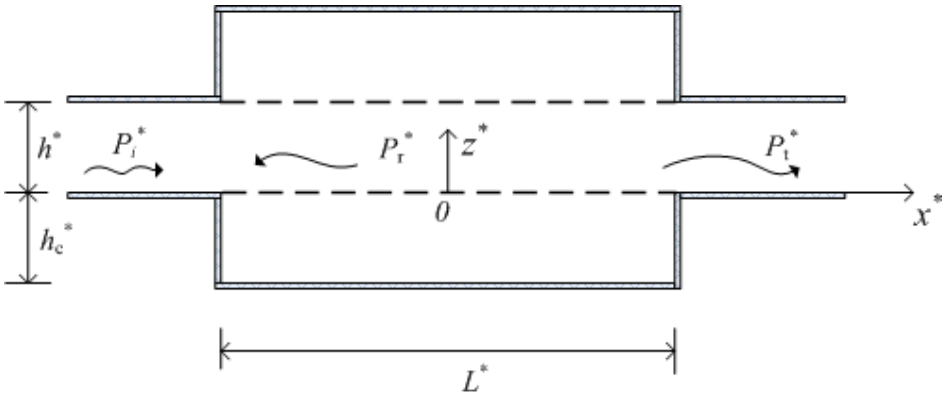

Fig.2.1 Theoretical model of the plate silencer with micro-perforation in a rectangular cavity.

and it excites the plate into vibration with a transverse displacement of complex amplitude η_p^* and velocity v_p^* with the same time dependence, $e^{i(\omega^* t^*)}$.

2.2.1 Air-plate interaction

The plate motion radiates sound in both directions of the duct, and also induces a fluid loading on itself from both the cavity and the duct side. The plate vibration is governed by the following equation

$$B^* \frac{\partial \eta_p^*}{\partial (x^*)^4} + m^* \frac{\partial^2 \eta_p^*}{\partial (t^*)^2} + (p_i^* + p_{duct}^* - p_{cav}^*) = 0 \qquad (2.2)$$

where B^* is the bending stiffness of the plate; m^* the plate mass per unit surface area, p_{duct}^* and p_{cav}^* the radiation pressures in the duct and cavity respectively.

Now considering the micro-perforations, which are a lattice of sub-millimetre holes uniformly distributed over the surface of the plate, the sound pressure difference applied between two sides of the plate generates air mass vibration in the holes. As the orifice diameter is much smaller than the acoustic wavelength of interest, the air particle velocity is assumed to be distributed uniformly within the area of each hole

and the air solid interaction is given by (Takahashi *et al*., 2002)

$$Z_{resist,0}(v_0^* - v_p^*) + Z_{react,0}v_0^* + \frac{1}{\rho_0^* c_0^*}(p_i^* + p_{duct}^* - p_{cav}^*) = 0 \tag{2.3}$$

where v_0^* is the particle velocity in a single hole; and v_p^* the vibration velocity of the plate. Z_0 denotes the complex acoustic impedance of the hole normalized by the characteristic impedance of the air $\rho_0^* c_0^*$. $Z_{resist,0}$ and $Z_{react,0}$ are the resistant part and reactant part of Z_0 respectively, which are proposed as (Maa, 1975)

$$\begin{aligned} Z_0 &= Z_{resist,0} + Z_{react,0} \\ &= \frac{32\mu^*\tau^*}{\rho_0^* c_0^* (d^*)^2}\left[(1+\frac{K^2}{32})^{0.5} + \frac{\sqrt{2}Kd^*}{32\tau^*}\right] + \frac{i\omega^*\tau^*}{c_0^*}\left[1+(1+\frac{K^2}{32})^{-0.5} + 0.85\frac{d^*}{\tau^*}\right] \end{aligned} \tag{2.4}$$

where τ^* is the thickness of the plate; d^* is the diameter of the hole; and μ^* is the coefficient of viscosity, $K = \frac{d^*}{2}\sqrt{\rho_0^*\omega^*/\mu^*}$. All the dimensional variables used are nondimensionalized by three quantities: air density ρ_0^*, speed of sound in free space c_0^*, and duct height h^* as

$$\begin{aligned} &x = \frac{x^*}{h^*},\ z = \frac{z^*}{h^*},\ h_c = \frac{h_c^*}{h^*},\ L = \frac{L^*}{h^*},\ \eta_p = \frac{\eta_p^*}{h^*},\ f = \frac{f^* h^*}{c_0^*}, \\ &m = \frac{m^*}{\rho_0^* h^*},\ B = \frac{B^*}{\rho_0^*(h^*)^3(c_0^*)^2},\ p = \frac{p^*}{\rho_0^*(c_0^*)^2} \\ &d = \frac{d^*}{h^*},\ \tau = \frac{\tau^*}{h^*},\ \mu = \frac{\mu^*}{\rho_0^* c_0^* h^*}. \end{aligned} \tag{2.5}$$

Assuming the plate is in a harmonic motion, $v_p = \frac{\partial \eta_p}{\partial t} = i\omega\eta_p$, Eq. (2.2) can be written as

$$\frac{B}{i\omega}\frac{\partial^4 v_p}{\partial x^4} + mi\omega v_p + (p_i + p_{duct} - p_{cav}) = 0 \tag{2.6}$$

Eq. (2.3) turns into

$$Z_{resist,0}(v_0 - v_p) + Z_{react,0}v_0 + p_i + p_{duct} - p_{cav} = 0 \tag{2.7}$$

An average air velocity $\overline{v}_0$ is obtained by averaging the discrete air particle velocity over each orifice across the adjacent imperforated region of the plate as

$$\overline{v}_0 = v_0\sigma \tag{2.8}$$

Where σ is the perforation ratio of the plate.

The dynamics of the plate described in Eq. (2.6) and Eq. (2.7) can be solved by the standard Galerkin procedure, in which $v_p(x)$ is expanded as a series of *in-vacuo* modes $\varphi_j(\xi)$ of the clamped-clamped plates with modal amplitude $V_{p,j}$

$$v_p(x) = \sum_{j=1}^{\infty} V_{p,j}\varphi_j(\xi), \qquad \xi = x/L + 1/2 \tag{2.9}$$

Where

$$\varphi_j(\xi) = A_{1,j}e^{\lambda_j\xi} + A_{2,j}e^{-\lambda_j\xi} + A_{3,j}\sin(\lambda_j\xi) + A_{4,j}\cos(\lambda_j\xi) \tag{2.10}$$

With

$$A_{1,j} = \frac{1}{2}(1-\varepsilon_j),\ A_{2,j} = \frac{1}{2}(1+\varepsilon_j),\ A_{3,j} = \varepsilon_j,\ A_{4,j} = -1 \tag{2.11}$$

$$\varepsilon_j = \frac{\cosh(\lambda_j) - \cos(\lambda_j)}{\sinh(\lambda_j) - \sin(\lambda_j)}, \cos(\lambda_j)\cdot\cosh(\lambda_j) = 1 \tag{2.12}$$

So $\overline{v}_0$ is also expanded over the same series $\varphi_j(\xi)$ as

$$\overline{v}_0(x) = \sum_{j=1}^{\infty} \overline{V}_{0,j}\varphi_j(\xi) \tag{2.13}$$

So $v_0(x) = \sum_{j=1}^{\infty} V_{0,j}\varphi_j(\xi)$ with $V_{0,j} = \frac{\overline{V}_{0,j}}{\sigma}$.

Therefore, Eq. (2.6) and Eq. (2.7) become

$$\{\frac{B}{i\omega}(\frac{\beta_j}{L})^4 + mi\omega\}V_{p,j} + \int_0^1 (p_i + p_{duct} - p_{cav})\varphi_j(\xi)d\xi = 0 \tag{2.14}$$

$$Z_{resist,0}(V_{0,j}-V_{p,j})+Z_{react,0}V_{0,j}+\int_0^1(p_i+p_{duct}-p_{cav})\varphi_j(\xi)d\xi=0 \qquad (2.15)$$

respectively.

2.2.2 Fluid loading on MPP in the duct

Given the average velocity distribution for the whole plate with micro-perforations $\overline{v}(x)$, which is defined as $\overline{v}(x)=(1-\sigma)v_p(x)+\overline{v}_0(x)$, the radiated pressure p_{duct} can be calculated as (Doak,1973)

$$p_{duct}(x,z)=\frac{L}{2}\sum_{n=0}^{\infty}c_n\phi_n(z)\times\int_0^1\overline{v}(x')\phi_n(z')[H(x-x')e^{-ik_n(x-x')}+H(x'-x)e^{+ik_n(x-x')}]d\xi' \quad (2.16)$$

with

$$c_n=\frac{i}{\sqrt{(n\pi/\omega)^2-1}},\ k_n=\frac{\omega}{c_n},\ \phi_n(z)=\sqrt{2-\delta_{0n}}\cos(n\pi z) \qquad (2.17)$$

where $H(x)$ is the Heaviside function, δ_{0n} is the Kronecker delta, and c_n, k_n, ϕ_n are respectively the modal phase speed, modal wave number and the modal velocity potential. The source is specified as a plate vibration at $z'=0$, $x'\in[-L/2, L/2]$.

Assuming that the radiation pressure caused by the jth modal vibration of unit amplitude φ_j is $p_{duct,j}$ which is denoted as

$$p_{duct,j}(x,z)=\frac{L}{2}\sum_{n=0}^{\infty}c_n\phi_n(z)\times\int_0^1\varphi_j(x)\phi_n(z')[H(x-x')e^{-ik_n(x-x')}+H(x'-x)e^{+ik_n(x-x')}]d\xi' \quad (2.18)$$

and at $z=0$

$$p_{duct,j}(x,0)=\frac{L}{2}\sum_{n=0}^{\infty}c_n\times\int_0^1\varphi_j(x)[H(x-x')e^{-ik_n(x-x')}+H(x'-x)e^{+ik_n(x-x')}]d\xi' \quad (2.19)$$

The total fluid loading in the duct will be expressed as

$$p_{duct} = \sum_{j=1}^{\infty} \bar{V}_j \, p_{duct,j} \tag{2.20}$$

The duct modal impedance is then defined as

$$Z_{duct,jl} = \int_0^1 p_{duct,j}(x,0)\varphi_l(\xi)d\xi \tag{2.21}$$

Substituting Eq. (2.19) into Eq. (2.21) gives

$$\begin{aligned} Z_{duct,jl} &= \frac{L}{2}\sum_{n=0}^{\infty} c_n \times \int_0^1\int_0^1 \varphi_j(x)[H(x-x')e^{-ik_n(x-x')} + H(x'-x)e^{+ik_n(x-x')}]d\xi'\varphi_l(\xi)d\xi \\ &= i\frac{L}{2}\sum_{n=0}^{\infty}\frac{(2-\delta_{0r})}{\sqrt{(r\pi)^2-k_0^2}}\sum_{p=1}^{4}\sum_{q=1}^{4} A_{p,l}\cdot A_{q,j}\cdot \Pi_{p,q} \end{aligned} \tag{2.22}$$

where $A_{p,l}$ and $A_{q,j}$ are coefficients defined in Eq. (2.11). And the coefficients $\Pi_{p,q}$ are given in the Appendix.

2.2.3 Fluid loading on MPP in the cavity

The sound pressure inside the cavity p_{cav} can be expressed in terms of the acoustic modes of a rigid-walled cavity with a light damping (Cheng, 2005)

$$p_{cav}(x,z) = \sum_{r,s}\frac{-i\omega\psi_{rs}(x,z)}{Lh_c(\kappa_{rs}^2 - k_0^2 + 2i\zeta_{rs}\kappa_{rs}k_0)}\int_0^1 \bar{v}(x',0)\psi_{rs}(x',0)d\xi' \tag{2.23}$$

where ζ_{rs} is the damping ratio of the (*r*,*s*)th acoustic mode $\psi_{rs}(x,z)$, and κ_{rs} the corresponding acoustic wave number of the acoustic mode $\psi_{rs}(x,z)$, with $\psi_{rs}(x,z)$ and κ_{rs} given as

$$\psi_{rs}(x,z) = \sqrt{(2-\delta_{0r})(2-\delta_{0s})}\cos\left(\frac{r\pi x}{L}\right)\cos\left(\frac{s\pi z}{h_c}\right) \tag{2.24}$$

$$\kappa_{rs}^2 = \left(\frac{r\pi}{L}\right)^2 + \left(\frac{s\pi}{h_c}\right)^2 \tag{2.25}$$

The total fluid loading inside the cavity will be expressed as

$$p_{cav} = \sum_{j=1}^{\infty} \bar{V}_j p_{cav,j} \tag{2.26}$$

where

$$p_{cav,j}(x,z) = \sum_{r,s} \frac{-i\omega\psi_{rs}(x,z)}{Lh_c(\kappa_{rs}^2 - k_0^2 + 2i\zeta_{rs}\kappa_{rs}k_0)} \int_0^1 \varphi(x')\psi_{rs}(x',0)d\xi' \tag{2.27}$$

At the plate surface z=0

$$p_{cav,j}(x,0) = \sum_{r,s} \frac{-i\omega\psi_{rs}(x,0)}{Lh_c(\kappa_{rs}^2 - k_0^2 + 2i\zeta_{rs}\kappa_{rs}k_0)} \int_0^1 \varphi(x')\psi_{rs}(x',0)d\xi' \tag{2.28}$$

The corresponding cavity modal impedance is given as

$$Z_{cav,jl} = -\int_0^1 p_{cav,j}(x,0)\varphi_l(\xi)d\xi \tag{2.29}$$

Substituting Eq. (2.28) into Eq. (2.29)

$$Z_{cav,jl} = -\sum_{r,s} \frac{-i\omega}{Lh_c(\kappa_{rs}^2 - k_0^2 + 2i\zeta_{rs}\kappa_{rs}k_0)} \int_0^1 \psi_{rs}(x,0) \int_0^1 \varphi(x')\psi_{rs}(x',0)\varphi_l(\xi)d\xi' d\xi \tag{2.30}$$

Re-arranging the double integration

$$\begin{aligned} Z_{cav,jl} &= \sum_{r=0}^{\infty}\sum_{s=0}^{\infty} \frac{ik_0(2-\delta_{0r})(2-\delta_{0s})}{h_c(\kappa_{rs}^2 - k_0^2 + 2i\zeta_{rs}\kappa_{rs}k_0)} \int_0^1 [\int_0^1 \varphi_j(\xi')\cos(r\pi\xi')d\xi']\cos(r\pi\xi)\varphi_l(\xi)d\xi \\ &= \sum_{r,s} \frac{ik_0(2-\delta_{0r})(2-\delta_{0s})}{h_c(\kappa_{rs}^2 - k_0^2 + 2i\zeta_{rs}\kappa_{rs}k_0)} I_{c,jl} \end{aligned} \tag{2.31}$$

where $I_{c,jl}$ is defined as

$$\begin{aligned} I_{c,jl} = &\int_0^1 [A_{1,j}e^{\beta_j\xi'} + A_{2,j}e^{-\beta_j\xi'} + A_{3,j}\sin(\beta_j\xi') + A_{4,j}\cos(\beta_j\xi')]\cos(r\pi\xi')d\xi' \\ &\cdot \int_0^1 [A_{1,l}e^{\beta_l\xi} + A_{2,l}e^{\beta_l\xi} + A_{3,l}\sin(\beta_l\xi) + A_{4,l}\cos(\beta_l\xi)]\cos(r\pi\xi)d\xi \end{aligned} \tag{2.32}$$

2.2.4 Vibration matrix and transmission loss

Eq. (2.14) and Eq. (2.15) can be cast into a set of linear equations in terms of modal vibration in j mode as

$$L_j V_{p,j} + (Z_{duct,jl} - Z_{cav,jl})[(1-\sigma)V_{p,j} + \sigma V_{0,j}] = -I_j \tag{2.33}$$

$$Z_{resist,0}(V_{0,j}-V_{p,j})+Z_{react,0}V_{0,j}+(Z_{duct,jl}-Z_{cav,jl})[(1-\sigma)V_{p,j}+\sigma V_{0,j}]=-I_j \quad (2.34)$$

where $L_j=\{\frac{B}{i\omega}(\frac{\beta_j}{L})^4+mi\omega\}$, and I_j is the modal coefficient of incident waves which is defined as

$$I_j=\int_0^1 p_i\varphi_j(\xi)d\xi \quad (2.35)$$

As a result, $V_{0,j}$ and $V_{p,j}$ can be solved through matrix inversion, given as

$$\begin{bmatrix} L_j+(Z_{duct,jl}-Z_{cav,jl})(1-\sigma) & (Z_{duct,jl}-Z_{cav,jl})\sigma \\ (Z_{duct,jl}-Z_{cav,jl})(1-\sigma) & (Z_{resist,0}+Z_{react,0})+(Z_{duct,jl}-Z_{cav,jl})\sigma \end{bmatrix}\begin{bmatrix} V_{p,j} \\ V_{0,j} \end{bmatrix}=-\begin{bmatrix} I_j \\ I_j \end{bmatrix} \quad (2.36)$$

The total sound pressure transmitted downstream is determined by adding the incident wave p_i to the far-field radiation wave p_{duct}, which can be found with the help of Eq. (2.16) by taking only the plane wave mode with $n=0$ for $x>L/2$

$$p_t=p_{duct}\big|_{n=0,x\to+\infty}+p_i \quad (2.37)$$

Similarly

$$p_r=p_{duct}\big|_{n=0,x\to-\infty} \quad (2.38)$$

Hence, for an incident wave of unit amplitude, the transmission loss of the silencer can be calculated as

$$\mathrm{TL}=-20\log_{10}\frac{|p_t|}{|p_i|} \quad (2.39)$$

The coefficients of sound power reflected and absorbed are calculated respectively by

$$\beta=\left|\frac{p_r}{p_i}\right|^2,\ \alpha=1-\beta-\left|\frac{p_t}{p_i}\right|^2 \quad (2.40)$$

where p_r is given by

$$p_r=\frac{1}{2}\int_{-L/2}^{L/2}\bar{v}(x')e^{-ik_0x'}dx'=\sum_{j=1}^{\infty}\bar{V}_jR_j \quad (2.41)$$

with

$$R_j = \int_{-L/2}^{L/2} \varphi_j(\xi') e^{-ik_0 x'} dx' \tag{2.42}$$

R_j is the complex amplitude of the reflected sound by the induced vibration of the *j*th mode with unit amplitude, and $\bar{V}_j R_j$ is defined as the modal reflection which evaluates the reflection capability of each mode.

2.3 Simulation with finite element method

In order to validate the theoretical results, the finite element method (FEM) is adopted to simulate the plate silencer with micro-perforations. For symmetry and simplicity, only half of the device is simulated, as shown in Fig. 2.2. A plane sound wave is assumed to come from the left to the right with unit amplitude $p_i = e^{i(\omega t - k_0 x)}$

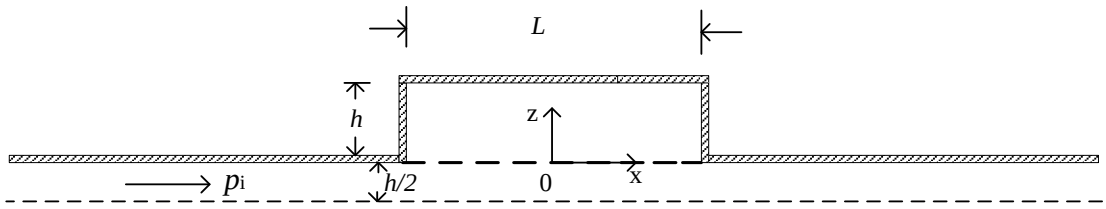

Fig.2.2 Configuration of plate silencer for FEM simulation

It induces the plate to vibrate with a normal displacement of complex amplitude η_p with the same time dependence. The plate motion radiates sound into both duct directions $\pm x$, and imposes a radiation pressure on the plate.

2.3.1 Setup of the model

The finite element method is conducted with the use of Femlab®. Femlab® is a software package for solving partial differential equations based on the finite element

method. It is chosen to solve the current vibroacoustic coupling problem due to its strong multi-physics capability. In the current simulation there are two types of physical domain. One is the two-dimensional acoustic domain for the air in the duct and cavity, the other is the one-dimensional domain for the plate (beam), which is modelled based on an In-plane Euler beam.

The velocity potential υ in the duct and cavity are modelled by the Helmholtz equation

$$\left(\nabla^2 - \frac{1}{c_0^{\,2}}\frac{\partial^2}{\partial t^2}\right)\upsilon = 0 \tag{2.43}$$

The relationship between sound pressure p, acoustical particle velocity v and the velocity potential υ are shown as

$$p = -\rho_0 \frac{\partial \upsilon}{\partial t}, \quad v = \nabla \upsilon \tag{2.44}$$

In which, c_0 is the speed of sound in air, and ρ_0 the density of air. The vibration of the plate is governed by the following dynamic equation

$$m\frac{\partial^2 \eta_p}{\partial t^2} + B\nabla^4 \eta_p + \Delta p = 0 \tag{2.45}$$

Where m and B are the mass ratio and bending stiffness of the plate respectively, and Δp is the sound pressure difference across the interface at z=0

$$\Delta p = p\big|_{z=0^+} - p\big|_{z=0^-} \tag{2.46}$$

Furthermore, according to velocity continuity

$$\frac{\partial \upsilon}{\partial z}\Big|_{z=0^+} = \frac{\partial \upsilon}{\partial z}\Big|_{z=0^-} = \overline{v} \tag{2.47}$$

where $\overline{v}$ is the total velocity along the plate surface. When there are no perforations,

$\overline{v} = \dfrac{\partial \eta_p}{\partial t}$. If micro-perforations are involved, the velocities are shown in Fig. 2.3.

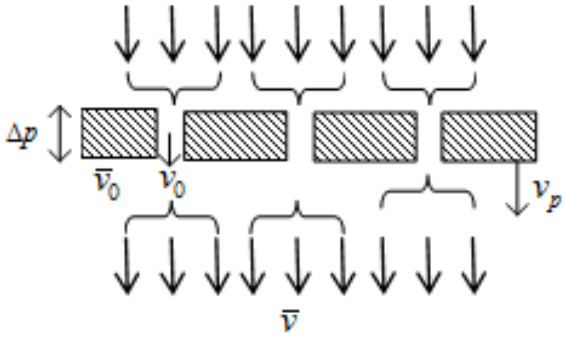

Fig.2.3 Velocity distribution along the micro-perforated plate

The plate has its own vibration velocity, denoted as v_p. Assuming the air passes through a single hole with a velocity of v_0, by multiplication with the perforation ratio σ, it represents the total velocity contributed by the holes, denoted as $\overline{v}_0$. So the total velocity along the surface of the plate can be defined as

$$\overline{v} = v_p + (v_0 - v_p)\sigma \tag{2.48}$$

Combining with Eq. (2.7), results in

$$\overline{v} = v_p(1 - \frac{Z_{react,0}}{Z_0} \cdot \sigma) + \frac{\Delta p}{Z_0} \cdot \sigma, \quad Z_0 = Z_{resist,0} + Z_{react,0} \tag{2.49}$$

Also the boundary conditions for the inlet and outlet of the duct need to be specified. For frequencies below the first cut-on frequency of the duct, the simple travelling wave governs

$$\upsilon_{\pm} = A_{\pm} \exp(i\omega t \mp ik_0 x), \qquad p_{\pm} = \pm \rho_0 c_0 v \tag{2.50}$$

where the signs $\pm$ apply to the down-going and up-going waves respectively. At the exit an anechoic boundary condition is assumed, so that $p = \rho_0 c_0 v$, which is

$$\frac{\partial \upsilon}{\partial x} + ik_0 \upsilon = 0 \tag{2.51}$$

At the inlet, the incident wave p_i and reflected wave are combined together. Assuming a total sound wave p, total acoustic particle velocity v, incident particle velocity v_+, reflected wave p_r and particle velocity v_-, they satisfy the following relationship, as

$$p_r = p - p_i, \quad v_- = v - v_+, \quad p_r = -\rho_0 c_0 v_- \tag{2.52}$$

Thus

$$p - p_i = -\rho_0 c_0 (v - v_+) \tag{2.53}$$

$$p + \rho_0 c_0 v = 2 p_i \tag{2.54}$$

By assuming p_i=1

$$\frac{\partial \upsilon}{\partial x} - ik_0 \upsilon = \frac{2}{\rho_0 c_0} \tag{2.55}$$

The wall of the duct and cavities are assumed to be acoustically rigid, so the boundary condition along the wall is

$$\frac{\partial \upsilon}{\partial \vec{n}} = 0 \tag{2.56}$$

where $\vec{n}$ is the outward normal direction. Eqs. (2.43) to (2.56) are solved in Femlab®, and the transmission loss of the plate silencer is determined as

$$TL = 10 \log_{10} \left(\frac{\int_{exit} |\upsilon|^2 \, ds}{\int_{inlet} |\upsilon_i|^2 \, ds} \right) \tag{2.57}$$

The absorption coefficient α and the reflection coefficient β are evaluated as

$$\alpha = 1 - \frac{\int_{inlet} |\upsilon - \upsilon_i|^2 \, ds + \int_{exit} |\upsilon|^2 \, ds}{\int_{inlet} |\upsilon_i|^2 \, ds} \tag{2.58}$$

$$\beta = \frac{\int_{inlet} |\upsilon - \upsilon_i|^2 \, ds}{\int_{inlet} |\upsilon_i|^2 \, ds} \tag{2.59}$$

2.3.2 Comparison between the analytical and FEM results

Fig. 2.4 shows the comparison between the theoretical prediction (solid line) and FEM simulation (dashed line) of TL. A set of parameters are chosen: B=0.063, m=1, τ =0.04, d=0.005, and $\sigma = 0.5\%$. Although there is little deviation in the range of f=0.05 to 0.1, the curves generally match each other.

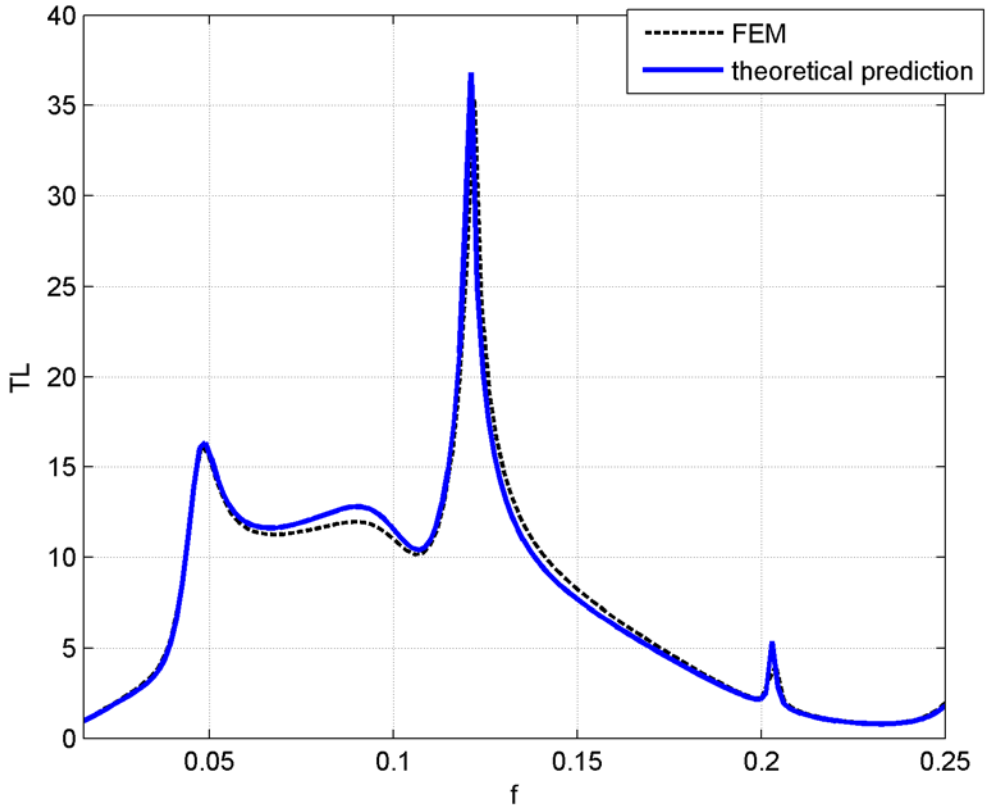

Fig.2.4 TL comparison between the theoretical prediction and FEM simulation, B=0.063, m=1, τ =0.04, d=0.005, $\sigma = 0.5\%$.

2.4 Summary

A two-dimensional theoretical model of a plate silencer with micro-perforations has been established in this chapter. Some summarized points are given as follows:

1). Dynamic equations have been developed for describing the vibration of the micro-perforated plate with clamped ends and the plate-air interaction. Friction occurs due to relative velocity between the plate and oscillating air through the sub-millimetre holes.

2). Modal expansion has been carried out to solve the equations. The fluid loading acting on the plate can be expanded as the summation of vibration modal amplitude and modal impedance. Finally the equations can be solved through matrix inversion.

3). Finite element method has also been used for the validation of the theoretical results. The domains and boundaries of the configuration are well defined in order to describe the interaction between the vibrating micro-perforated plate and the sound field inside the duct and cavity. The results of the finite element method and analytical calculations generally agree with each other within the frequency range of the interest.

CHAPTER 3

NUMERICAL RESULTS AND ANALYSES

3.1 Introduction

A theoretical model of the plate silencer with micro-perforations has been established in Chapter 2. The plate, drilled with sub-millimetre holes, vibrates when incident sound waves arrive, and thus air flow is driven through the holes. Friction occurs when the relative velocity between the vibration of the plate and air flow exists, and therefore part of the sound energy is dissipated. The absorption mechanism is intended to compensate for the deficiency in plate reflection. In Chapter 2, modal expansion is used to solve the dynamic equations. Fluid loading is expanded based on the plate vibration modes as well as the duct and cavity modes. The reflected sound pressure can be expressed as the summation of the plate vibration modal amplitude and a reflecting complex which describes the ability of reflecting sound for each vibration mode, and TL can be obtained correspondingly.

In this chapter, the detailed working principles of the plate silencer with micro-perforations are studied. The improvement in the working bandwidth of the TL spectrum together with the reduction in the TL peak and the lift of the TL trough when the perforation is added on the plate is to be discussed. A parametric study is carried out to study the relationship between the different variables and their effect on the TL

performance. In order to achieve optimal results, optimization is conducted. It will show that the micro-perforation plays an important role in reducing the severe structural property requirements of a plate with a very high bending stiffness.

3.2 Performance analyses

There are many variables to be considered for achieving the good performance of a plate silencer with micro-perforations. The performance study is first carried out with most variables fixed, such that the length of the plate $L = 5$, the cavity depth $h_c = 1$, the height of the duct h = 1, and the mass ratio of the plate $m = 1$. The bending stiffness of the plate is a very influential parameter, which is varied while studying the effect of the properties of micro-perforation, such as the diameter of the holes, perforation ratio and the thickness of the plate. The performance of the plate-silencer is evaluated by the logarithmic width of its stopband, defined as the frequency range in which TL is everywhere equal to or greater than a suitable criterion level (TL_{cr}). Expressed symbolically, $f \in [f_1, f_2]$ in which $TL \geq TL_{cr}$ and TL_{cr} =10 dB in the present study. A cost function is set as the ratio of the band limits f_2 / f_1 in the optimization of the design.

In order to ensure the accuracy of calculations, the duct, cavity and plate modes are truncated to 50, 50 and 25 respectively. A further increase in the number of modes does not make a noticeable improvement in the calculation results within the frequency range of interest of the present work.

3.2.1 Results of default configurations

The effect of micro-perforation on the TL is first presented before detailed analyses are provided in later sections. Fig. 3.1 compares the TL of the plate silencer with and without micro-perforations for three configurations.

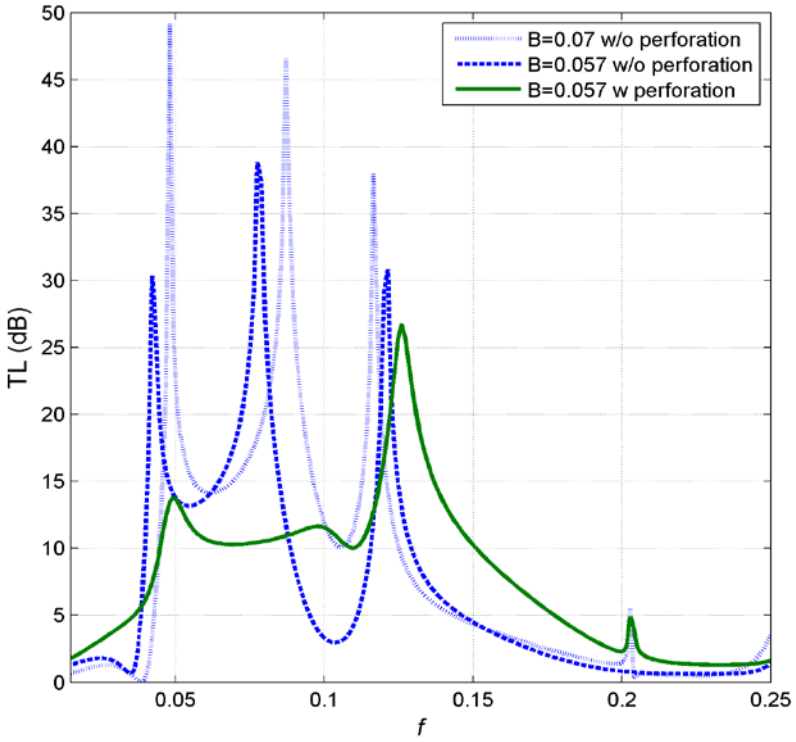

Fig.3.1 Transmission loss of the plate silencer with different plates: plate (m=1, B=0.07) without perforations (dotted line), plate (m=1, B=0.057) without perforations (dashed line); plate (m=1, B=0.057) with micro-perforations (τ=0.04, d=0.007, $\sigma = 0.7\%$) (solid line).

The TL curve, shown as the dotted line, with B=0.07, was previously determined as the optimal bending stiffness for a plate silencer without any perforations. Three peaks are observed which are shown to be caused by the strong sound reflection from the plate due to the dominance of the first two modes of the plate. The stopband

begins at $f_1 = 0.044$ and ends at $f_2 = 0.124$, corresponding to $f_2 / f_1 = 2.81$. Note that the bending stiffness required is very high. Reducing *B* by about 20% down to 0.057, the trough between the second and third peaks in the TL curve drastically drops resulting in a TL of less than 10 dB, so that the overall stopband is significantly decreased to $f_2 / f_1 = 2.21$ (dashed line). Keeping the same bending stiffness at $B = 0.057$, perforations with $\sigma = 0.7\%$ and a nondimensional diameter *d* = 0.007 (dimensional diameter d^*= 0.7 mm) are then added to the plate. It can be seen that micro-perforations can lift up the trough between the second and third peaks so that a more flattened TL curve is obtained. Meanwhile, compared with the TL of *B*=0.07, while basically keeping the same f_1, the third peak on the TL curve is moved to a higher frequency so that the stopband ends at a much higher frequency at $f_2 = 0.15$. This corresponds to $f_2 / f_1 = 3.45$, a significant broadening of the stopband of about 23% compared to the optimally designed stiff plate silencer, or 56% compared to that with the same bending stiffness but without perforations. Therefore, the use of micro-perforations in the plate seems to result in a more uniform TL with a broader stopband with the use of a less stiff plate. This is beneficial for coping with broadband noise control. By the same token, the harsh requirement of the high bending stiffness of the plate imposed by the original silencer design is also relaxed. The underlying physics explaining these effects are provided in the following sections.

3.2.2 Noise reduction mechanism

Analyses are performed to explore the underlying physics and to explain such an

improvement on the stopband due to the addition of micro-perforations. In particular, the effectiveness of sound reflection and sound absorption enhancement by the micro-perforated plate (MPP) as well as the plate's response are to be discussed. Using B=0.057, the reflection coefficient (β) and absorption coefficient (α) are shown in Fig. 3.2, together with the corresponding TL curve, to facilitate the analysis of the peak and trough frequency variation.

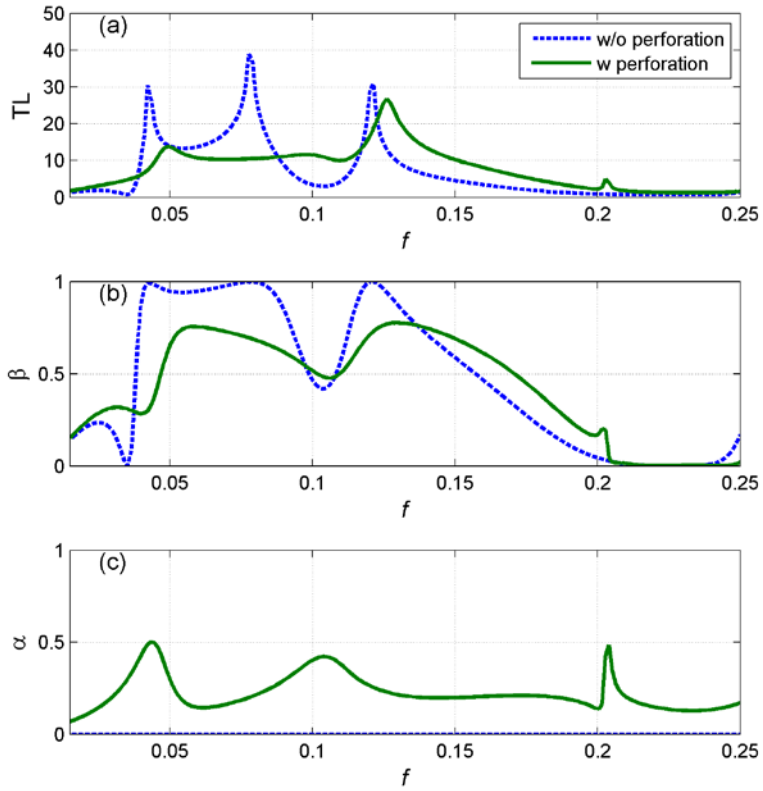

Fig.3.2 Comparison between the plate with and without perforations. (a) Transmission loss (TL) (b) reflection coefficient β and (c) absorption coefficient α.

It can be observed from Fig. 3.2(a) and Fig. 3.2(b) that without perforations the plate silencer purely relies on strong sound reflection, as evidenced by the high β regions to create high TL peaks. The addition of the micro-perforations generally reduces the

sound reflection from the plate. Roughly speaking, upon deployment of the micro-perforations the whole reflection coefficient spectrum seems to be slightly shifted towards higher frequencies, and hence an enhancement in the reflection coefficient for $f > 0.13$ is observed. Fig. 3.2(c) shows the corresponding absorption coefficient spectrum. Without perforations there is practically no absorption, so the dashed line is maintained at zero at all frequencies. With micro-perforations the absorption coefficient is about 0.3 on average, with two peaks at f =0.043 and f=0.104, respectively, which do not exactly coincide with the peaks in the TL spectra. The nature of these absorption peaks will be examined later. It is however pertinent to note that the second peak at f = 0.104, with α of about 0.42, directly contributes to the increase in TL, where the original trough region without micro-perforations is elevated.

3.3 Analysis of the TL spectrum

From the previous Sec. 3.2, with the addition of micro-perforations three main observations can be made: (1) all TL peaks are smoothed out while slightly shifting towards higher frequencies; (2) the original trough of TL for a plate without micro-perforations is raised, mainly because of the increase in sound absorption; and (3) the stopband is widened due to the shift of the third dominant peak to a higher frequency. These phenomena are explained in this section.

3.3.1 TL peaks

In this section three aspects are considered for studying the mechanism of sound and plate interaction for explaining the reason for the smoothing of the TL peaks. These are 1) the variation in the sound pressure acting upon the plate which is the driving force for plate vibration and air flow through the holes; 2) the dominant modal amplitude of the plate vibration, and 3) the vibration velocities of the plate and air flow.

A. Pressure difference over the plate

The pressure difference Δp acting on the plate includes the incident plane wave p_i, the radiated pressure from the plate into the duct p_{duct} and into the cavity p_{cav}, i.e. $\Delta p = p_i + p_{duct} - p_{cav}$. The variation in the amplitude and phase of Δp with frequency is shown in Fig. 3.3 (a) and Fig. 3.3 (b) respectively for the plate without perforations (dashed line) and with perforations (solid line).

When micro-perforations are added to the plate, the amplitude of Δp on the plate is generally reduced within the working band, with a slight shift of the curve towards higher frequencies. This is consistent with the physical explanation of the effect of the perforations by Fahy (2007). When there are perforations, pressure differences across the plate, due to the opposite phase surface sources driving fluid through the holes, partially cancel the surface volume velocities and hence sound radiation (Fahy, 2007). In the present case, with perforations on the plate Δp is partly balanced due to the

air flow through the holes, leading to a reduction in plate vibration.

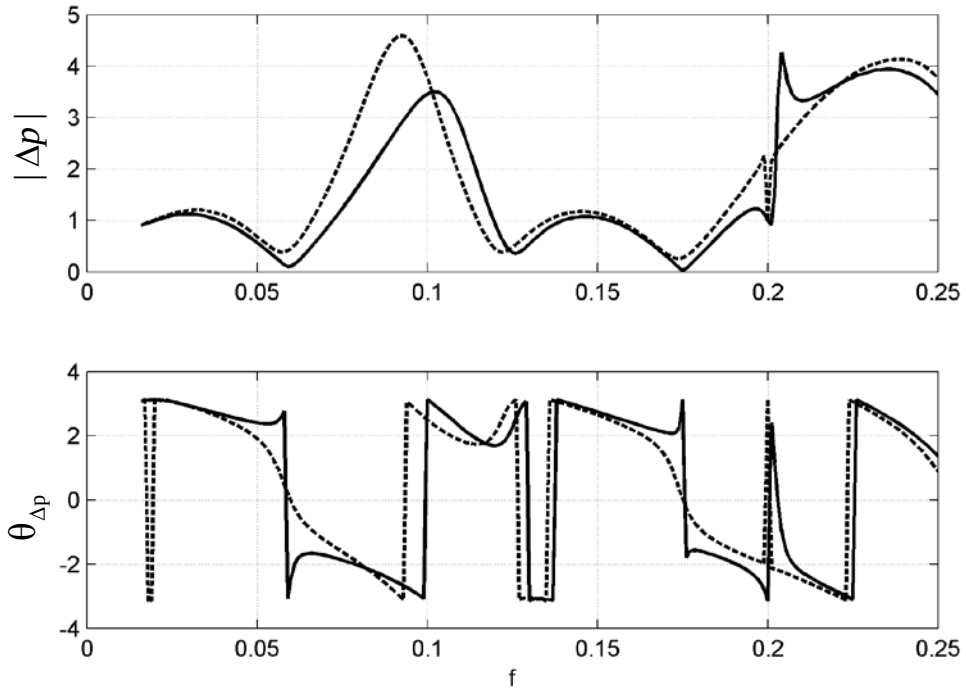

Fig.3.3 Variation in pressure difference Δp over the plate.

(a) is the amplitude and (b) is the phase.

B. Modal amplitude

Due to the change in pressure difference over the plate, which implies a variation in the driving force, the response of the plate is expected to vary. Therefore the modal amplitude $|\overline{V}_j|$ and modal reflection $|\overline{V}_j R_j|$ are to be investigated. The first column of Fig. 3.4 shows the modal amplitude $|\overline{V}_j|$ of the first three modes of the plate vibration. The responses of the plate in higher order modes are relatively weak, so they are not shown in the figure. The second column of Fig. 3.4 depicts the modal reflections $|\overline{V}_j R_j|$. The three circles and three crosses marked on the curves correspond to the frequencies of three TL peaks without perforations (dashed line) and

with perforations (solid line), respectively.

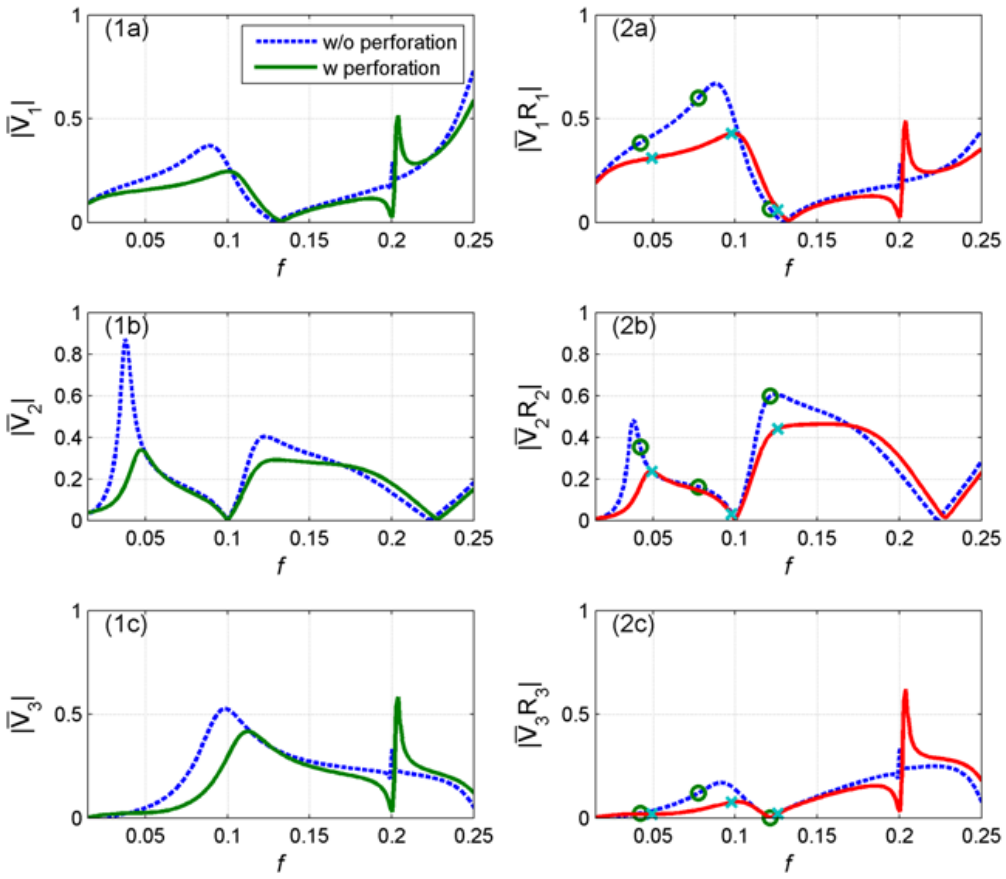

Fig.3.4 Modal Analysis. The first column is the modal amplitude $|\bar{V}_j|$ and the second column is the modal reflection $|\bar{V}_j R_j|$, j=1,2,3.

It is observed that in both cases (without and with perforations) the first peak of TL is simultaneously attributed to the first and second modes. The second peak of TL is mainly dominated by the first mode, while the third peak is due to the second modal contribution. For the micro-perforated plate, the first peak of TL is reduced as a result of a reduction in both $|\bar{V}_1|$ and $|\bar{V}_2|$, as shown in Fig. 3.4 (1a) and Fig. 3.4 (1b).

This is due to the fact that the introduction of the micro-perforations brings about a

certain degree of pressure balance across the perforated panel through the holes, seen in Fig. 3.3, so that the resulting excitation on the plate is reduced, leading to an ultimate reduction in the response of the plate. A similar trend can be observed in the variations of $\left|\bar{V}_1 R_1\right|$ and $\left|\bar{V}_2 R_2\right|$, shown in Fig. 3.4(2a) and Fig. 3.4(2b) respectively. Compared with the plate without micro-perforations, the sound reflection from the perforated plate is also reduced. It should be noted that the terminology "reflection" is being used loosely here to be consistent with previous work (Huang, 2002; Wang *et al.*, 2007). In fact, the sound is "reflected" upstream, mainly due to the radiation of the vibrating plate. In that sense, the reduced vibration response of the perforated plate due to a better pressure balance is the direct cause of the impaired sound reflection. Meanwhile, the radiation efficiency of the plate is, in principle, also impaired (Fahy and Gardonio, 2007; Putra and Thompson, 2010) due to the micro-perforations. This also contributes to the impaired sound reflection and consequently reduced TL peak values.

C. The amplitude and phase of $\bar{v}_0$, $\bar{v}$,and v_p

The phase relationship between the air vibration velocity $\bar{v}_0$ and the plate vibration v_p together with the overall velocity $\bar{v}$ for the first and second modes are shown in Fig. 3.5(1b) and Fig. 3.5(2b). Roughly speaking, the average air velocity $\bar{v}_0$ has always been in the same phase as the plate vibration. This suggests that the overall behaviour of the MPP is mainly dominated by plate vibration. The relative air motion of the perforation with respect to the plate, although critical to the sound absorption of

the MPP, is not the most dominant factor in terms of the interaction between the MPP and the surrounding acoustic media.

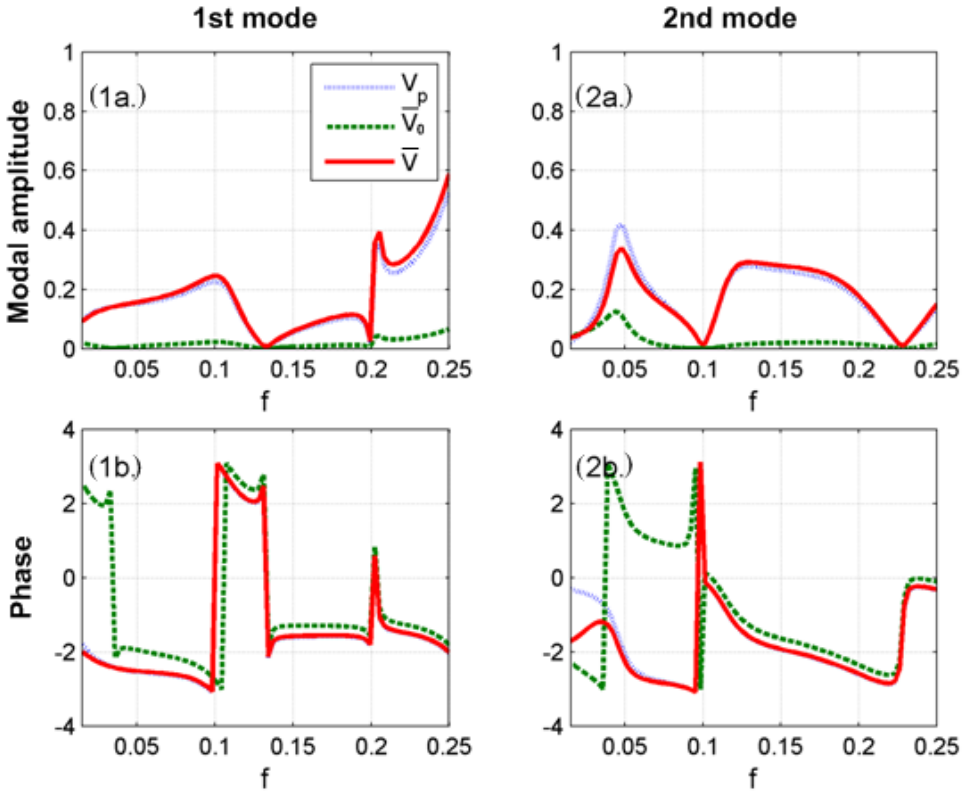

Fig.3.5 Decomposition of the air velocity $\overline{v}_0$, plate velocity v_p and the overall velocity along the plate surface $\overline{v}$ .The first and second rows show the amplitude and phase respectively.

With micro-perforations in the plate, the air velocity is very small compared with the velocity of the plate. However, the existence of the millimetre-holes balances the pressure difference working on the plates as air flows through the holes. Pressure reduction leads to the amplitude reduction of the plate vibration, and the amount of reflected sound energy is reduced correspondingly, finally resulting in the smoothing of the TL peaks.

3.3.2 Absorption coefficient of the peaks

The lifting of the TL trough is mainly attributed to the relatively significant sound absorption in that frequency range. The silencer is a complex system involving coupling among the sound field in the duct, cavity and the structural vibration of the plate. This can be best seen in terms of system impedance. Fig.3.6 shows the total reactance, with the formula ($\mathrm{Im}(Z_{jl}) = \mathrm{Im}(L_j + Z_{duct,jl} - Z_{cav,jl})$) for the first two plate modes without perforations. When cross-modal coupling is ignored, the coupled system resonates when the total reactance vanishes. The first resonance now occurs at f=0.182, which is beyond the second *in vacuo* natural frequency of the plate, from which one can see the strong coupling between the plate and the cavity due to the symmetrical nature of the first plate mode.

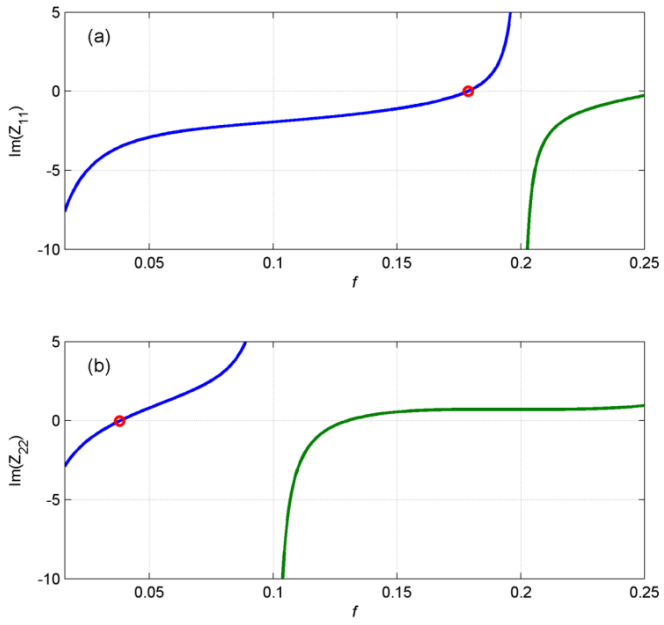

Fig.3.6 Total reactance of the first two modes. (a) Im(Z_{11});

(b)Im (Z_{22}) for which zero reactance is marked by an open circle.

The first and second resonance points found in Fig. 3.6(a) and Fig. 3.6(b) marked with circles roughly correspond to third and first peaks in the sound absorption coefficient, respectively, as shown in Fig. 3.2(c). On the other hand, the second peak of the sound absorption coefficient at f=0.104 roughly corresponds to the first cavity modal frequency, where the cavity length is a half wavelength. This will cause a strong response in the plate at the first mode. Because the cross-modal effect is ignored here, the resonance points in Fig. 3.6 may not exactly match the absorption peaks in Fig. 3.2(c). Nevertheless, perforations on the plate play an important role in the sound absorption in the system resonance, while the plate without perforations is only effective in reflecting sound in the first two modes. Therefore sound absorption at the resonance can compensates for the insufficiency in reflection at some frequency ranges for plates with a weaker bending stiffness.

3.3.3 Structural impedance

Without perforations, the dynamics of the plate with vibroacoustic coupling and the excitation force I_j can be described as follows

$$\{L_j + Z_{duct,jl} - Z_{cav,jl}\}V_{p,j} = -I_j \tag{3.1}$$

In order to investigate the effect of perforations on the structural properties, Eq. (2.33) is re-arranged into the following form

$$\{\frac{L_j}{1-\sigma}\left(1-\frac{\bar{V}_{0,j}}{V_{p,j}}\right)+(Z_{duct,jl}-Z_{cav,jl})\}\bar{V}_j = -I_j \tag{3.2}$$

where $\bar{V}_j = (1-\sigma)V_{p,j} + \bar{V}_{0,j}$ represents the smeared-out plate modal response including the average air velocity at the holes and that of the solid part of the plate.

Comparing Eq. (3.1) and Eq. (3.2), and keeping the same $Z_{duct,jl}$ and $Z_{cav,jl}$, an equivalent structural impedance of the plate with perforations $Z_{struc\_eq,j}$ can be identified

$$Z_{struct\_eq,j} = \frac{L_j}{1-\sigma}\left(1-\frac{\overline{V}_{0,j}}{V_{p,j}}\right) \tag{3.3}$$

It is clear that, apart from the mass and bending stiffness of the structure itself, $Z_{struc\_eq,j}$ is also affected by the velocity of the air motion of the perforation with respect to that of the plate. Fig. 3.7 shows the resistant part (Figs. 3.7 (1a) and (2a)), and the reactant part (Figs. 3.7(1b) and (2b)), of $Z_{sturct\_eq,1}$ and $Z_{sturct\_eq,2}$, with B=0.057 and m=1.

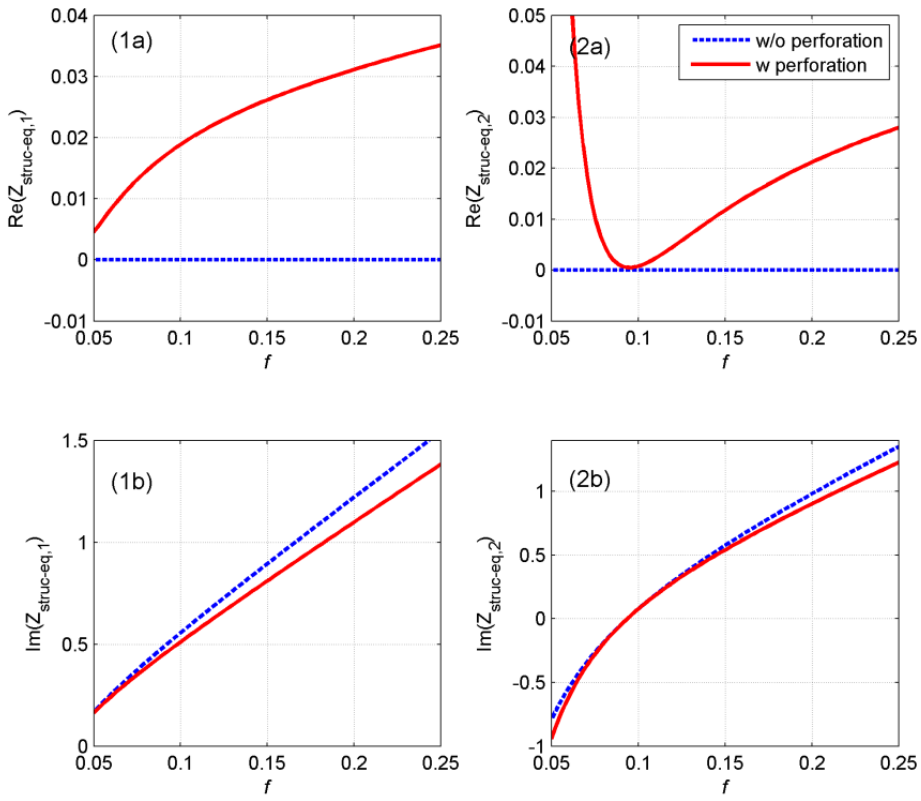

Fig.3.7 Equivalent structural impedance $Z_{struc\_eq,j}$ for the first two modes, j=1,2.

(1a) the resistant part of the 1st mode; (1b) reactant part of the 1st mode;

(2a) resistant part of the 2nd mode; (2b) reactant part of the 2nd mode.

Without perforations (dashed line) there is no resistance on the plate. Micro-perforations give rise to a resistive term for both the first and second modes, thus introducing damping on the plate. As shown in Figs. 3.7(1b) and 3.7(2b), the reactance curve appears to slightly shift to higher frequencies and the system becomes less massive for the frequency f >0.05 for the first mode and f >0.09 for the second mode. This can be regarded as a virtual negative mass effect brought about by micro-perforation. Due to the decrease in the effective mass in the structural impedance in the second mode, the resonance of the system is shifted towards a higher frequency. This is the reason why the modal reflection $\left|\overline{V}_j R_j\right|$ and the reflection coefficient β curves are shifted to higher frequencies when micro-perforation is added. Such a high frequency shift results in a higher band limit f_2, and subsequently the widening of the stopband.

3.4 Optimization of TL performance

The absorption provided by the micro-perforation is controlled by parameters such as the hole diameter and perforation ratio. They in turn affect the coupled system impedance, sound reflection, sound absorption and ultimately the TL performance. Therefore, the optimization of the variables is necessary to achieve the best performance of the silencer. These variables are basically divided into three categories: the first is geometrical variables such as the length and height of the cavity and the height of the duct; the second category is related to structural properties, such as the bending stiffness and the mass ratio of the plate; while the third category is the

perforation parameters such as perforation ratio and diameter of the hole. Huang (2005) introduced the use of a cost function for optimization in order to search for the optimal cavity length to height ratio. Choy (2005) and Wang (2007, 2008) adopted the cost function when conducting the optimization procedure in order to determine the appropriate structural properties of the membrane and plate for a drumlike silencer and plate silencer respectively. In the following sections, optimization is carried out by fixing some variables such as the length of the plate ($L = 5$), the cavity depth ($h_c = 1$), and the height of the duct (h=1).

3.4.1 Structural properties

In this section, the structural properties of the mass ratio and bending stiffness of the plate are investigated. When there are perforations, the parameters concerning the perforations such as the perforation ratio and hole size are fixed at σ=0.5% and d=0.004 respectively.

A. Bending stiffness

Fig. 3.8 displays the TL spectra varying with different bending stiffnesses for fixing of m=1. The resonant frequencies shift towards higher frequencies when the bending stiffness is increased. When the bending stiffness is small (B=0.03) shown in Fig.3.8(a), the serious trough between the second and the third peaks makes the working bandwidth of the silencer relatively narrow. When the bending stiffness increases, the trough is lifted accordingly such that the average transmission loss

increases. However, when the bending stiffness is too high (B=0.08) shown in Fig.3.8(f), the second and third peaks merge together and then the TL drops. This is probably because the plate has a very high bending stiffness and it is difficult to be excited, especially for the first mode which contributes to the second peak of the TL. As a result, for the present case the optimal bending stiffness B is found to be around 0.6 to 0.7 because the spectral valleys between the three peaks rise above TL_{cr}, as shown in Fig. 3.8(d) and Fig. 3.8(e).

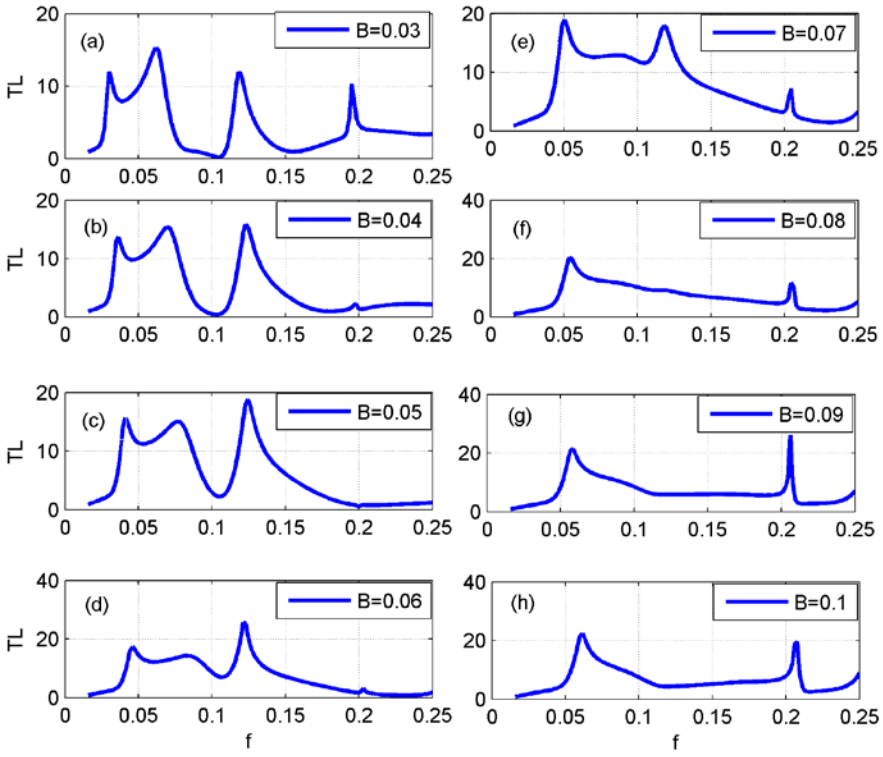

Fig.3.8 Variation of TL with different bending stiffnesses

In order to determine a more accurate value of the bending stiffness, the corresponding variation in different stopbands for different bending stiffnesses is investigated. Figs. 3.9(a) and (b) show the lower limit f_1 and the working bandwidth f_2/f_1 as a function of bending stiffness B respectively for fixing m=1. As shown in Fig.

3.9(a), the lower frequency limit f_1 increases with B. This is because the increase in bending stiffness B will shift the whole spectra towards higher frequencies due to the shift in resonance frequency. As shown in Fig. 3.9(b), the working bandwidth increases with bending stiffness and then drops until B=0.07. This reveals that the widest working bandwidth can be achieved with the proper tuning of the bending stiffness. The bending stiffness required cannot be too high, such as B=0.1 shown in Fig. 3.8(b), because the plate is hard to excite.

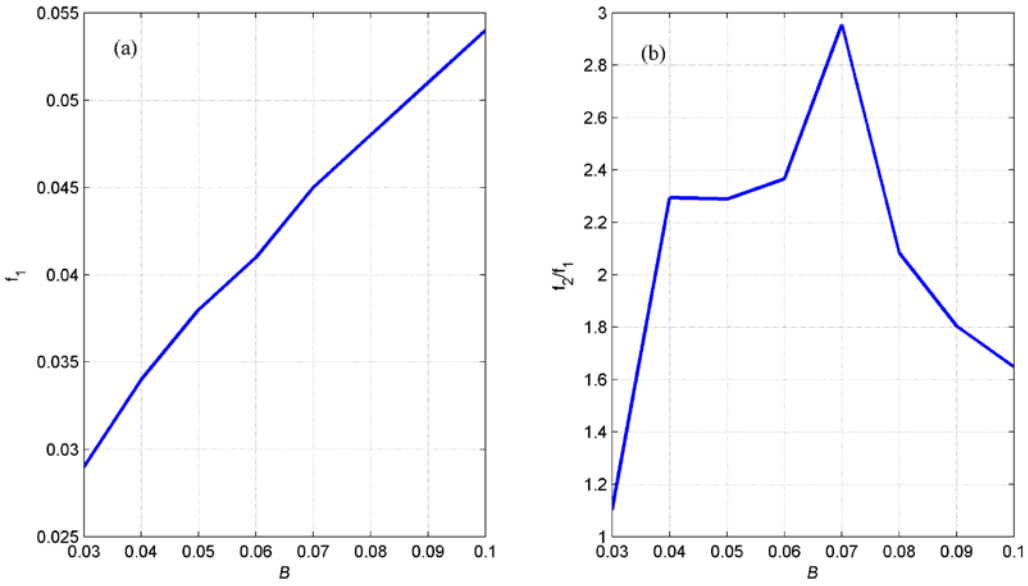

Fig.3.9 Variations of f_1 and f_2/f_1 with B

B. Mass ratio

The effect of the plate mass is shown in Fig. 3.10 for given plate bending stiffnesses B equalling to (a) 0.04, (b) 0.06, (c) 0.07 and (d) 0.09. The spectra of the heavier plates are shifted towards lower frequencies compared to that of lighter plates. However, such a shift cannot help improve the overall performance of the silencer, because the width of the trough is relatively wide for the heavier plate, which results in a narrower

stopband. For example, as shown in Fig. 3.10(c), the plate with m=1 achieves a good performance with B=0.07. For the same bending stiffness, the TL spectrum has serious dip with m=3. Fig. 3.10(d) shows that when the plate is maintained at m=3, the trough as well as the peak are lifted for high values of bending stiffness with B=0.09. This indicates that increasing B is helpful for improving the stopband when the mass is high.

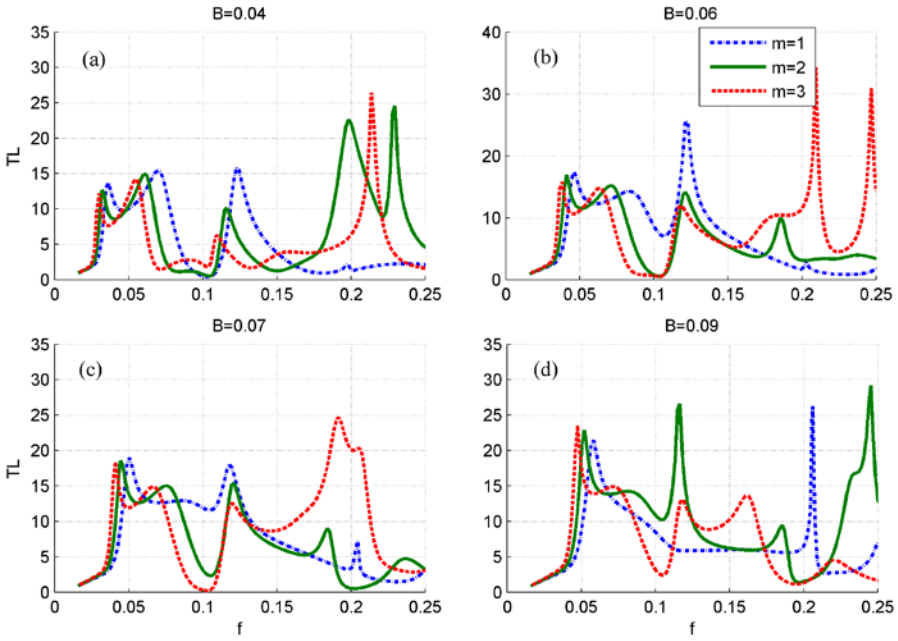

Fig.3.10 Variation in TL spectra with different mass ratios and different bending stiffnesses

Fig. 3.11 depicts the optimal bending stiffness B_{opt}, the corresponding lower frequency limit f_1 and the working bandwidth f_2/f_1 as a function of the mass ratio. Fig. 3.11(a) suggests that the optimal bending stiffness increases with plate mass. The trend is the same as the plate silencer without perforations (Wang, 2007). Wang (2007) showed that for a plate without perforations (m=1), the optimal bending stiffness was found to be B=0.07. In the current study, Fig. 3.11(a) shows that the optimal bending

stiffness for a plate with perforations (σ=0.5% and d=0.004) is found to be B=0.065. There is a slight decrease in the value of the bending stiffness compared with a plate without perforations. This is because part of the sound energy is dissipated by the micro-perforations so that the required amount of reflected sound energy is reduced accordingly. As shown in Fig. 3.11(b), when the mass of the plate increases, the lower band limit f_1 increases. This effect is undesirable for a plate silencer designed for low-frequency noise control. Nevertheless, f_1 still remains within the low frequency region. For example, when m=4, f_1=0.052, for a duct with a height of 10 cm, the dimensional lower band limit is f_1^*=176 Hz. As shown in Fig. 3.11(c), the maximum bandwidth f_2/f_1 decreases gradually when the mass of the plate is increased. When m=4, the maximum bandwidth is 2.22, which is still larger than one octave.

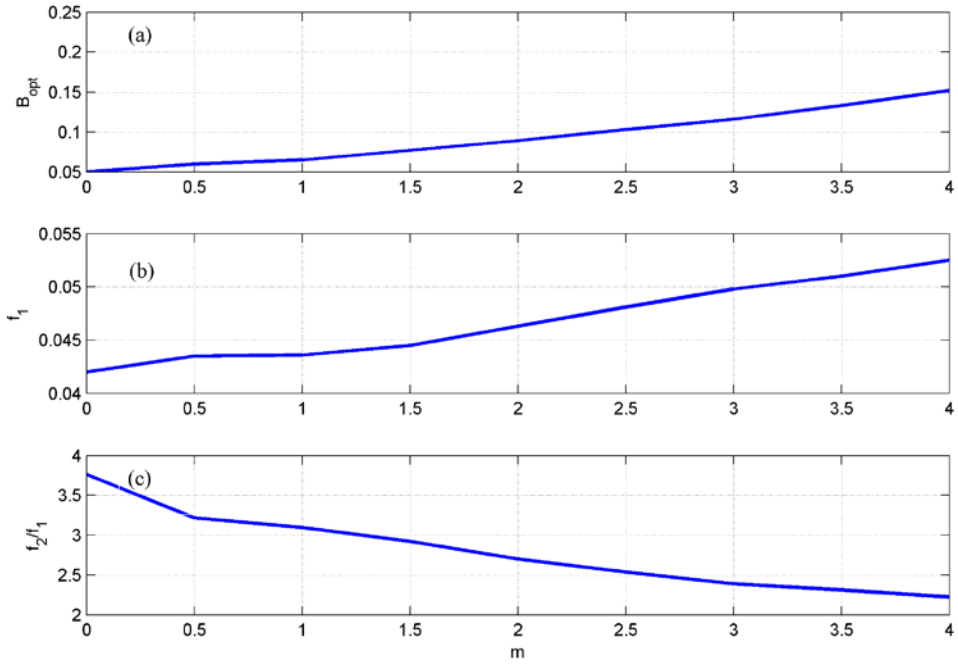

Fig.3.11 Parameters variation with mass ratio of the plate silencer with micro-perforation.

(a) optimal bending stiffness B_{opt}; (b) the corresponding lower band limit f_1.

(c) the corresponding working bandwidth f_2/f_1.

3.4.2 Perforation parameters

Perforations play an important role in the improvement of the performance of the plate silencer. First of all, the holes on the plate can dissipate sound energy, and with perforations on the plate, Δp is partly balanced due to the air flow through the holes, leading to a reduction in plate vibration. The working mechanism cannot be simply described by the resistance and reactance of the MPP. In contrast, the effect of the perforations on the performance of the plate silencer can be studied by observing the variation in the TL spectrum as a function of the perforation parameters.

A. Diameter of the holes

From the previous study of the structural properties of the plate, m=1 and B=0.06 are found to be appropriate to contributing to the good performance of the plate silencer with perforations. Therefore, in this section the following values are set: B=0.06, m=1 and σ=0.5%. The variation in TL spectrum as a function of the diameter of the hole is shown in Fig. 3.12. It shows that with micro-perforations there are two opposite actions between the TL peaks and trough. The amplitude of the TL peak is reduced and the trough between the second and third peaks is lifted. The level of lifting of the trough is increased when the diameter is increased from 0 to 0.012. However, when d reaches 0.015 (solid line), the trough start to drop slightly and as a result TL is also reduced. This may be due to the pressure difference being mostly balanced by the large holes, and consequently the vibration of the plate deteriorates.

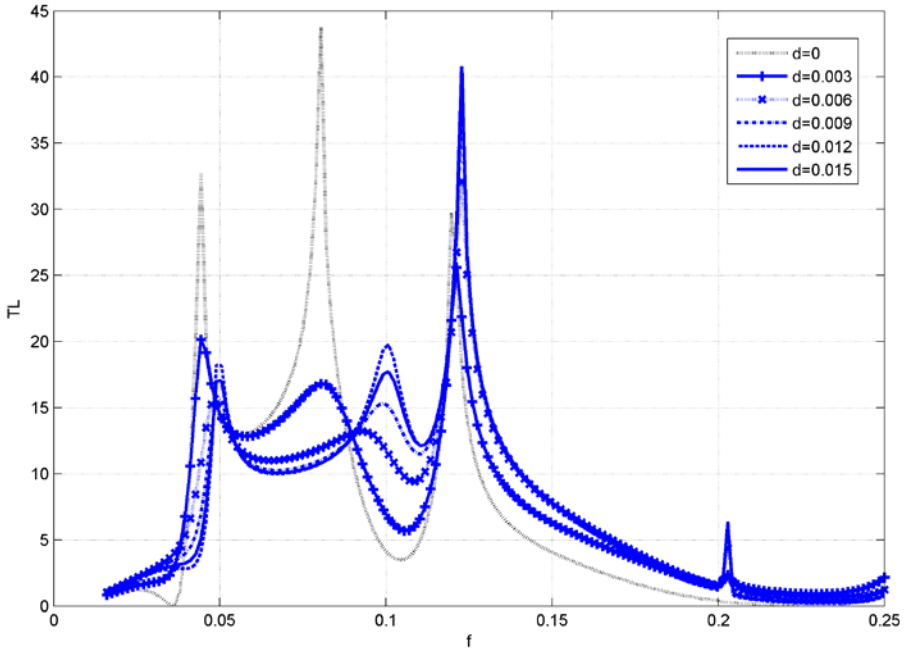

Fig.3.12 TL spectra with different diameters of hole

B. Perforation ratio

Fig. 3.13 shows the variation in TL spectra as a function of the perforation ratio by fixing B=0.06, m=1 and d=0.005. When σ is increased from 0% to 0.5% the TL peak is obviously reduced, but the trough is lifted. This results in a more flattened and uniform TL performance. When σ equals 5%, TL is decreased, especially in the low frequency range f <0.1. As a result, the performance is similar to the expansion chamber. It is attributed to the large amount of holes balancing the air pressure on the plate and sound penetration through such a large amount of holes.

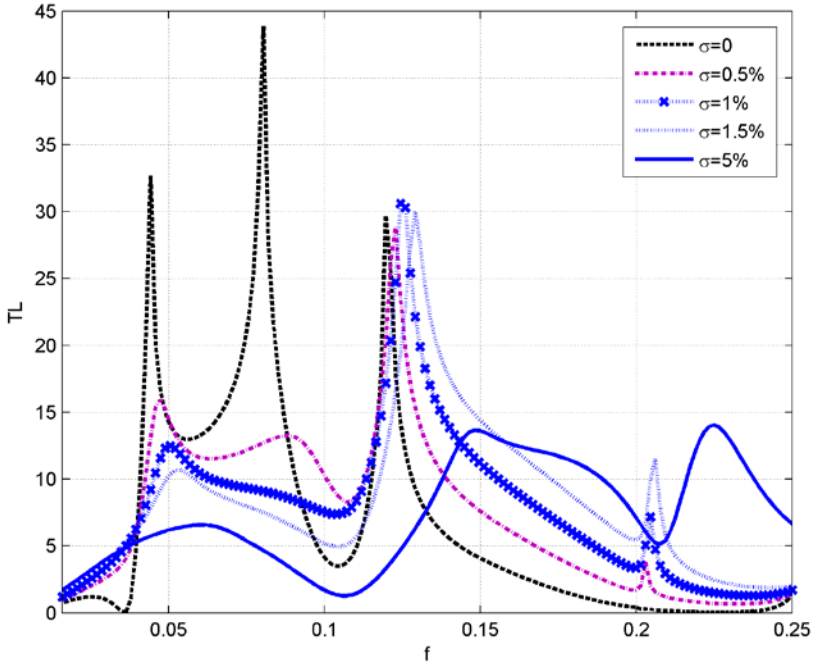

Fig.3.13 TL spectra with different perforation ratios of the hole

Fig. 3.12 and Fig. 3.13 reveal that TL performance is influenced by the perforation parameters. With the appropriate tuning of the hole size and perforation ratio, the desired TL performance can be obtained. TL performance is attributed to the compromise between sound reflection and absorption. Therefore the corresponding reflection coefficient β and the absorption coefficient α are also to be investigated for different perforation ratios. Fig. 3.14 (a) and Fig. 3.14(b) show the reflection coefficients and absorption coefficients respectively by assuming very a large bending stiffness of the plate. In this manner the plate is hard to excite, so reflection due to plate vibration is excluded, and focus can be fully paid to energy dissipation due to MPP. It is noted that m=1 and d=0.005 are set in this study. When there is no perforation (solid line), β and α are both zero, as shown in Fig. 3.14(a) and 3.14(b) respectively. This is because the plate is considered as a rigid wall of the duct with the

plane wave travelling. Fig. 3.14(a) shows that even if there is no vibration of the plate, reflection still occurs when there is perforation due to the change of impedance. However when σ is further increased to 5%, there are two loops from f = 0 to f = 0.2 in the reflection coefficient shown in Fig. 3.14(a), which is similar to the performance of an expansion chamber. The peaks of absorption coefficient, shown in Fig. 3.14(b), are mainly due to the resonance of the coupled system, which is already explained in Sec. 3.3.2. The absorption coefficient in the frequency range of the TL trough is relatively high and plays the role of compensating for insufficient reflection such that the TL trough can be raised to achieve the optimal wide stopband.

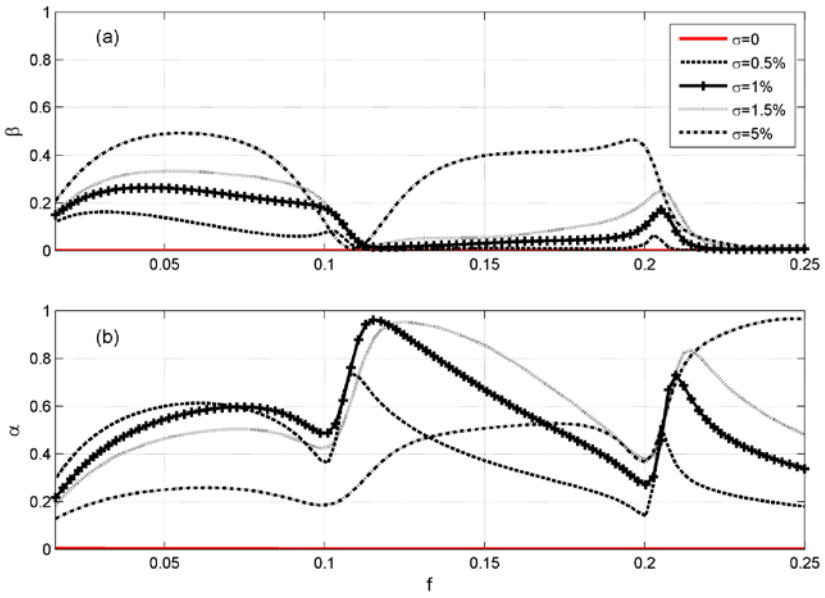

Fig.3.14 Variation of reflection coefficient and absorption coefficient with plate vibration excluded.

3.4.3 Pressure difference

The variation in the pressure difference by tuning of the perforation ratio is studied in this section. As mentioned in Sec. 3.3.2, the perforation plays an important role in

providing a dissipative mechanism and partially balancing the acting force on the plate. Fig. 3.15 shows the variation in the pressure difference over the plate for different perforation ratios. The pressure difference over the plate generally decreases with an increase in the perforation ratio. With the selection of the appropriate perforation ratio there is high energy dissipation when the air passes through the holes. At the same time there is certain level of balancing of the pressure on the top and bottom of the plate through the holes. It will restrict the motion of the plate and hence the sound reflection. Therefore these two mechanisms mutually affect each other. To achieve optimal TL performance, the perforation parameters should be tuned with consideration of both effects.

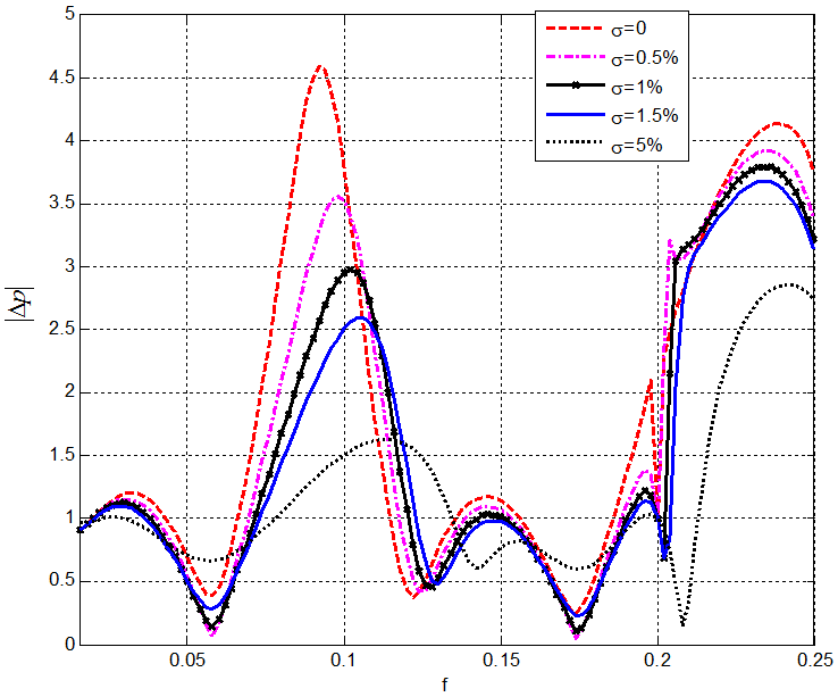

Fig.3.15 Variation in pressure differences at different perforation ratios

3.4.4 Optimal bending stiffness and perforation parameters

In the previous section, the bending stiffness of the plate is fixed and different perforation parameters affect the sound reflection, sound absorption and TL performance. Therefore, the optimization of the parameters of the micro-perforated plate is necessary to achieve the best performance of the silencer. Fig. 3.16 depicts the variation in bandwidth f_2/f_1 as a function of the optimal diameter of the holes and perforation ratio for different bending stiffnesses. Three curves represent the search results for an optimal bandwidth with three typical bending stiffnesses.

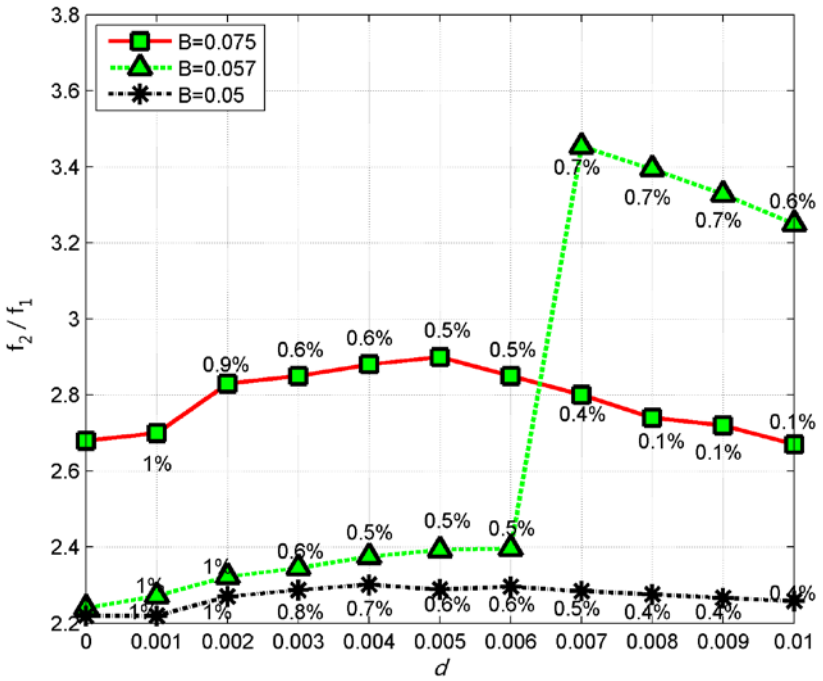

Fig.3.16 Optimization curve for different bending stiffnesses. The percentage on each point shows the perforation ratio to achieve the optimal f_2/f_1 with corresponding diameter.

For a plate with a relatively weak bending stiffness B=0.05 (dashed line with stars),

the corresponding stopband remains at around f_2/f_1=2.22 with very slight dependence on hole size and perforation ratio. This is because the trough between the second and third peaks in the TL spectrum (not shown here) are at a very low level, and consequently the addition of micro-perforations does not lead to any significant increase in the TL at the trough point. For a very high bending stiffness B=0.075 (solid line with squares), without perforations, the optimal stopband is relatively wide f_2/f_1=2.68. When micro-perforations are added, the stopband remains in the range 2.7 to 2.9. This means that the high bending stiffness of the plate itself can support the strong sound reflection. This effect alone can already substantiate a relatively broad stopband. The relative velocity of the holes and perforated plates cannot significantly influence structural impedance due to the dominance of such a high bending stiffness. Therefore there is no tremendous change in the stopband when micro-perforations are introduced onto the plate. The significance of the micro-perforations can be best seen when the bending stiffness of the plate falls into the intermediate range. With B =0.057 (dashed line with triangles) excessively small perforation holes (d<0.006) cannot significantly increase the stopband (typically ranging from f_2/f_1=2.2 to 2.4). On the other hand, when the size of the hole is further increased to d=0.007 with the optimal perforation ratio σ=0.7%, the stopband is drastically increased to f_2/f_1=3.45. One can see an obvious change in the stopband for a hole size varying from d=0.006 to d=0.007 with the proper selection of perforation ratio. The above analysis seems to suggest that, in order for the micro-perforations to have a dominant effect in enlarging the stopband of the silencer, a minimum level of bending stiffness of the plate is

required. This will ensure a minimum sound reflection in some frequency regions, whilst deficient ones will be taken care of by the micro-perforations. When properly designed, this plate silencer with micro-perforations can provide a stopband which is even larger than a conventional plate silencer with a much higher stiffness, by finding the balance between reflection and absorption.

3.5 Summary

Numerical analysis of the performance of the plate silencer with micro-perforations has been conducted in this chapter. The micro-perforations have been found to smooth the TL peak, lift the TL trough, and expand the working bandwidth. As a result a more uniform TL spectrum can be achieved. Due to the contribution of the energy dissipation by the MPP, the insufficiency in reflection can be compensated when the bending stiffness of the plate is relatively weak. Therefore the harsh requirement for bending stiffness is released by 20%. The effects of the micro-perforations are threefold:

1). The perforation plays an important role in providing a dissipative mechanism and partially balancing the pressure between the two sides of the plate. Therefore there is compromise between the sound radiation capability due to the weaker response of the plate and sound dissipation due to the existence of the perforations. As a result, the sharp peaks on the TL curve provided by original plate silencers are smoothed out. The physics behind has been discussed through the analysis of the pressure

difference over the plate, variation in the air and plate vibration velocities and modal amplitude.

2). Micro-perforation contributes sound absorption capability to the system. With the help of sound absorption, the original TL trough point between the second and third peaks can be lifted for a plate with lower strength due to insufficient sound reflection. This results in broadening of the stopband.

3). Micro-perforation allows a reduction in the reactance of the equivalent structural impedance, like a virtual negative mass. This results in a shift of the system resonance to higher frequencies that lead to a widening of the stopband. Together with the effects mentioned in a) and b), a more flattened/uniform broadband silencer can be achieved.

Moreover, optimization of a plate silencer with micro-perforations has been carried out. The TL spectrum shifts to a higher frequency with an increase in bending stiffness and shifts to a lower frequency with an increase of mass due to the resonance of the system. The perforation parameters such as perforation ratio and diameter of the holes have also been studied, which offer guidelines for optimization. With a proper bending stiffness and optimal perforation parameters, a silencer of moderate bending stiffness can provide a wide stopband that outperforms the conventional plate silencer with very high bending stiffness.

CHAPTER 4

EXPERIMENTAL INVESTIGATION

4.1 Introduction

A theoretical model of a plate silencer with micro-perforations has been developed in Chapter 2. Dynamic equations, capable of dealing with vibro-acoustic coupling, are established. The working mechanism is analysed in Chapter 3. When the micro-perforations are introduced into the plate silencer, sound absorption attributed to the micro-perforations can compensate for the insufficiency of sound reflection contributed by a plate of lower stiffness. However, the plate vibration is simultaneously reduced due to the pressure balance through the holes, thus the reflected sound energy is reduced. By properly choosing the perforation parameters, the balance between absorption and reflection can be explored. Furthermore, the working band is expanded to higher frequency due to the virtual negative mass effect brought about by micro-perforation. With these effects, a more uniform and broader band noise control performance can be achieved.

In this chapter an experimental study is carried out. The purpose of which is to validate the two-dimensional theoretical model established in Chapters 2 and 3. In doing so, the silencing performance of a prototype clamped plate silencer is tested experimentally using a reinforced polymathacrylimide (PMI) plate. There are several

issues involved. Firstly, the fabrication of the composite plate is a complicated task. The foam chosen for this study is closed-cell rigid foam based on polymathacrylimide (PMI). Carbon fibre is adhered to the PMI to reinforce the bending stiffness of the foam. Secondly, the sub-millimetre holes need to be drilled in a proper way. In this study a laser machine is chosen, and it is noted that the working power of the laser machine should be properly tuned to drill the holes. If the power is too high the foam will over-melt, or if the power is insufficient the laser will fail to drill holes. Thirdly, the installation should be very precise, as the three-dimensional test rig is set up to validate the two-dimensional model. Sound waves travel through the duct along the *x*-axis and the plate vibrates transversely along the *z*-axis. Thus for the *y*-axis, which is perpendicular to the figure, the two edges of the plates are inserted into a very thin gap between the cavity walls. The gap should be carefully adjusted to avoid sound leakage as well as the plate touching either the cavity wall or the duct wall.

4.2 Experimental set-up

The experiment is carried out using the two-load method with four microphones.

4.2.1 Two-load method

The set-up for the two-load measurement is shown in Fig. 4.1. Four travelling waves are considered to be plane waves at a distance sufficiently far away from the junctions.

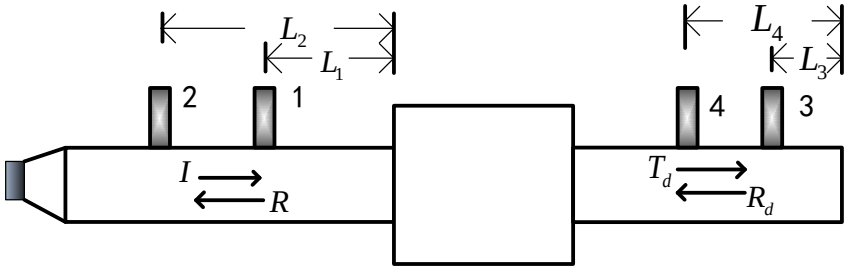

Fig.4.1 Configuration of two-load method

The sound pressure upstream and downstream of the chamber both consist of incident and reflected waves, whose complex amplitudes are denoted by *I*, *R* in the upstream duct and T_d and R_d for the downstream duct. If the first and second microphones are placed at a distance of L_1 and L_2 from the first junction, as shown in Fig. 4.1, the measured pressures can be expressed as follows

$$p_1 = J_1 A_1 e^{i\omega t} = I e^{i(\omega t + kL_1)} + \mathrm{R} e^{i(\omega t - kL_1)} \tag{4.1}$$

$$p_2 = J_2 A_2 e^{i\omega t} = I e^{i(\omega t + kL_2)} + R\, \mathrm{e}^{i(\omega t - kL_2)} \tag{4.2}$$

In which A_1, A_2 are digital readings in voltage, and J_1 and J_2 are the transfer function between the signal voltage and the real sound pressure in Pascal units. The amplitude of the travelling waves is found by solving Eq. (4.1) and Eq. (4.2), as

$$I = \frac{J_1 A_1 e^{-ik(L_1+s)} - J_2 A_2 e^{-ikL_1}}{e^{-iks} - e^{-iks}}, R = \frac{-J_1 A_1 e^{ik(L_1+s)} + J_2 A_2 e^{-ikL_1}}{e^{-iks} - e^{-iks}} \tag{4.3}$$

where $s = |L_2 - L_1|$ is the separation between the two microphones. Similarly, the transmitted sound T_d and the reflection R_d are found by measurement at microphones 3 and 4.

Furthermore, two measurements are taken for two downstream boundary conditions. The first is for a rigid boundary, with the results indicated by subscript ‘rig’. The

second is for an absorption boundary, and the results are indicated with ‘abs’. Downstream reflection $R_d = R_{drig} + \varsigma R_{dabs}$, where ς is any complex constant. A virtual anechoic condition at the downstream end can be achieved if the constant is such that $R_d = 0$. So

$$\varsigma = -\frac{R_{drig}}{R_{dabs}} \tag{4.4}$$

With this constant the resultant incident wave and transmitted wave amplitudes with anechoic termination become

$$I = I_{rig} - \frac{R_{drig}}{R_{dabs}} I_{abs}, T_d = T_{d\,rig} - \frac{R_{drig}}{R_{dabs}} T_{d\,abs} \tag{4.5}$$

The transmission loss TL is

$$TL = 10\log_{10}(|\frac{I}{T_d}|^2) = 20\log_{10}|\frac{I_{rig} - \frac{R_{drig}}{R_{dabs}} I_{abs}}{T_{d\,rig} - \frac{R_{drig}}{R_{dabs}} T_{d\,abs}}| \tag{4.6}$$

4.2.2 TL measurement

The experimental set-up is shown in Fig. 4.2. The incident noise is generated by a loudspeaker connected to the duct through a contraction cone. The output signal from the DA converter (NI.PCI-M10-16E-1) is passed to the loudspeaker via a B&K power amplifier. Two pairs of 1/2in, phase-matched microphones (B&K 4187) connected with conditioning amplifier (B&K Nexus 2691), labelled M1~M4, are used. The separation distance between the microphones is 80 mm. Signals from the microphones are acquired through an A/D converter (NI-PCI-4452). Both A/D and D/A processes are controlled by the NI Labview program and are run on a loop of discrete frequency

generation from 50 Hz to 1000 Hz with a increment of 10 Hz. Two independent different downstream loading conditions are used to simulate the physical anechoic termination. In the present study, the first downstream boundary condition is a simple “rigid ending”, while the other one is an “absorbing ending”, which is realized by connecting the downstream end of the duct to an absorptive chamber.

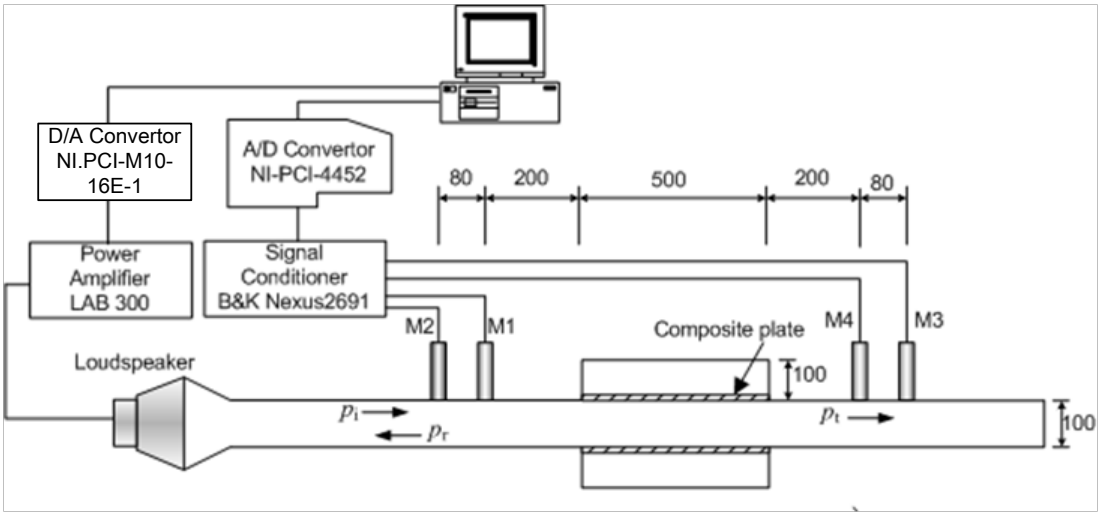

Fig.4.2 Experimental set-up

The duct wall is made of 15-mm-thick acrylic so that it can be assumed to be acoustically rigid. The cross-section of the duct is 100 mm x 100 mm and the corresponding cut-on frequency of the duct is about 1700 Hz, which is much higher than the upper limit of the measurement frequency range. The two cavities also have a cross-section of 100 mm x 100 mm and length of 500 mm. A photo of the plate silencer is given in Fig. 4.3.

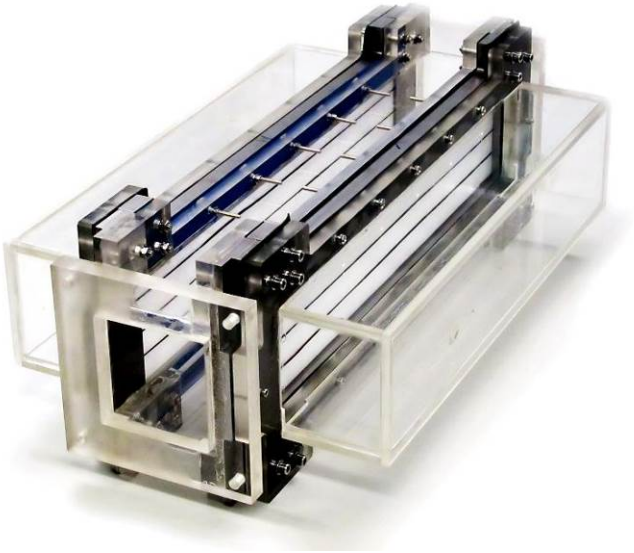

Fig.4.3 Image of the plate silencer

The two lateral edges of the plates are inserted into a thin gap between the cavity and duct walls. The gap should be delicately tuned, for if it is too small the vibration of the plate is affected by the plate touching the edges, while if the gap is too large sound leakage of noise from the main duct to the cavities would occur.

Before measuring the TL of the plate silencer, the TL of the whole system without the plate is first measured. There are two purposes for this measurement; one is to calibrate the system and the other is to check the damping of the duct and cavity. The TL spectrum, the reflection coefficient β and the absorption coefficient α are measured and compared with the theoretical predictions in Fig. 4.4.

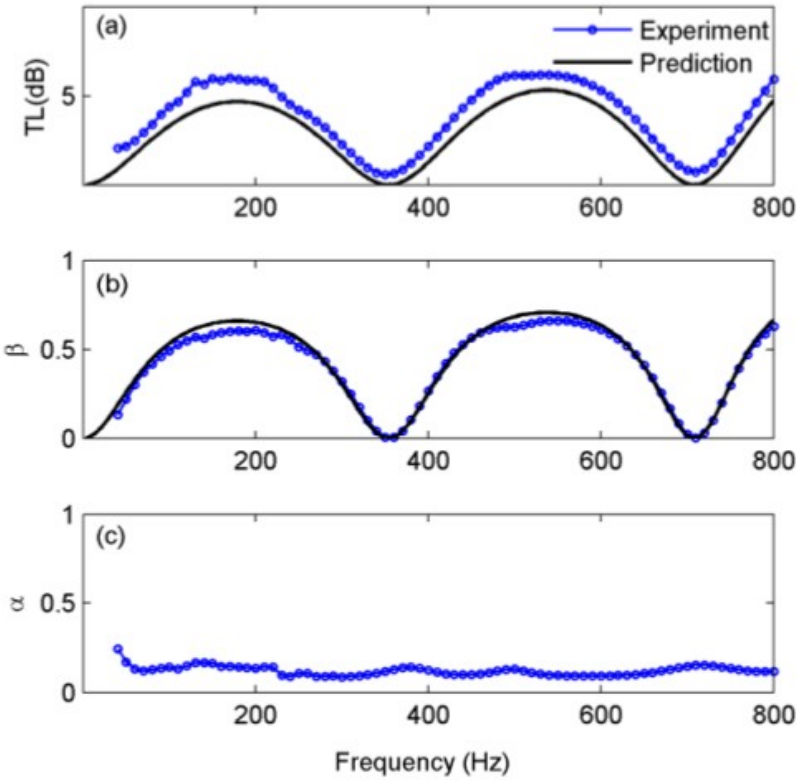

Fig.4.4 Performance of the expansion chamber.

Without the plate the plate silencer becomes an expansion chamber with a cross-sectional area ratio of 3 with respect to the main duct. Fig. 4.4(a) shows that the measured TL matches the theoretical prediction well, except that the measured TL is about 0.5 dB higher that that predicted. This is mainly due to the energy dissipation mechanisms which are excluded in the theory but inevitably exist in the rig. As shown in Fig. 4.4(c), the overall absorption coefficient of the expansion chamber is around 0.1. The possible damping mechanism includes the damping of the cavity and by sharp edges, the wall vibration, etc. In general, the absorption coefficient is small and sound reflection dominates.

4.3 Material investigation

Two pieces of composite plate made of Polymathacrylimide (PMI) with the carbon fibre (CF) reinforcement tows are installed flush with the duct (Choy *et al.*, 2012). The plate is 520 mm long, 104 mm wide and 4 mm thick. The leading and trailing edges of the plates are clamped, and the effective length of the plates is 500 mm.

The foam chosen for the present study is closed-cell rigid foam based on polymathacrylinide (PMI). This low-density foam has excellent mechanical properties over a wide range of temperature up to 220°C. PMI foam (Rohacell® core foam) has excellent dynamic strength, and the cell size can be tailored for different processing methods. The foam has easy shape formability by conventional machining techniques, such as milling, drilling, sanding and turning, which makes it suitable for a wide variety of applications in the fields of medicine, automotive engineering, wind energy and sport. In this study, PMI IG-31 foam plates (density of 35 kg/m^3) with a thickness of 4 mm are chosen. On the other hand, a unidirectional carbon fibre (CF) tow of 0.08g per tow is chosen for attachment on both the top and bottom surface of the PMI plates. It is selected as reinforcement due to its light but stiff characteristics. Epoxy AA3041 from Chematco (Hong Kong) Ltd. is used for the adhesion of the reinforcement to the core materials. Fig. 4.5(a) shows how the three CF tows are attached onto the core plate. The CF tows are laid with equal spacing on the plate either on the top or bottom surface. Such an arrangement may give an improved, even distribution of mass and bending stiffness. Fig. 4.5(b) presents a photo of the

configuration of the PMI foam plate reinforced with CF.

(a)

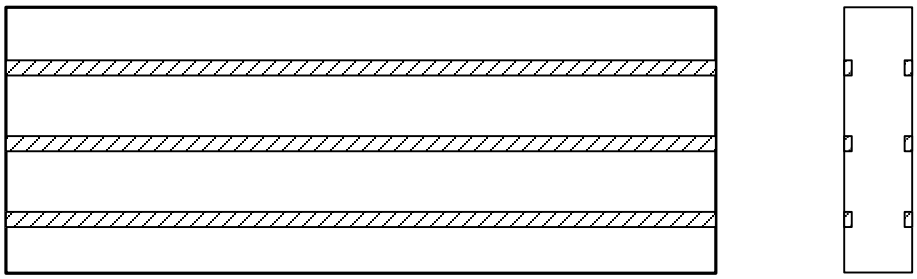

(b)

Fig.4.5 Composite plate: (a) method of adhering CF to PMI plate,

(b) image of PMI plate reinforced by CFs.

The composite plates were fabricated by hand lay-up technique, and each composite plate was left to cure at room temperature for 5 days with a certain amount of pressure applied, which can ensure that the reinforcement was well bonded with the core material and a flat surface for the specimen could be achieved.

A flexural (3-point bending) test was performed on the samples according to ASTM standard (ASTM C393) to obtain the average value of the bending stiffness of the composite plate. The dimensions of the plate were 200 mm x 105 mm. The samples were mounted on the MTS Alliance RT/50 testing machine, and the schematic of the three-point bending test is shown in Fig. 4.6(a). The span length of the samples was 150 mm, and the test speed was set to 6 mm/min. Load was increased gradually on the

sample. An example of the relationship between the applied load and the deflection at the mid-point of the plate is shown in Fig. 4.6(b). The response of the plate is reasonably linear as deflection increases from 0 to 1.5 mm.

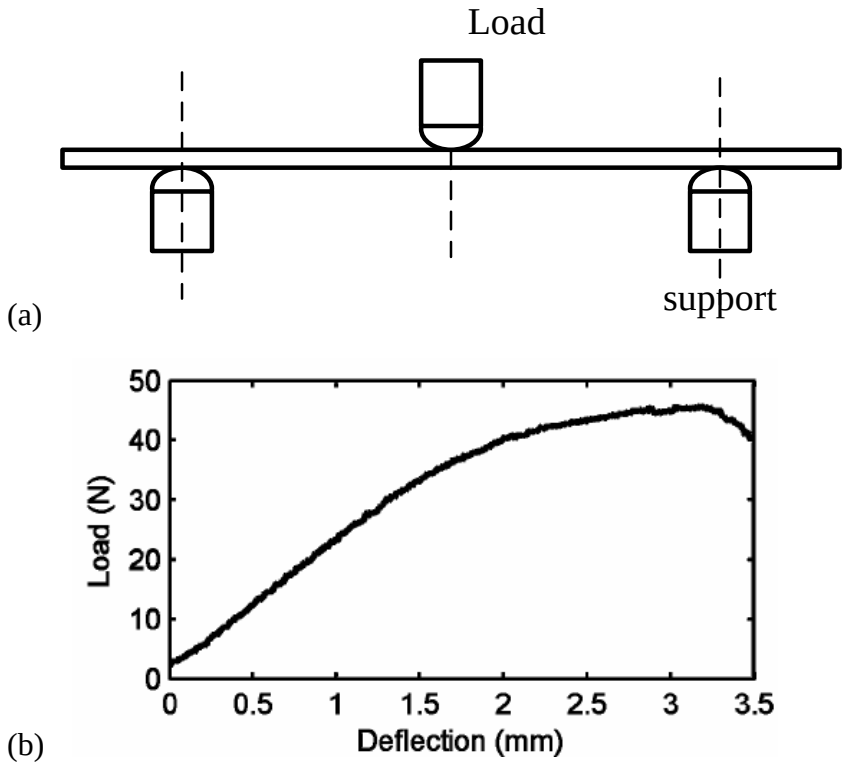

Fig.4.6 (a) Configuration of the three-point bending test; (b) a result from the test

Hence the measured data within this region are used to determine the Young's modulus. The bending stiffness of the plate can be calculated as

$$z = \frac{FL^3}{48YI} \tag{4.7}$$

where z is the deflection, F is the load applied, Y is the Young's modulus of the plate, and I is the second moment of inertia of the plate.

Fig. 4.7 shows the test results on a small sample of the composite plates with

difference numbers of CF. The carbon fibres reinforce the bending stiffness; however the mass is also increased. So the fabrication of the composite plate should be precise in order to control the amount of glue and to ensure the firm connection between the plate and the carbon fibre.

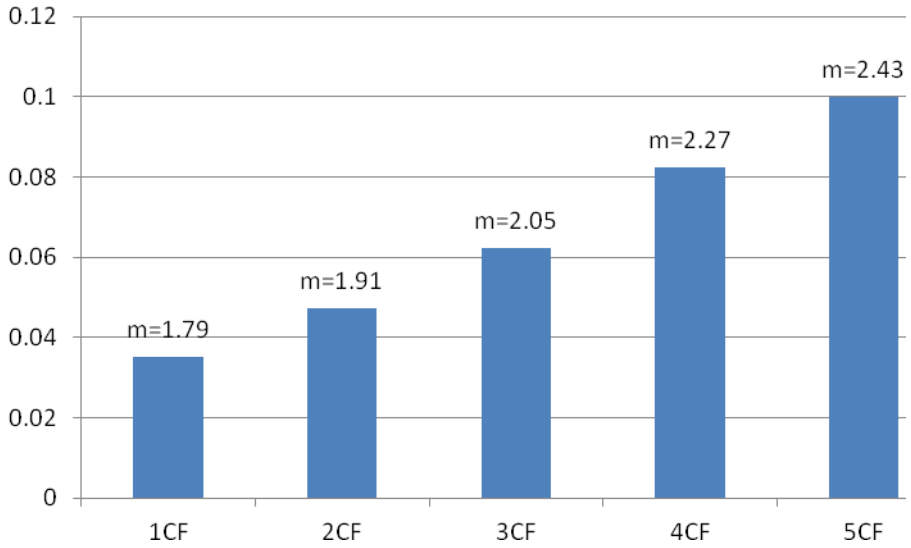

Fig.4.7 Mass ratio and bending stiffness of the composite plate

After the manufacture of the composite plates, the plate is drilled by laser machine. The Legend 36 EXT laser is chosen for drilling the holes. The working power of the laser should be properly regulated. If the power is too high the PMI foam will over-melt with extremely large and irregular holes, while if insufficient power is used the laser is not able to pass through the plate. Thus 8% of the maximum laser power is chosen by trial and error, which is 9.6 Watts.

The installation of the plate is also very important. In fact it is a crucial factor during the experiment, as shown later in Sec. 4.4. As mentioned previously, this 3D

experiment is carried out to validate the 2D model. The lateral edges of the plate should not touch the edge of either the cavity or duct, but the width of the plate should be slightly wider than the width of the cavity to prevent sound leakage. The installation is shown in Fig. 4.8.

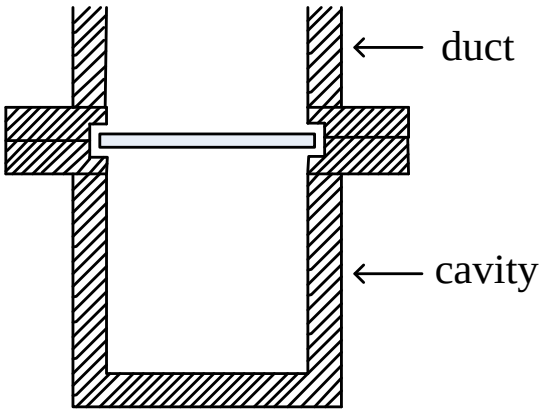

Fig.4.8 Cross-section of the plate installation

4.4 Results and analysis

Fig. 4.9 shows the measured TL of the plate with and without perforations of σ=0.5% and a hole size of 0.4 mm. The parameters of the composite plate are given in Table 4.1.

Table 4.1 Parameters for the composite plate

Length (mm)	520
Width (mm)	104
Thickness (mm)	4
Density of PMI (kg/m^3)	35
Number of carbon fibres (per surface)	5

Roughly speaking, the measured TL of the plate without perforations agrees quite well with the tendency predicted by theoretical prediction shown in Fig. 3.1 (dashed line). There are two peaks in the stopband (TL>10 dB). The measured TL for the plate with perforations also shows that the trough point in the frequency range 350 Hz to 400 Hz is raised, and the third peak is shifted to a higher frequency so that the band limit f_2^* is extended from 500 Hz to 590 Hz. Such an improvement is roughly in agreement with the theoretical predictions.

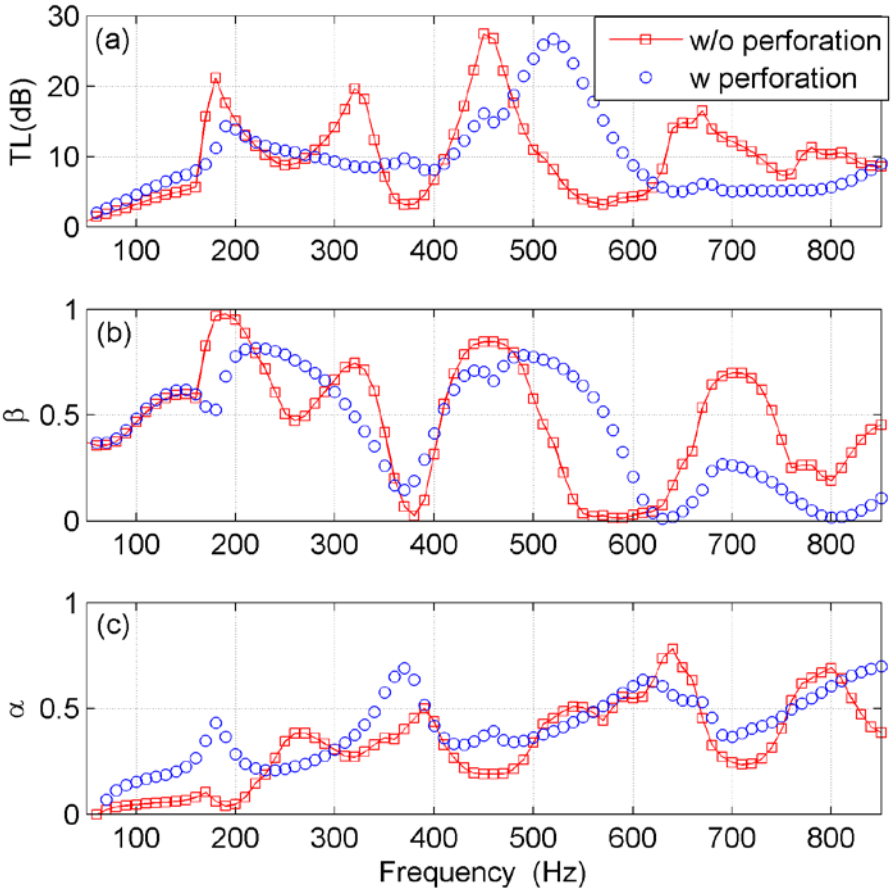

Fig.4.9 Experimental results for validating the theoretical predictions

Although the experimental results show that the perforations can truly enhance the trough point and widen the stopband, there are some practical limitations. For example, the installation of the plate to the cavity is one issue. Fig. 4.10 shows a

typical example of a failed installation. The TL spectrum in Fig. 4.10(a) is very low with absorption shown in Fig. 4.10(c) being relatively high within the overall frequency range, which may be due to sound leakage to the cavity. The air flow through the gap balances the pressure. As a result, the driving force is reduced, and the vibration of the plate is correspondingly reduced, and thus the reflection coefficient is below 0.5, seen in Fig. 4.10(b).

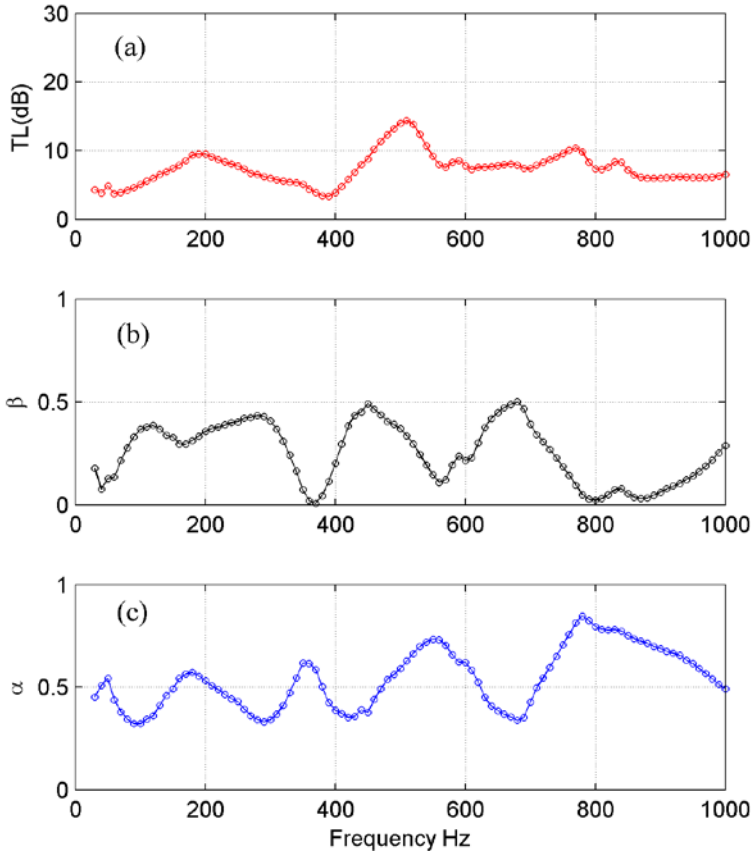

Fig.4.10 Experimental results from poor installation.

(a) Transmission loss; (b) Reflection coefficient; (c) Absorption coefficient.

There are also some limitations on the plate material. As a kind of porous material, as seen in Fig. 4.11(a), the manufacturing process of drilling micro-perforated holes by laser machine turned out to be very tedious and it was difficult to control the exact size of each hole as well as its shape. A typical drilled micro-perforated hole is shown

in Fig. 4.11(b), illustrating the irregular shape of the hole. Close examination of the hole typology using a microscope revealed that the range of the drilled hole diameter varied from 0.2 mm to 0.9 mm when using laser drilling on this type of material, whilst the projected hole diameter was 0.4 mm. Therefore the intention here is not to validate the accuracy of the theoretical prediction. Instead we would rather focus on confirming the micro-perforation effect predicted in the above analyses.

(a)

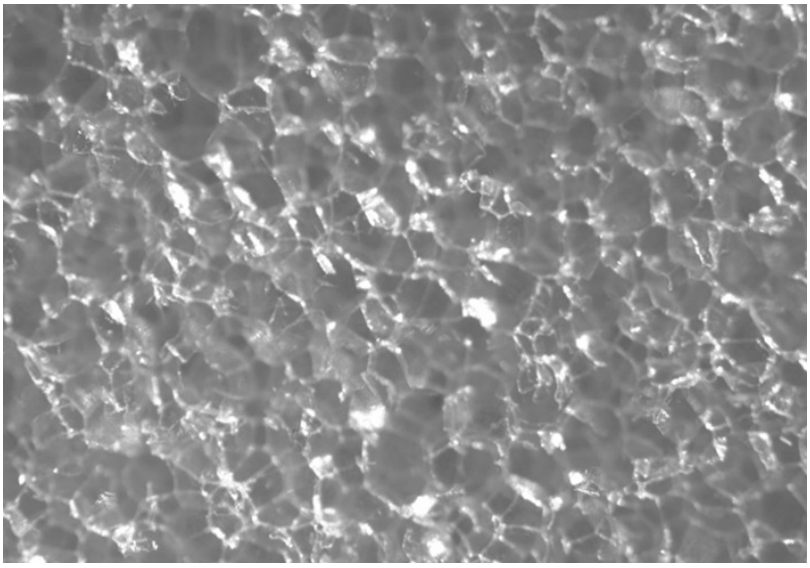

(b)

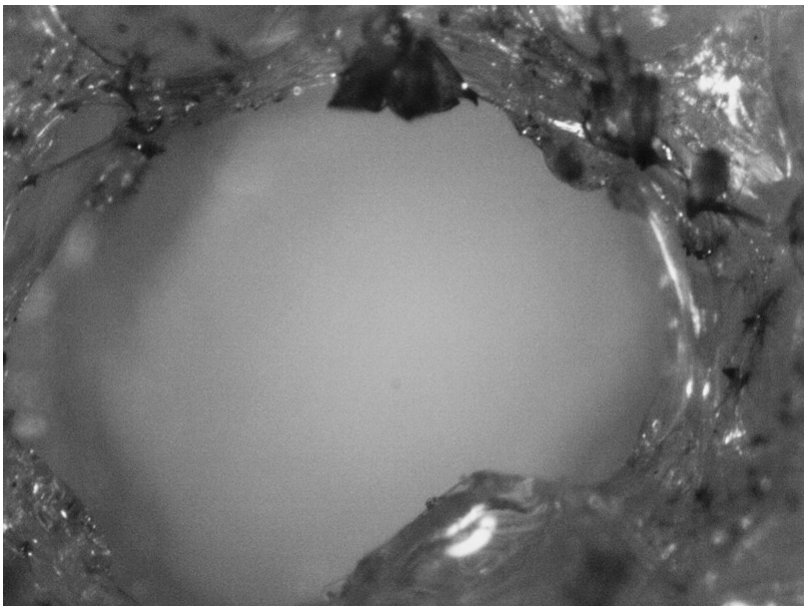

Fig.4.11 PMI plate and millimetre hole checked by microscope:

(a) the surface of the PMI plate, (b) actual shape of the hole

4.5 Summary

The experiment in this chapter has been carried out to validate the theoretical model in Chapters 2 and 3. From the theoretical analysis, by introducing micro-perforations to the plate silencer there are three significant changes, which are a smoothing of the TL peaks, lifting of the TL trough and expanding of the working range to higher frequencies.

The composite plate is fabricated by adhering carbon fibres to a PMI plate. Carbon fibre is used to reinforce the stiffness of the plate. Sub-millimetre holes are drilled by laser machine. The experimental results validate the three changes that micro-perforation has made to the system. However there are some limitations since installation is delicate, and poor installation may cause either sound leakage or friction. The PMI itself is also a porous material. These problems are excluded in the theoretical analysis.

CHAPTER 5

HYBRID PASSIVE AND ACTIVE NOISE CONTROL SYSTEM

5.1 Introduction

The performance of the plate silencer with micro-perforations has been investigated theoretically and experimentally in Chapters 2 to 4. The benefit of combining sound reflection and absorption mechanism is a more uniform TL spectrum with a wider stopband and a relaxation of the harsh requirement on the material property imposed by previous plate silencers. Reflection dominates most of the working range, while the absorption can compensate for the insufficiency of reflection in certain frequency ranges. The balance between reflection and absorption can be adjusted through a simple method of tuning perforation parameters, such as perforation ratio and diameter of the hole.

However, this noise control system is a purely passive system. In an attempt to achieve a performance with an even broader working bandwidth as well as relatively good behaviour at low frequencies, active control is a very typical and common method. In this chapter, active control is therefore introduced into the plate silencer with micro-perforations. As a result, a system by combining passive and active control

mechanisms is developed, that is so-called ‘hybrid’. The purpose is to explore the possibility of enhancing the TL performance of the current plate silencer with micro-perforations at even lower frequencies.

In this chapter, piezoelectric material is used as the actuator due to its compact and stable properties. An extra plate attached to the piezoelectric actuator is placed adjacent to the original plate. The purpose of using another plate is to avoid deteriorating the passive performance that the original single plate can achieve. Thus, there are two coupling plates in this system.

The modelling of the hybrid noise control system is described in Sec. 5.2. Due to its complexity, the modelling is divided into several steps: 1) Lagrange equation is used for establishing the model of the plate with piezoelectric material attached by taking the mass and the bending stiffness of the piezoelectric material into consideration. The driving force provided by the piezoelectric actuators can also be obtained; 2) the coupling model of two adjacent plates interaction in a duct is developed; 3) integration of the first step, second step and micro-perforation to model the hybrid system.

Two operation modes for the hybrid system are pre-defined. When the external voltage is zero, which means the driving force provided by the piezoelectric actuator is excluded, the system under this situation is defined as the passive mode. When the

external driving force is involved, the operation mode is regarded as the active mode of the hybrid system.

Before discussing the active control algorithm, the performance of the hybrid system in passive mode is studied from Sec. 5.3 to Sec. 5.6. In Sec. 5.3, validation is carried out with the theoretical results compared with FEM simulation; A new TL criterion is set for the one-side-branch plate silencer in Sec. 5.4. Parametric analysis is conducted in Sec.5.5, mainly focusing on the properties of the extra plate, such as its length, mass and bending stiffness. Optimization for the passive system then follows in Sec 5.6.

Sec. 5.7 introduces the active control algorithm and its realization. A simple control algorithm is developed by reinforcing the first modal vibration of the extra plate. The driving force is provided by the piezoelectric actuator. The amplitude and phase of the driving force as well as the location of the actuator are determined. An attempt is also made to decide the material properties of the piezoelectric actuator and the plate for the practical application.

5.2 Modelling of the hybrid noise control system

The configuration of the hybrid noise control system is shown in Fig.5.1. Two plates are designated, denoted as plate I and plate II: plate I is micro-perforated and plate II has a pair of piezoelectric actuators attached. Each plate is backed by a rigid cavity.

The two cavities are separated by a rigid wall. The centre of plate I is defined as the zero point for the *x*-axis. The distance between the centres of the two plates is denoted as *D*.

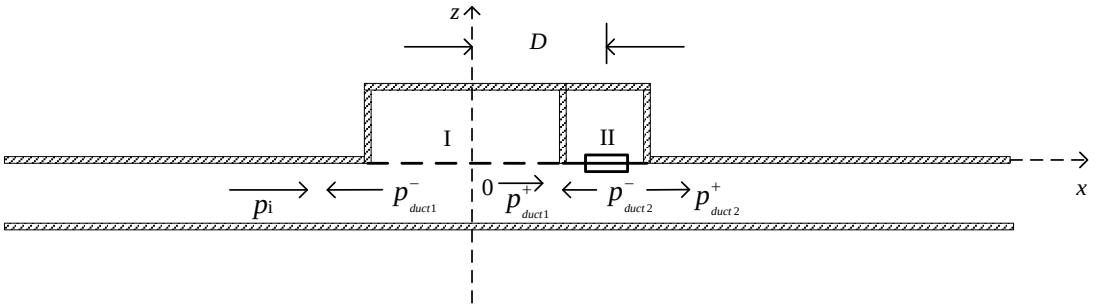

Fig.5.1 Configuration of the hybrid noise control system.

plate I is assigned to reflect the sound upstream as well as to absorb sound energy by micro-perforation, which has the same working mechanism with that of the plate silencer with perforations described in Chapter 2. Meanwhile, Plate II is forced into motion due to the operation of the actuators. The former plate is to controls sound from low to medium frequency while the latter plate suppresses sound within a very low frequency range which is beyond the working range of plate I.

When an incident sound wave passes over the plates in the duct, the plates are excited into vibration. They radiate sounds into the cavity, upstream and downstream of the duct. The radiation sounds in the two cavities are denoted as p_{cav1} and p_{cav2} respectively. And the radiation sound in the duct, according to their direction, are defined as p^-_{duct1}, p^+_{duct1}, p^-_{duct2} and p^+_{duct2}. The minus and plus signs represent the wave propagation upstream and downstream respectively. As a result, the fluid loading

attributed to the vibration of plate II in the upstream direction, p_{duct2}^{-} is imposed on plate I; while the fluid loading attributed to the vibration of plate I downstream, p_{duct1}^{+} is imposed on plate II. The coupling between plate I and plate II will be taken into consideration in the modelling.

It should be pointed out that in order to simplify the modelling, only half of the device is considered. This means that the duct has plates flush-mounted only in one side branch, while the opposite duct wall is rigid. The current study investigates the mutual interaction between the two adjacent plates with two different working mechanisms. If the opposite wall is also flush-mounted with two plates, there will be mutual interactions between the four plates. Such mutual couplings between four plates are complicated and are not considered here. Therefore two plates flush-mounted on one side of the wall are considered.

Three steps are carried out to finish the modelling. The first step is to establish the vibration model of a plate with attached piezoelectric actuator, the mass and bending stiffness of which cannot be ignored; the second step is to model the coupling of two adjacent plates flush-mounted in the one-side-branch of a duct, with micro-perforations and piezoelectric attachment excluded. And the third step is to combine the first step, second step and micro-perforation together to derive the complete hybrid system.

5.2.1 Plate vibration with piezoelectric actuators attached

A. Lagrange equation

Lagrange equation is a re-formulation of classical mechanics using the Hamilton principle. Lagrange equations apply to systems whether or not they conserve energy or momentum. The equation was introduced by Joseph Louis Lagrange in the 1780s. Lagrange equations are easy to use and well suited to mechanical systems (Moretti, 2002; Petyt, 2010).

In what follows, $a_1, \cdots, a_N$ are a set of N independent generalized coordinates for a system having N degrees of freedom. The N Lagrange equations which will give the N coupled differential equations of motion

$$\frac{d}{dt}\left(\frac{\partial \ell}{\partial \dot{a}_j}\right) - \frac{\partial \ell}{\partial a_j} = 0, \qquad j = 1, \cdots, N \tag{5.1}$$

where ℓ is the Lagrangian of the system expressed as $\ell = E_k - E_p + E_F$. E_k is the kinetic energy of the system, E_p the potential energy of the system and E_F the work done by external forces.

If the kinetic and potential energies as well as the work done by external force of the dynamic system can be expressed solely in terms of the generalized coordinates and their time derivatives, the motion of the system can be immediately expressed in terms of the generalized coordinates.

B. Dynamic equation for plate vibration with general boundary conditions

The plate in the current study is two-dimensional. The model calculated from the Lagrange equation will be compared with Euler-Bernoulli theory, which aims at 1) validating the accuracy of the model and 2) further developing the model of plates with piezoelectric materials attached.

In a general way, a two-dimensional plate with elastic boundaries is shown in Fig.5.2. The plate is elastically supported by translational and rotational springs at edges. By setting the appropriate constant *K* or *C* equal to either zero or infinity (Cheng, 1992), the plate edge is assumed to be supported by translational springs having a distributed stiffness *K* and by rotational springs having a distributed stiffness *C*. The four classical boundary conditions are defined as follows: free case (*K*=0,*C*=0;) guided case (*K*=0,*C*=∞); simply supported (*K*=∞, *C*=0); and clamped case (*K*=∞; *C*=∞).

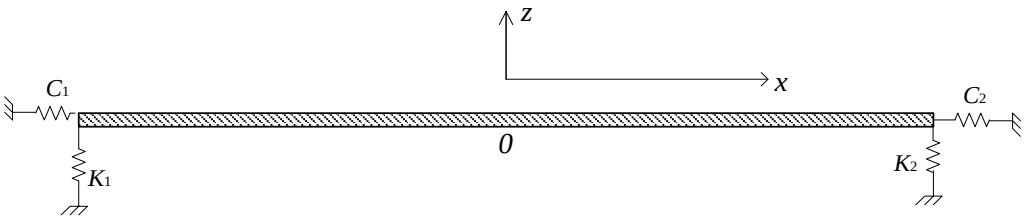

Fig.5.2 Two-dimensional plate with general boundary conditions.

To apply the Lagrange equation, the kinetic and potential energies should be calculated. Assuming the flexural displacement of the plate to be $\eta_b(x)$, the kinetic energy is described as

$$E_{k\_b} = \frac{1}{2}\int \rho_b v_b^2 dV_b \tag{5.2}$$

where ρ_b is the density of the plate, v_b the plate vibration velocity, and by assuming harmonic vibration, $v_b = i\omega\eta_b$. V_b is the volume of the plate.

Referring to the IEEE compact notation (*IEEE* Standard 176), the strain of the plate is

$$S_{1\_b}(x,z,t) = -z\frac{\partial^2\eta_b(x,t)}{\partial x^2}, \quad S_{2\_b} = S_{3\_b} = S_{4\_b} = S_{5\_b} = S_{6\_b} = 0 \tag{5.3}$$

From Hooke's law and using the IEEE compact notation, the stress can be written as

$$T_{1\_b} = Y_b S_{1\_b} \tag{5.4}$$

where T_{1_b} is the stress in the plate and Y_b is the Young's modulus of the plate.

The potential energy of the plate is defined as

$$E_{p\_b} = \frac{1}{2}\int T_{1\_b} S_{1\_b} dV_b \tag{5.5}$$

Also the potential energy of the springs used to simulate the boundary conditions is shown as

$$E_{p\_b}^{spring} = \frac{1}{2}K_1\eta_b(\frac{-L_b}{2})^2 + \frac{1}{2}K_2\eta_b(\frac{L_b}{2})^2 + \frac{1}{2}C_1[\frac{\partial\eta_b(\frac{-L_b}{2})}{\partial x}]^2 + \frac{1}{2}C_2[\frac{\partial\eta_b(\frac{L_b}{2})}{\partial x}]^2 \tag{5.6}$$

The potential and kinetic energies are both related to the displacement. However, the displacement is still unknown. Therefore the Rayleigh-Ritz method is adopted to approximate the plate displacement by a linear combination of simple functions. Polynomial expansion is widely adopted due to its generality.

The displacement can be expanded into a series of polynomials, which was widely used in previous studies (Proulx and Cheng, 2000; Charette *et al*., 1994).

$$\eta_b = \sum_{j=0}^{N-1} a_j \left(\frac{2x}{L_b}\right)^j \tag{5.7}$$

Eq. (5.2), Eq. (5.5) and Eq. (5.6) are converted into

$$E_{k\_b} = \frac{1}{2}\int \rho_b {v_b}^2 dV_b = \frac{\rho_b b_b h_b}{2}\int_{-L_b/2}^{L_b/2} \left(\frac{\partial \eta_b}{\partial t}\right)^2 dx = \sum_{j=0}^{N-1}\sum_{l=0}^{N-1} K'_{jl}\dot{a}_j\dot{a}_l \tag{5.8}$$

$$E_{p\_b} = \frac{1}{2}\int T_{1\_b} S_{1\_b} dV_b = \frac{1}{2}\int Y_b {S_{1\_b}}^2 dV_b = \sum_{j=2}^{N-1}\sum_{l=2}^{N-1} P'_{jl} a_j a_l \tag{5.9}$$

$$\begin{aligned} E_{p\_b}^{spring} &= \sum_{j=0}^{N-1}\sum_{l=0}^{N-1}\frac{1}{2}K_1 a_j a_l + \frac{2C_1}{L^2}\sum_{j=1}^{N-1}\sum_{l=1}^{N-1} jl a_j a_l + \\ &\quad \sum_{j=0}^{N-1}\sum_{l=0}^{N-1}\frac{1}{2}K_2(-1)^{j+l} a_j a_l + \frac{2C_2}{L^2}\sum_{j=1}^{N-1}\sum_{l=1}^{N-1} jl a_j a_l (-1)^{j+l-2} \\ &= \sum_{j=0}^{N-1}\sum_{l=0}^{N-1} P_{jl}^{spring} a_j a_l \end{aligned} \tag{5.10}$$

where $K'_{jl} = \frac{\rho_b b_b h_b L_b}{4}\frac{[1-(-1)^{j+l+1}]}{j+l+1}$, $P'_{jl} = \frac{b_b Y_b {h_b}^3}{3{L_b}^3} jl(j-1)(l-1)\frac{[1-(-1)^{j+l-3}]}{j+l-3}$, and

$P_{jl}^{spring} = [\frac{1}{2}K_1 + \frac{2C_1}{{L_b}^2} jl + \frac{1}{2}K_2(-1)^{j+l} + \frac{2C_2}{{L_b}^2} jl(-1)^{j+l-2}]$.

In the present study, the leading and trailing edge of the plate is assumed to be simply supported. Consequently, the displacement can also be expanded as a series of sine functions. For a simply supported plate, if polynomials are used for the Rayleigh-Ritz approximation, the potential energy of boundary conditions should be considered for extra calculation; while if the sine function is adopted for the expansion of displacement, there is no need for the extra calculation of the potential energy of the boundary conditions. Thus the displacement can be expressed as

$$\eta_b = \sum_{j=1}^{N} a_j \sin(j\pi\xi) \tag{5.11}$$

where $\xi = \frac{x}{L_b} + \frac{1}{2}$, $\xi \in [0 \quad 1]$.

The kinetic and potential energy for the plate are therefore written as

$$E_{k\_b} = \frac{\rho_b b_b h_b}{2} \int_{-L_b/2}^{L_b/2} (\frac{\partial \eta_b}{\partial t})^2 dx = \sum_{j=1}^{N} \sum_{l=1}^{N} K_{jl} \dot{a}_j \dot{a}_l \tag{5.12}$$

$$E_{p\_b} = \frac{1}{2} \int Y_b (-z \frac{\partial^2 \eta_b}{\partial x^2})^2 dV_b = \sum_{j=1}^{N} \sum_{l=1}^{N} P_{jl} j^2 l^2 a_j a_l \tag{5.13}$$

where $K_{jl} = \frac{L_b \rho_b b_b h_b}{4}$ and $P_{jl} = \frac{b_b Y_b \pi^4 h_b{}^3}{48 L_b^3}$ when $j = l$; while $K_{jl} = P_{jl} = 0$ when $j \neq l$

The Lagrange equation is applied to the above two expansions

$$\frac{d}{dt}(\frac{\partial \ell}{\partial \dot{a}_j}) - \frac{\partial \ell}{\partial a_j} = 0 \tag{5.14}$$

where $\ell = E_{k\_b} - E_{p\_b} + E_{p\_b}^{spring} + E_F$, and E_F is the work done by the external force which is zero in this case. In order to ascertain whether the sine function expansion can be adopted in the present study, comparison is performed among the sine function expansion, polynomial function expansion and Euler-Bernoulli theory (Wang, 1995). Table 5.1 gives the resonance frequencies calculated from the three methods for simulating a simply-supported plate with the plate properties given in Table 5.2.

Table 5.1 Natural frequencies calculated from the three methods (Hz)

Mode number / methods	1	2	3	4
Polynomial expansion	17.6435	70.5737	158.7906	282.2943
Sine expansion	17.6434	70.5736	158.7907	282.2946
Euler-Bernoulli theory	17.6434	70.5736	158.7907	282.2946

Table 5.2 Parameters of the plate

Density (kg/m^3)	2726
Young's modulus(Pa)	7×10^7
Length(m)	0.29
Thickness(m)	3.25×10^{-3}
Width(m)	2×10^{-3}

The resonance frequencies between the sine function expansion and Euler-Bernoulli theory are exactly the same, which is because when the plate is simply supported, the sine series are used to describe the vibration mode shape during the calculation using Euler-Bernoulli theory. The results from the polynomials expansion are generally the same with other two methods, with an error of 0.0001%.

C. Attachment of piezoelectric actuators on the plate

The modelling of a simply-supported plate using the Lagrange equation and the Rayleigh-Ritz approximation based on sine series was adopted in Part B above. This section further introduces the derivation of the dynamic equation of a simply supported plate with piezoelectric actuators attached. Two identical piezoelectric actuators are attached symmetrically onto the top and bottom of the plate, denoted as piezo1 and piezo2 respectively, as shown in Fig.5.3. An excitation is applied to the plate by the piezoelectric actuators later in the chapter, however, due to their masses and bending stiffnesses, their passive influences to the plate cannot be ignored. Therefore, before implementing the active control method, the passive configuration should be modelled primarily.

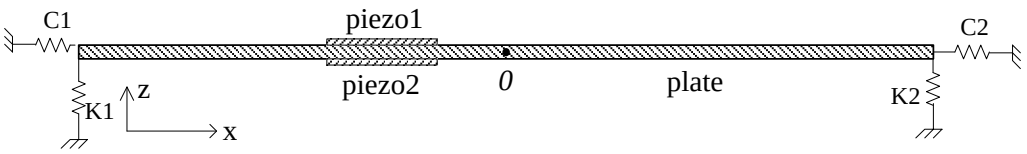

Fig.5.3 Configuration of a plate with two identical piezoelectric actuators attached symmetrically.

The Bernoulli hypothesis is assumed to describe the displacement of the plate. This hypothesis states that prior to or after deformation, any line perpendicular to the plate neutral axis remains perpendicular to the neutral axis, neglecting the shear and Possion effect. Fig.5.4 shows a segment of the plate-piezos patch before and after deformation; a random point P is specified to illustrate the flexural and extensional displacement.

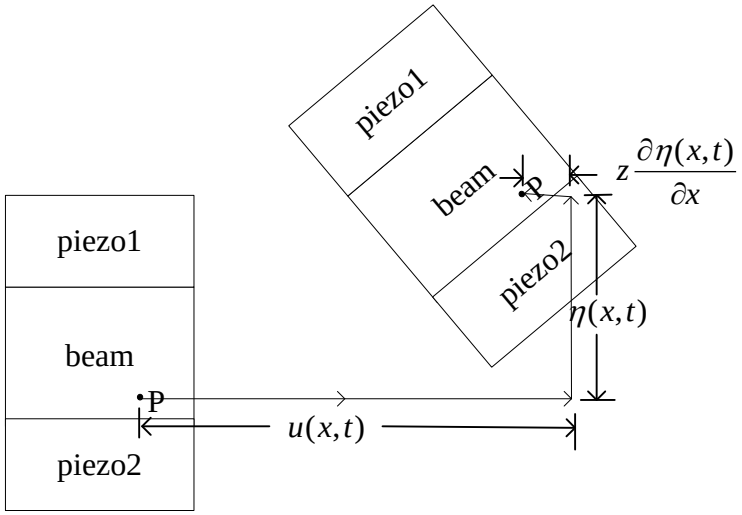

Fig.5.4 Displacement of a segment of the plate with piezoelectric actuators attached.

The displacement for the plate-piezos patch is written as

$$U(x,z,t) = u(x,t) - z\frac{\partial \eta(x,t)}{\partial x} \tag{5.15}$$

$$W(x,t) = \eta(x,t) \tag{5.16}$$

where U and W are the total displacement in the x and z directions respectively. $u(x,t)$ is the axial component due to the extensional motion, and $-z\frac{\partial \eta(x,t)}{\partial x}$ is due to the flexural motion.

The kinetic energies of piezo 1 and piezo 2 are

$$E_{k\_p_1} = \frac{\rho_{p_1} b_{p_1}}{2} \int_{h_b}^{h_b+h_{p_1}} \int_{x_{p_1}-L_b/2}^{x_{p_1}+L_b/2} [(\frac{\partial u\ (x,t)}{\partial t} - z\frac{\partial^2 w(x,t)}{\partial x \partial t})^2 + (\frac{\partial w(x,t)}{\partial t})^2] dx dz \qquad (5.17)$$

$$E_{k\_p_2} = \frac{\rho_{p_2} b_{p_2}}{2} \int_{h_b-h_{p_2}}^{h_b} \int_{x_{p_2}-L_b/2}^{x_{p_2}+L_b/2} [(\frac{\partial u(x,t)}{\partial t} - z\frac{\partial^2 w(x,t)}{\partial x \partial t})^2 + (\frac{\partial w(x,t)}{\partial t})^2] dx dz \qquad (5.18)$$

respectively.

The total enthalpy density of a piezoelectric patch can be written as (Plantier, 1995)

$$H = \frac{1}{2}[T_1 S_1 + e_{31}\frac{\Delta\varphi}{h} S_1 - \varepsilon_{33}(\frac{\Delta\varphi}{h})^2] \qquad (5.19)$$

where e_{31} is the stress/charge coefficient, ε_{33} the permittivity coefficient, and $\Delta\varphi$ is the voltage between the electrodes.

Therefore the potential energy of piezo 1 can be written as

$$E_{p\_p_1} = \int H_{p_1} dV_{p_1} = b_{p_1} \int_{h_b}^{h_b+h_{p_1}} \int_{x_{p_1}-L_b/2}^{x_{p_1}+L_b/2} \{\frac{Y_{11\_p_1}}{2}[(\frac{\partial u(x,t)}{\partial t} - z\frac{\partial^2 w(x,t)}{\partial x \partial t})^2 + (\frac{\partial w(x,t)}{\partial t})^2] + \frac{e_{31\_p_1}\Delta\varphi_{p_1}}{h_{p_1}}[\frac{\partial u(x,t)}{\partial x} - z\frac{\partial^2 w(x,t)}{\partial x^2}] - \frac{\varepsilon_{33}}{2}(\frac{\Delta\varphi_{p_1}}{h_{p_1}})^2\} dx dz \qquad (5.20)$$

while that of piezo 2 is

$$E_{p\_p_2} = \int H_{p_2} dV_{p_2} = b_{p_1} \int_{h_b-h_{p_2}}^{h_b} \int_{x_{p_2}-L_b/2}^{x_{p_2}+L_b/2} \{\frac{Y_{11\_p_2}}{2}[(\frac{\partial u(x,t)}{\partial t} - z\frac{\partial^2 w(x,t)}{\partial x \partial t})^2 + (\frac{\partial w(x,t)}{\partial t})^2] + \frac{e_{31\_p_2}\Delta\varphi_{p_2}}{h_{p_2}}[\frac{\partial u(x,t)}{\partial x} - z\frac{\partial^2 w(x,t)}{\partial x^2}] - \frac{\varepsilon_{33}}{2}(\frac{\Delta\varphi_{p_2}}{h_{p_2}})^2\} dx dz \qquad (5.21)$$

Thus by applying the Lagrange equation, resonance frequencies of this structure can be derived. Table 5.3 shows the calculation results of the resonant frequencies of the plate. Plate parameters are shown in Table 5.2, while Table 5.4 gives the parameters for the two piezoelectric actuators.

Table 5.3 Resonance frequencies before/after adding the two actuators to the plate (Hz)

Mode number / structure	1	2	3	4
plate	17.6435	70.5737	158.7906	282.2943
Plate with actuators attached	17.6417	70.5510	158.7084	282.1307

Table 5.4 Parameters for the piezoelectric actuators

Density (kg/m^3)	7600
Young's modulus(Pa)	6×10^{7}
Length(m)	0.02
Thickness(m)	0.18×10^{-3}
Width(m)	2×10^{-3}

Before and after attachment of the piezoelectric actuator, the variation of the resonance frequencies is within 0.05% which is very small. The influence of the mass of the piezoelectric actuator on the resonance frequencies is more significant than the stiffness effect of the piezoelectric actuator, which is purely decided by the material selection of the actuators.

5.2.2 Working mechanism of two plates in series as a side branch in a duct

In this section, the model of two adjacent plates flush-mounted on the wall of a duct in series is studied, as shown in Fig. 5.1.

The dynamic equations of plate I and plate II are shown as

$$m_{b1}\frac{\partial^2\eta_{b1}}{\partial t^2}+B_{b1}\frac{\partial^4\eta_{b1}}{\partial x^4}+p_i+p_{duct1}+p^-_{duct2}-p_{cav1}=0 \tag{5.22}$$

$$m_{b2}\frac{\partial^2\eta_{b2}}{\partial t^2}+B_{b2}\frac{\partial^4\eta_{b2}}{\partial x^4}+p_i+p^+_{duct1}+p_{duct2}-p_{cav2}=0 \tag{5.23}$$

respectively, where subscript 1 represents the parameters of plate I while subscript 2 represents those of plate II. m_{b1}, B_{b1}, and η_{b1} are the mass ratio, bending stiffness and displacement for plate I, while m_{b2}, B_{b2}, and η_{b2} are the mass ratio, bending stiffness and displacement for plate II. For plate I, its vibration is driven by the incident wave p_i and the self-radiated sound pressure, denoted as p_{duct1} and p_{cav1}. Besides, it is also affected by the radiated sound from plate II, p^-_{duct2}; while plate II is driven by the incident wave p_i , p_{duct2}, p_{cav2}, and radiated sound pressure p^+_{duct1} from plate I.

Simply-supported boundary conditions are used and modal expansion is conducted based on the Galerkin procedure. By considering the harmonic vibration by $v_{b1}=i\omega\eta_{b1}$ and $v_{b2}=i\omega\eta_{b2}$, the velocities are denoted as

$$v_{b1}=\sum_{j=1}^{N}V_{b1,j}\sin(j\pi\xi_1),\quad \xi_1=\frac{x}{L_{b1}}+\frac{1}{2} \tag{5.24}$$

$$v_{b2}=\sum_{j=1}^{N}V_{b2,j}\sin(j\pi\xi_2),\quad \xi_2=\frac{x-D}{L_{b2}}+\frac{1}{2} \tag{5.25}$$

where L_{b1} and L_{b2} are the length of plate I and plate II respectively. And D is the distance between the two centres of the plates, in this configuration, $D=\frac{L_{b1}+L_{b2}}{2}$.

By multiplying $2\sin(l\pi\xi_1)$ and $2\sin(l\pi\xi_2)$ into Eq. (5.24) and (5.25), and

integrating over the whole plate respectively

$$[m_{b1}i\omega+\frac{B_{b1}}{i\omega}(\frac{j\pi}{L_{b1}})^4]V_{b1,j}+2\int_0^1[p_i+p_{duct1}+p_{duct2}^-p_{cav1}]\sin(l\pi\xi_1)d\xi_1=0 \qquad (5.26)$$

$$[m_{b2}i\omega+\frac{B_{b2}}{i\omega}(\frac{j\pi}{L_{b2}})^4]V_{b2,j}+2\int_0^1[p_i+p_{duct1}^+p_{duct2}-p_{cav2}]\sin(l\pi\xi_2)d\xi_2=0 \qquad (5.27)$$

A. Radiation impedance

Following the same procedure in Chapter 2, the duct impedance and cavity impedance are derived as

$$Z_{duct1\_1,jl}=2\int_0^1 p_{duct1,j}\sin(l\pi\xi_1)d\xi_1 \qquad (5.28)$$

$$Z_{duct2\_2,jl}=2\int_0^1 p_{duct2,j}\sin(l\pi\xi_2)d\xi_2 \qquad (5.29)$$

$$Z_{duct2\_1,jl}=2\int_0^1 p_{duct2,j}\sin(l\pi\xi_1)d\xi_1 \qquad (5.30)$$

$$Z_{duct1\_2,jl}=2\int_0^1 p_{duct1,j}\sin(l\pi\xi_2)d\xi_2 \qquad (5.31)$$

The duct impedance has 2 numbers in the subscript: the first number represents the radiating source and the second represents on which plate the radiated pressure works. $Z_{duct2\_1,jl}$ and $Z_{duct1\_2,jl}$ show the coupling between the two plates. The cavity impedances are denoted as

$$Z_{cav1,jl}=2\int_0^1 p_{cav1,j}\sin(l\pi\xi_1)d\xi_1 \qquad (5.32)$$

$$Z_{cav2,jl}=2\int_0^1 p_{cav2,j}\sin(l\pi\xi_2)d\xi_2 \qquad (5.33)$$

For the duct impedance, p_{duct1} and p_{duct2} are given as

$$p_{duct1}(x,z)=\frac{i}{2}\sum_{r=0}^{\infty}\frac{(2-\delta_{0r})\cos(r\pi z)}{\sqrt{(r\pi/\omega)^2-1}}\times \int_{-\frac{L_{b1}}{2}}^{\frac{L_{b1}}{2}}\cos(r\pi z')V(x')[H(x-x')e^{-ik_r(x-x')}+H(x'-x)e^{ik_r(x-x')}]dx' \qquad (5.34)$$

$$p_{duct2}(x,z)=\frac{i}{2}\sum_{r=0}^{\infty}\frac{(2-\delta_{0r})\cos(r\pi z)}{\sqrt{(r\pi/\omega)^2-1}}\times \int_{\frac{L_{b1}}{2}}^{\frac{L_{b1}}{2}+L_{b2}}\cos(r\pi z')V(x')[H(x-x')e^{-ik_r(x-x')}+H(x'-x)e^{ik_r(x-x')}]dx' \tag{5.35}$$

respectively. Therefore, the impedances are given as

$$Z_{duct1\_1}=L_{b1}\sum_{r=0}^{\infty}(2-\delta_{0r})c_rQ_{1\_1} \tag{5.36}$$

where

$$Q_{1\_1}=\frac{jl\pi^2[e^{il\pi}-e^{-ik_rL_{b1}}][e^{il\pi}+e^{ij\pi}]}{[(k_rL_{b1})^2-(j\pi)^2][(k_rL_{b1})^2-(l\pi)^2]}-\frac{ik_rL_{b1}\delta_{jl}}{(k_rL_{b1})^2-(j\pi)^2} \tag{5.37}$$

In order to avoid the occurrence of singularities for plane wave r=0, as $j\pi=k_0L_{b1}$ or $l\pi=k_0L_{b1}$, there is arrangement of the mathematical formulations which are shown as follows

when $j\pi=k_0L_{b1}, l\pi\neq k_0L_{b1}$, $Q_{1\_1}=\dfrac{il\pi[1+(-1)^{j+l}]}{2[(k_0L_{b1})^2-(l\pi)^2]}$;

when $l\pi=k_rL_{b1}, j\pi\neq k_rL_{b1}, Q_{1\_1}=\dfrac{ij\pi[1+(-1)^{j+l}]}{2[(k_0L_{b1})^2-(j\pi)^2]}$;

and when $l\pi=k_0L_{b1}, j\pi=k_0L_{b1}, Q_{1\_1}=0.25-\dfrac{0.75*i}{k_0L_{b1}}$.

Similarly,

$$Z_{duct2\_2}=L_{b2}\sum_{r=0}^{\infty}(2-\delta_{0r})c_rQ_{2\_2} \tag{5.38}$$

with

$$Q_{2\_2}=\frac{jl\pi^2[e^{il\pi}-e^{-ik_rL_{b2}}][e^{il\pi}+e^{ij\pi}]}{[(k_rL_{b2})^2-(j\pi)^2][(k_rL_{b2})^2-(l\pi)^2]}-\frac{ik_rL_{b2}\delta_{jl}}{(k_rL_{b2})^2-(j\pi)^2} \tag{5.39}$$

The singularities are similar to Q_{1_1} with L_{b2} instead of L_{b1}.

The coupling impedance can be written as

$$Z_{duct2\_1} = L_{b2}\sum_{r=0}^{\infty}(2-\delta_{0r})c_r Q_{2\_1} \tag{5.40}$$

And

$$Z_{duct1\_2} = L_{b1}\sum_{r=0}^{\infty}(2-\delta_{0r})c_r Q_{1\_2} \tag{5.41}$$

With the singularities involved, the expression is written as

$$Q_{2\_1} = \begin{cases} \dfrac{\cos(l\pi)}{4}, & j\pi = k_0 L_{b2}, l\pi = k_0 L_{b1} \\ \dfrac{i}{2}\dfrac{l\pi e^{-ik_0 L_{b1}}[1-e^{ik_0 L_{b1}}\cos(l\pi)]}{(k_0 L_{b1})^2-(l\pi)^2}, & j\pi = k_0 L_{b2}, l\pi \neq k_0 L_{b1} \\ -\dfrac{i}{2}\dfrac{j\pi\cos(l\pi)[1-e^{-ik_0 L_{b2}}\cos(j\pi)]}{(k_0 L_{b2})^2-(j\pi)^2}, & j\pi \neq k_0 L_{b2}, l\pi = k_0 L_{b1} \end{cases} \tag{5.42}$$

And

$$Q_{1\_2} = \begin{cases} \dfrac{\cos(j\pi)}{4}, & j\pi = k_0 L_{b1}, l\pi = k_0 L_{b2} \\ -\dfrac{i\cos(j\pi)}{2}\dfrac{l\pi[1-e^{-ik_0 L_{b2}}\cos(l\pi)]}{(k_0 L_{b2})^2-(l\pi)^2}, & j\pi = k_0 L_{b1}, l\pi \neq k_0 L_{b2} \\ \dfrac{i}{2}\dfrac{j\pi[1-e^{ik_0 L_{b1}}\cos(j\pi)]e^{-ik_0 L_{b1}}}{(k_0 L_{b1})^2-(j\pi)^2}, & j\pi \neq k_0 L_{b1}, l\pi = k_0 L_{b2} \end{cases} \tag{5.43}$$

The cavity impedance can be calculated in the same manner of as in Chapter 2, which is not given here.

B. Transmitted coefficient

With the duct and cavity impedance calculated, the dynamic equations of Eq.(5.26) and Eq. (5.27) are written as

$$L_{1,j}V_{1,j} + [Z_{duct1\_1,jl} - Z_{cav1,jl}]V_{1,j} + Z_{duct2\_1,jl}V_{2,j} = -I_{1,j} \tag{5.44}$$

$$L_{2,j}V_{2,j}+[Z_{duct2\_2,jl}-Z_{cav2,jl}]V_{2,j}+Z_{duct1\_2,jl}V_{1,j}=-I_{2,j} \tag{5.45}$$

where

$L_{1,j}=m_{b1}i\omega+\frac{B_{b1}}{i\omega}(\frac{j\pi}{L_{b1}})^4$ and $L_{2,j}=m_{b2}i\omega+\frac{B_{b2}}{i\omega}(\frac{j\pi}{L_{b2}})^4$.

and

$$I_{1,j}=\frac{2}{L_{b1}}\int_{-L_{b1}/2}^{L_{b1}/2}e^{-ik_0x}\sin(j\pi\xi_1)dx=\frac{2e^{\frac{ik_0L_{b1}}{2}}j\pi}{(j\pi)^2-(k_0L_{b1})^2}[1-e^{-ik_0L_{b1}}\cos(j\pi)] \tag{5.46}$$

$$I_{2,j}=\frac{2}{L_{b2}}\int_{D-L_{b2}/2}^{D+L_{b2}/2}e^{-ik_0x}\sin(j\pi\xi_2)dx=e^{-ik_0D}\frac{2e^{\frac{ik_0L_{b2}}{2}}j\pi}{(j\pi)^2-(k_0L_{b2})^2}[1-e^{-ik_0L_{b2}}\cos(j\pi)] \tag{5.47}$$

Eq.(5.44) and (5.45) can be solved through matrix inversion

$$\begin{bmatrix}L_{1,j}+(Z_{duct1\_1,jl}-Z_{cav1,jl}) & Z_{duct2\_1,jl}\\ Z_{duct1\_2,jl} & L_{2,j}+(Z_{duct2\_2,jl}-Z_{cav2,jl})\end{bmatrix}\begin{bmatrix}V_{1,j}\\V_{2,j}\end{bmatrix}=-\begin{bmatrix}I_{1,j}\\I_{2,j}\end{bmatrix} \tag{5.48}$$

And the transmitted sound pressure is expressed as

$$\frac{p_t}{p_i}=1+\frac{p_{duct1}\big|_{r=0,x\to+\infty}}{p_i}+\frac{p_{duct2}\big|_{r=0,x\to+\infty}}{p_i}=1+\sum_{j=1}^{N}V_{1,j}T_{1,j}+\sum_{j=1}^{N}V_{2,j}T_{2,j} \tag{5.49}$$

$T_{1,j}$ and $T_{2,j}$ are the transmitted complex, which are defined as

$$T_{1,j}=\frac{L_{b1}}{2}\int_0^1 e^{ik_0L_{b1}(\xi-\frac{1}{2})}\sin(j\pi\xi_1)d\xi_1=\frac{\frac{L_{b1}}{2}e^{\frac{-ik_0L_{b1}}{2}}j\pi}{(j\pi)^2-(k_0L_{b1})^2}[1-e^{ik_0L_{b1}}\cos(j\pi)] \tag{5.50}$$

$$T_{2,j}=\frac{L_{b2}}{2}\int_0^1 e^{ik_0L_{b2}(\xi_2-\frac{1}{2}+\frac{D}{L_{b2}})}\sin(j\pi\xi_2)d\xi_2=e^{ik_0D}\frac{\frac{L_{b2}}{2}e^{\frac{-ik_0L_{b2}}{2}}j\pi}{(j\pi)^2-(k_0L_{b2})^2}[1-e^{ik_0L_{b2}}\cos(j\pi)] \tag{5.51}$$

5.2.3 Configuration of the hybrid noise control system

After establishing two important parts of the hybrid system in Sec 5.2.1 and Sec. 5.2.2, the dynamics of plate I with micro-perforations can be described as

$$m_{b1}\frac{\partial^2\eta_{b1}}{\partial t^2}+B_{b1}\frac{\partial^4\eta_{b1}}{\partial x^4}+p_i+p_{duct1}+p^-_{duct2}-p_{cav1}=0 \tag{5.52}$$

$$Z_{resist,0}(v_{01}-v_{p1})+Z_{react,0}v_{01}+p_i+p_{duct1}+p^-_{duct2}-p_{cav1}=0 \tag{5.53}$$

Following the standard Galerkin procedure as already shown in Sec5.5.2 by expanding the velocities as a series of *in vacuo* modes, Eq. (5.52) and Eq. (5.53) are expressed as

$$\{\frac{B_{b1}}{i\omega}(\frac{j\pi}{L_{b1}})^4+m_{b1}i\omega\}V_{p1,j}+(Z_{duct1\_1,jl}-Z_{cav1,jl})[(1-\sigma)V_{p1,j}+\sigma V_{01,j}]+Z_{duct2\_1,jl}V_{p2,j}=-I_{1,j} \tag{5.54}$$

$$Z_{resist,0}(V_{01,j}-V_{p1,j})+Z_{react,0}V_{01,j}+(Z_{duct1\_1,jl}-Z_{cav1,jl})[(1-\sigma)V_{p1,j}+\sigma V_{01,j}]+Z_{duct2\_1,jl}V_{p2,j}=-I_{1,j} \tag{5.55}$$

Meanwhile, by using the Lagrange equation, the dynamics of plate II is expressed as

$$\frac{d}{dt}(\frac{\partial\ell_{b2}}{\partial\dot{\eta}_{b2,j}})-\frac{\partial\ell_{b2}}{\partial\eta_{b2,j}}=0 \tag{5.56}$$

with $\eta_{b2}=\sum_{j=1}^{N}\eta_{b2,j}\sin(j\pi\xi_2)$ and $\eta_{b2,j}=\frac{V_{b2,j}}{i\omega}$.

And $\ell_{b2}=E_{k\_b2}+E_{p\_b2}+E_{k\_piezo1}+E_{k\_piezo2}+E_{p\_piezo1}+E_{p\_piezo2}+E_F$.

While $E_F=E_{p_i}+E_{p_{duct2}}+E_{p^+_{duct1}}+E_{p_{cav2}}$.

The calculation methods for the kinetic and potential energies of the plate and actuators are shown in Sec 5.2.1, and only the results are summarized as follows

$$E_{k\_b2}=\sum_{j=1}^{N}K_{b2,j}\dot{\eta}^2_{b2,j} \tag{5.57}$$

$$E_{k\_piezo1}=\sum_{j=1}^{N}\sum_{l=1}^{N}K_{piezo1,jl}\dot{\eta}_{b2,j}\dot{\eta}_{b2,l} \tag{5.58}$$

$$E_{k\_piezo2}=\sum_{j=1}^{N}\sum_{l=1}^{N}K_{piezo2,jl}\dot{\eta}_{b2,j}\dot{\eta}_{b2,l} \tag{5.59}$$

$$E_{p\_b2} = \sum_{j=1}^{N} P_{b2,j} \eta_{b2,j}^2 \tag{5.60}$$

$$E_{p\_piezo1} = \sum_{j=1}^{N} \sum_{l=1}^{N} P_{piezo11,jl} \eta_{b2,j} \eta_{b2,l} + \sum_{j=1}^{N} P_{piezo12,j} \eta_{b2,j} + P_{piezo13} \tag{5.61}$$

$$E_{p\_piezo2} = \sum_{j=1}^{N} \sum_{l=1}^{N} P_{piezo21,jl} \eta_{b2,j} \eta_{b2,l} + \sum_{j=1}^{N} P_{piezo22,j} \eta_{b2,j} + P_{piezo23} \tag{5.62}$$

$$E_{p_{cav2}} = \sum_{j=1}^{N} \sum_{l=1}^{N} F_{p_{cav2},jl} \eta_{b2,j} \eta_{b2,l} \tag{5.63}$$

$$E_{p_{duct2}} = \sum_{j=1}^{N} \sum_{l=1}^{N} F_{p_{duct2},jl} \eta_{b2,j} \eta_{b2,l} \tag{5.64}$$

$$E_{p^+_{duct1}} = \sum_{j=1}^{N} \sum_{l=1}^{N} F_{p^+_{duct1},jl} \overline{\eta}_{1,j} \eta_{b2,l} \tag{5.65}$$

$$E_{p_i} = \sum_{j=1}^{N} F_{pi,j} \eta_{b2,j} \tag{5.66}$$

Of which the constants $K_{b2,j}$, $K_{piezo1,jl}$, $K_{piezo2,jl}$, $P_{b2,j}$, $P_{piezo11,jl}$, $P_{piezo12,j}$, $P_{piezo13}$, $P_{piezo21,jl}$, $P_{piezo22,j}$, $P_{piezo23}$, $F_{p_{cav2},jl}$, $F_{p_{duct2},jl}$, $F_{p^+_{duct1},jl}$ and $F_{pi,j}$ are given in the Appendix.

Eq. (5.58) is re-arranged in the following matrix form as

$$\begin{aligned} &i\omega \frac{4}{L_{b2} b_{b2}} [\vec{K}_{b2} + \vec{K}_{piezo1} + \vec{K}_{piezo2}] \vec{V}_{b2} + \frac{1}{i\omega} \frac{4}{L_{b2} b_{b2}} [\vec{P}_b + \vec{P}_{piezo11} + \vec{P}_{piezo21}] \vec{V}_{b2} \\ &+ [\vec{Z}_{duct2\_2} - \vec{Z}_{cav2}] \vec{V}_{b2} + \vec{Z}_{duct1\_2} [(1-\sigma)\vec{V}_{p1} + \sigma \vec{V}_{01}] = \frac{-2}{L_{b2} b_{b2}} [\vec{F}_{p_i} + \vec{P}_{piezo12} + \vec{P}_{piezo22}] \end{aligned} \tag{5.67}$$

The term $\frac{4}{L_{b2} b_{b2}} [\vec{K}_{b2} + \vec{K}_{piezo1} + \vec{K}_{piezo2}]$, which acts as an overall mass ratio, is denoted as $m_2^{'}$, while the term $\frac{4}{L_{b2} b_{b2}} [\vec{P}_b + \vec{P}_{piezo11} + \vec{P}_{piezo21}]$ operates as an overall bending stiffness, denoted as $B_2^{'}$. Therefore, Eq. (5.67) is rewritten as

$$
\begin{aligned}
&i\omega m_2^{'}\vec{V}_{b2}+\frac{B_2^{'}}{i\omega}\vec{V}_{b2}+[\vec{Z}_{duct2\_2}-\vec{Z}_{cav2}]\vec{V}_{b2}\\
&+\vec{Z}_{duct1\_2}[(1-\sigma)\vec{V}_{p1}+\sigma\vec{V}_{01}]=\frac{-2}{L_{b2}b_{b2}}[\vec{F}_{p_i}+\vec{P}_{piezo12}+\vec{P}_{piezo22}]
\end{aligned}
\tag{5.68}
$$

Compared with the dynamic equation of plate II without attachment, shown in Eq. (5.45), the effects of the piezoelectric actuators on the plate are mainly threefold: 1). adding mass to the plate. Since $4\vec{K}_{b2}/L_{b2}b_{b2}=m_{b2}$, referring to Eq. (A.23) in the Appendix, the term $\frac{4}{L_{b2}b_{b2}}[\vec{K}_{piezo1}+\vec{K}_{piezo2}]$ is the mass added onto the plate provided by the actuators; 2). adding extra bending stiffness to the plate in terms of $\frac{4}{L_{b2}b_{b2}}[\vec{P}_{piezo11}+\vec{P}_{piezo21}]$; 3) providing an external excitation to the plate vibration due to the deformation of the piezoelectric actuators . The exciting force is expressed as follows

$$
\vec{F}_{piezo}=\frac{2}{L_{b2}b_{b2}}[\vec{P}_{piezo12}+\vec{P}_{piezo22}] \tag{5.69}
$$

The two identical actuators are designed to be driven out of phase. By referring to Eq.(A.28) in the Appendix, the modal driving force is given as

$$
F_{piezo,j}=\frac{4}{L_{b2}b_{b2}}P_{piezo12,j}=-\frac{4\Delta\varphi_{p_1}e_{31\_p_1}j\pi(h_{p_1}+h_{b2})}{L_{b2}}[\cos(j\pi\xi)]\Bigg|_{\frac{(x_{p1}-\frac{L_{p1}}{2})}{L_{b2}}+\frac{1}{2}}^{\frac{(x_{p1}+\frac{L_{p1}}{2})}{L_{b2}}+\frac{1}{2}} \tag{5.70}
$$

Combining Eq.(5.54), Eq.(5.55) and Eq. (5.68), the dynamic equations of the two plates can be solved through matrix inversion

$$\begin{bmatrix} V_{b1,j} \\ V_{01,j} \\ V_{b2,j} \end{bmatrix} =$$

$$-\begin{bmatrix} i\omega m_{b1} + \frac{B_{b1}}{i\omega}(\frac{j\pi}{L_{b1}})^4 + (Z_{duct1\_1,jl} - Z_{cav1,jl})(1-\sigma) & (Z_{duct1\_1,jl} - Z_{cav1,jl})\sigma & Z_{duct2\_1,jl} \\ (Z_{duct1\_1,jl} - Z_{cav1,jl})(1-\sigma) - Z_{resist,0} & Z_{resist,0} + Z_{react,0} + \sigma(Z_{duct1\_1,jl} - Z_{cav1,jl}) & Z_{duct2\_1,jl} \\ Z_{duct1\_2,jl}(1-\sigma) & Z_{duct1\_2,jl}\sigma & i\omega m_2^{'} + \frac{B_2^{'}}{i\omega} + (Z_{duct2\_2,jl} - Z_{cav2,jl}) \end{bmatrix}^{-1} \begin{bmatrix} I_{1,j} \\ I_{1,j} \\ \frac{2F_{pi,j}}{L_{b2}b_{b2}} + F_{piezo,j} \end{bmatrix}$$

(5.71)

5.3 Comparison between the analytical and FEM results

As mentioned, there are two operation modes for the current hybrid system, which are the passive mode and the active mode. The mutual relationship between the two plates has been investigated theoretically, without considering the external excitations by the actuators. This is the so-called passive mode. In this section, its performance in terms of transmission loss is validated by using the finite element method. Validation is first carried out without considering the perforations. The parameters are chosen with $B_{b1} = B_2^{'} = 0.129$, $m_{b1} = m_2^{'} = 1$ and $L_{b1} = L_{b2} = 5$. As shown in Fig.5.5, there is quite good agreement between the theoretical results and the FEM simulation result. The sharp peaks and dips indicate that there is very strong coupling between the two plates.

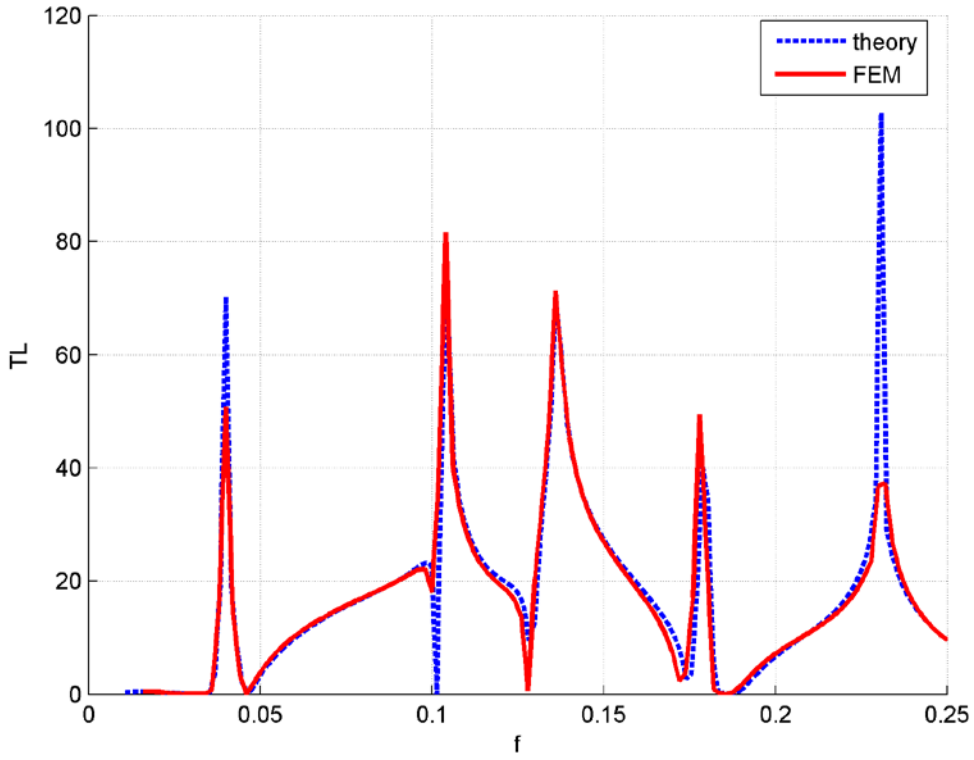

Fig.5.5 Comparison between the theoretical results and FEM simulation.

Fig. 5.6 also indicates the strong coupling between the two plates. It shows the comparison of two different configurations of the silencer. The dashed line represents the configuration with only one plate covered by one corresponding cavity, , and with B_{b1}=0.129, m_{b1}=1 and L_{b1}=5. The solid line represents the same configuration with that of Fig 5.5, that is, the silencer with two plates with $B_{b1}=B_2^{'}$=0.129, $m_{b1}=m_2^{'}$=1 and L_{b1}=L_{b2}=5. The TL pattern is totally different from the silencer with one plate as the sharp peaks and dips indicating two plates interaction.

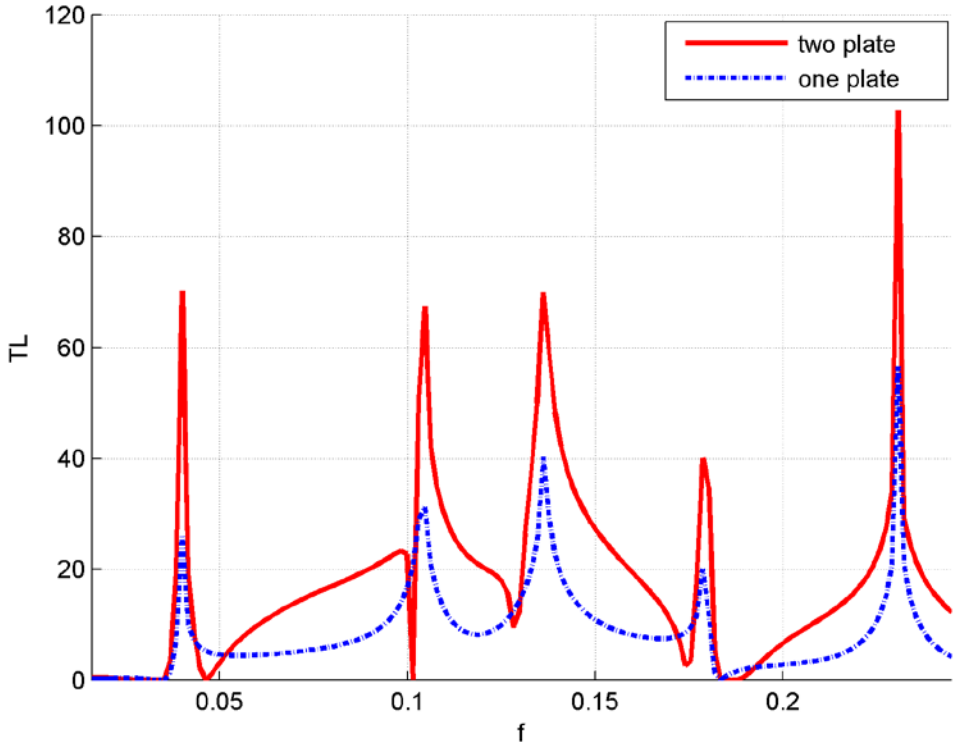

Fig.5.6 Comparison of TL spectra between the silencer with two plates (B_{b1}= $B_2^{'}$ =0.129, m_{b1}= $m_2^{'}$ =1 and L_{b1}=L_{b2}=5) and the silencer with only one plate (B_{b1}=0.129, m_{b1}=1 and L_{b1}=5).

For the silencer with two plates with B_{b1}= $B_2^{'}$ =0.129, m_{b1}= $m_2^{'}$ =1 and L_{b1}=L_{b2}=5, if micro-perforations are added to plate I with a perforation ratio σ=0.5%, diameter d=0.006, the TL spectrum shifts to a higher frequency within the range of 0.1<f <0.15, and meanwhile the TL peaks are smoothed out with trough lifted, as shown in Figure 5.7. The function of micro-perforation is exactly the same with that in Chapters 2 and 3.

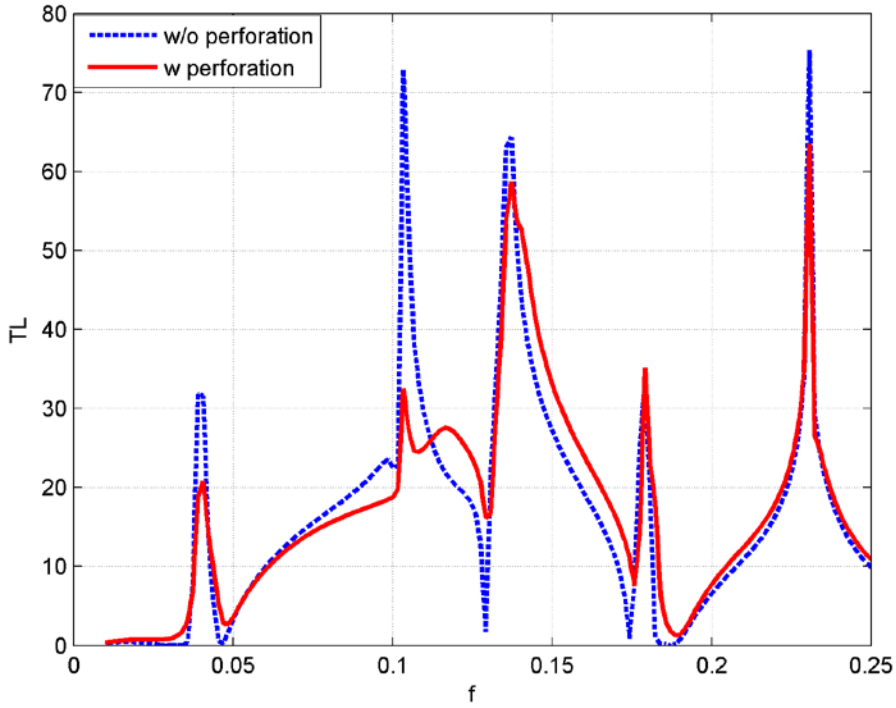

Fig.5.7 TL performance of the hybrid system in passive mode both without (dashed line) and with (solid line) micro-perforations in plate I.

5.4 TL criterion

In the current study, only half of the device is considered. The plate silencer in the previous study of Chapters 2 and 3 has two side branches, which means two identical plates are flush-mounted on the duct wall symmetrically along the duct central axis in the *x*-direction, while the silencer in this chapter only has one side branch with the rigid wall on the other side of the duct. This indicates that the former TL criterion of 10 dB which is used to assess the two-side-branch silencer may not be appropriate for the current device with one side branch. Fig. 5.8 shows the comparison of TL spectra. The dashed line represents the TL performance of the two-side-branch plate silencer which was studied in Chapter 2, and the solid line represents the TL spectrum of the

one-side-branch configuration with one single plate flush-mounted. The plates in the two configurations have the same properties with m=1, B=0.129 and L=5.

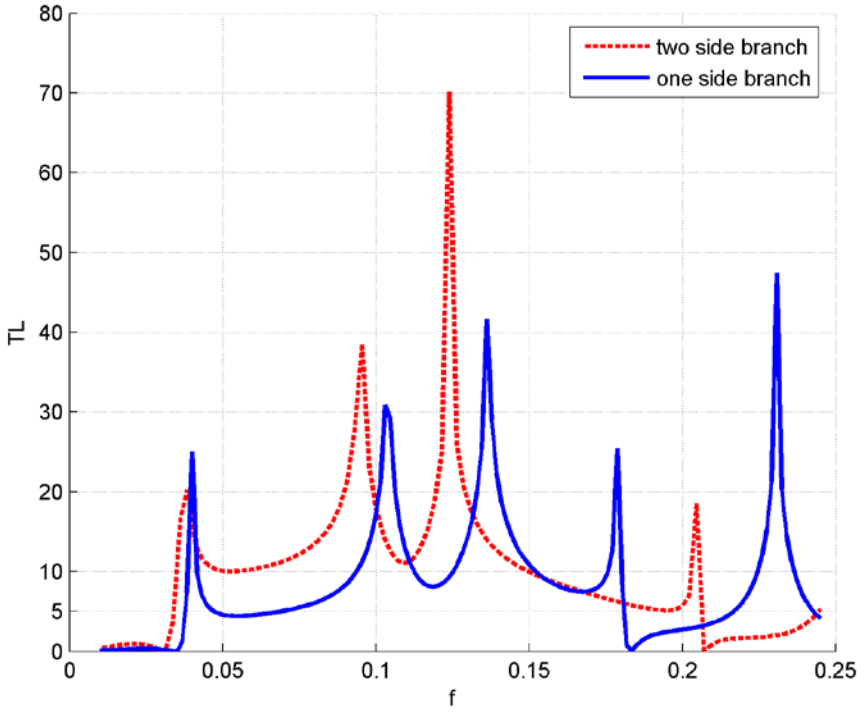

Fig.5.8 TL performance of one-side-branch silencer and two-side-branch silencer with the plate of m=1, B=0.129 and L=5.

It is observed that the performances are greatly different. TL of the two-side-branch system is above 10 dB within the range of f=0.035 to 0.15 with three peaks, while the one-side-branch system performs poorly if TL criterion TL_{cr} still equals 10 dB. However it has a continuous performance above 4 dB in the frequency range of f=0.036 to 0.18 with four peaks. Therefore the TL criteria should be reset.

Following the method provided by Huang (2005), for an expansion chamber, the two-side-branch system has a cross-sectional area ratio $a = \frac{S_2}{S_1}$, while S_2 is the

cross-sectional area of the expansion chamber and S_1 is the cross-sectional area of the main duct. TL can be described as (Du *et al*., 2000)

$$TL = 10\log_{10}[1+\frac{1}{4}(a-\frac{1}{a})^2 \sin^2 kL] \quad dB \tag{5.72}$$

If a=3, the maximum of TL is 4.4 dB. The two-side-branch plate silencer is designed to achieve 2 times performance of the expansion chamber with the same cross-sectional area, which is 8.8 dB. Thus an integer of 10 dB was set as the TL criterion in Chapters 2 and 3. However, for the one-side-branch system, a=2, therefore, the maximum of TL is reduced to 1.9 dB. Following the same procedure, twice 1.9 dB is chosen; 4 dB is thus set as the new TL criterion.

5.5 Parametric studies of the hybrid system in passive mode

With two plates mounted on one side of the duct wall, there is strong coupling between the plates, indicated by the impedance Z_{duct2_1} and Z_{duct1_2}, both of which vary with the length of the two plates. Thus, the relationship between the length of the two plates and the overall TL performance is first analyzed in Sec.5.5.1.

5.5.1 Length

Fig.5.9 shows the TL variation with the length of plate II, with L_{b1}=5 fixed and m_{b1}= $m_2^{'}$ =1, B_{b1}= $B_2^{'}$ =0.129. There are some observations. First of all, the location of the first TL peak is decided by the longer plate, as for $L_{b2} \leq 5$, the location of the first TL peak is basically unchanged. Once L_{b2} is larger than L_{b1}, the first peak shifts to a lower

frequency. This is because the plate with longer length has a lower first resonance frequency. Secondly, when L_{b2} is much smaller compared with L_{b1}, e.g. L_{b2}=1, plate II barely affects the performance of the plate I. Even if L_{b2}=2 or 3, the effect is relatively small in the low frequency of f<0.1.

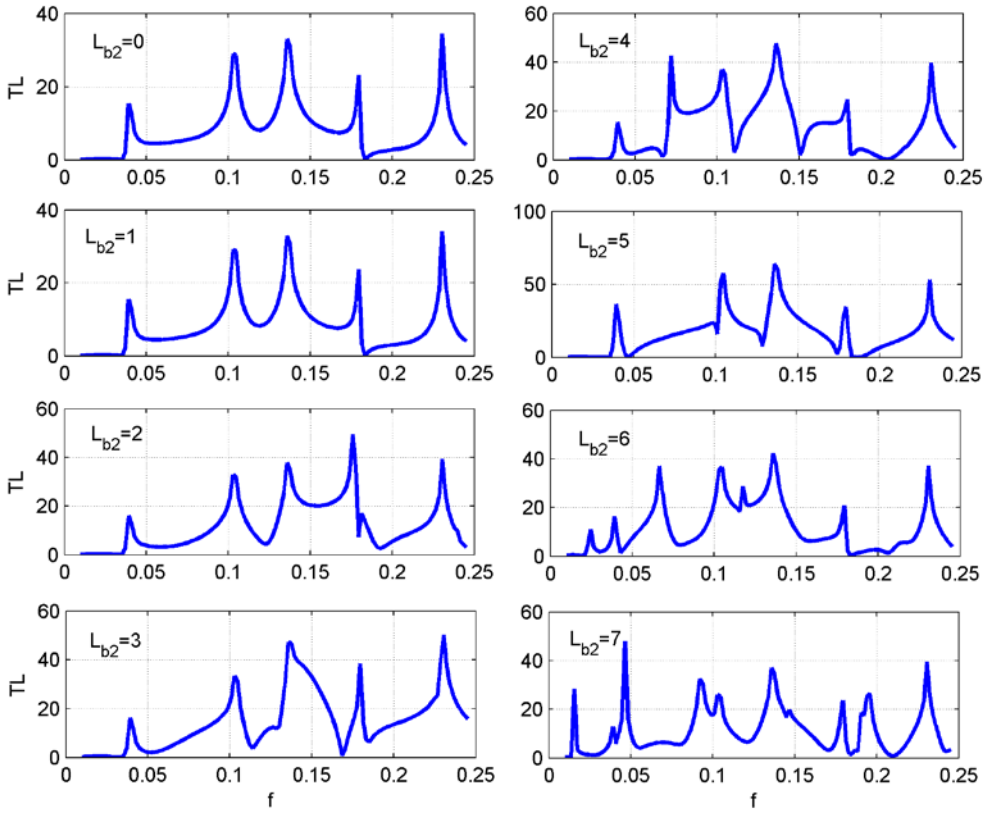

Fig.5.9 Variation of TL with the length of L_{b2}.

Fig.5.10 shows the modal amplitude of plate I and plate II with different L_{b2}=1,2,3. Other parameters are set as $m_{b1}=m_2^{'}=1$, $B_{b1}=B_2^{'}=0.129$ and L_{b1}=5. It validates that the interaction between the two plates can be ignored when there is a smaller L_{b2}, as $|V_{b2,j}|$ is far smaller than $|V_{b1,j}|$.

This observation is very important in this study. Since two plates are designed to

undertake different duties, if the coupling between them is small, it provides more flexible choices for the parameters of each individual plate. Based on the observation from Fig. 5.9 and Fig.5.10, if the length L_{b2} is small compared with L_{b1}, the longer plate drilled with sub-millimetre holes has a similar performance to that of the plate in Chapter 2, and simultaneously the shorter plate can have an actuator attached and be excited within a lower frequency range beyond the working range of plate I.

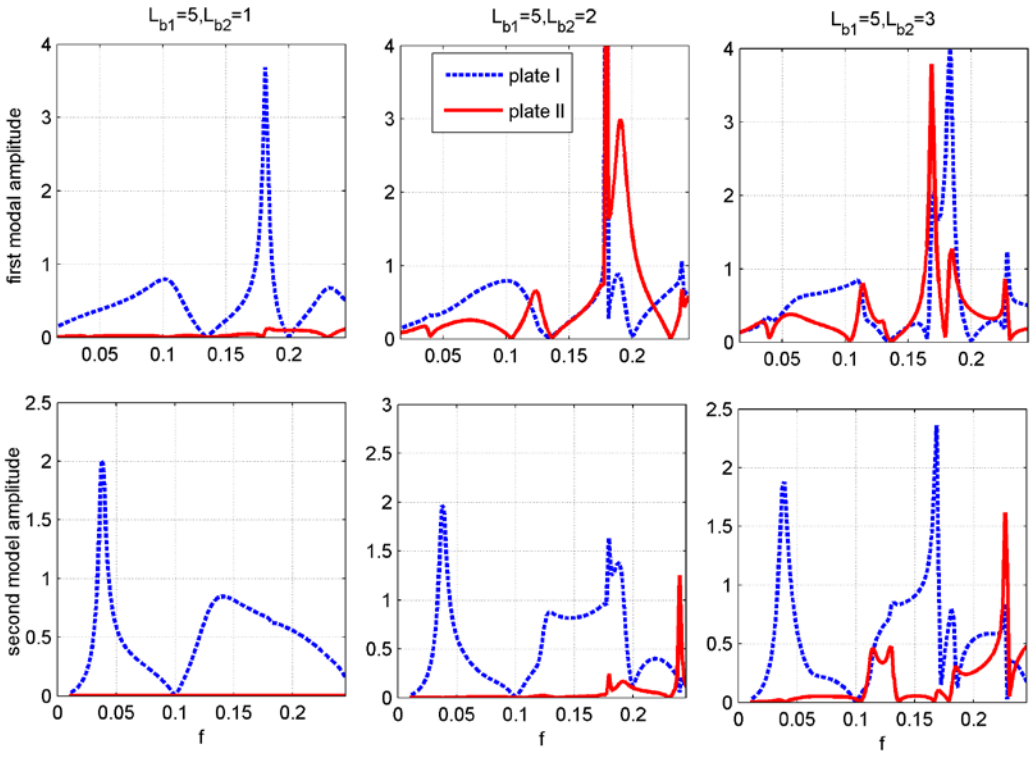

Fig.5.10 Model amplitudes of plate I and plate II, with different L_{b2}.

5.5.2 Mass

The mass study mainly focuses on the relationship between $m_2^{'}$ and the overall TL spectrum. It has significant meaning as the piezoelectric actuators influence the mass and bending stiffness of plate II. Before specifying the exact parameters of the

piezoelectric actuators and their influence on the plate, the general study of the mass and bending stiffness of plate II can be regarded as the guideline for choosing the piezoelectric material.

The parameters are set as m_{b1}=1, B_{b1}= $B_2^{'}$ =0.129 and L_{b1}=5. With different length of plate II, three values of $m_2^{'}$ are chosen, which are 1, 5 and 10. As shown in Fig.5.11 (a), when L_{b2} equals 1, which is a relatively small value, the effect of plate II on the system can be ignored, as plate I dominates the performance. With increasing L_{b2}, as shown in Fig. 5.11(b), the effect of $m_2^{'}$ becomes more obvious, as when $m_2^{'}$ =5, there is an extra peak between the original first and second TL peaks, and when $m_2^{'}$ =10, the extra peak shifts to lower frequency. This is because with a bigger $m_2^{'}$, the resonance frequency of plate II becomes smaller. The extra peak is due to the resonance of plate II. The same phenomenon can be seen in Fig.5.11 (c), which is more obvious as the effect of plate II on the overall system increases with L_{b2}.

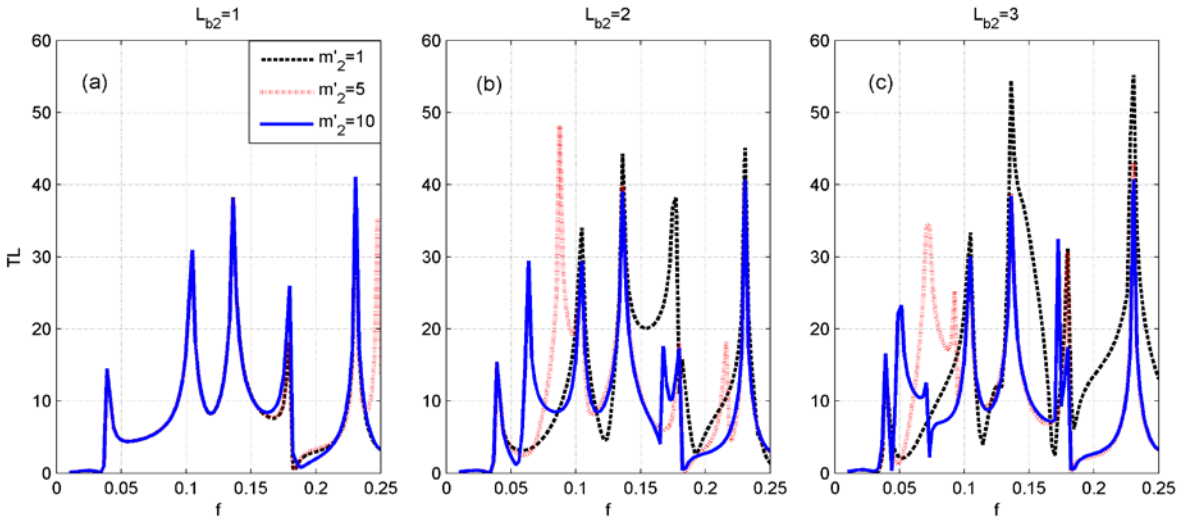

Fig.5.11 Variation of TL with $m_2^{'}$.

5.5.3 Bending stiffness

The silencer has the parameters with $m_{b1}=m_2^{'}=1$, $B_{b1}=0.129$ and $L_{b1}=5$. Three values of $B_2^{'}$ are chosen as 0.01, 0.1 and 1. Fig. 5.12 shows the TL variation with $B_2^{'}$. Fig.5.12 (a) shows the TL spectra when $L_{b2}=1$. It is observed that the TL performance is generally dominated by plate I. With L_{b2} increasing, shown in Fig.5.12 (b), an extra peak are observed when $B_2^{'}=0.01$. When $B_2^{'}$ is relatively high, i.e. $B_2^{'}=1$, the effect of plate II is not significant and ultimately TL is mainly attributed to the response of plate I only. With $L_{b2}=3$, the effect of plate II is more obvious.

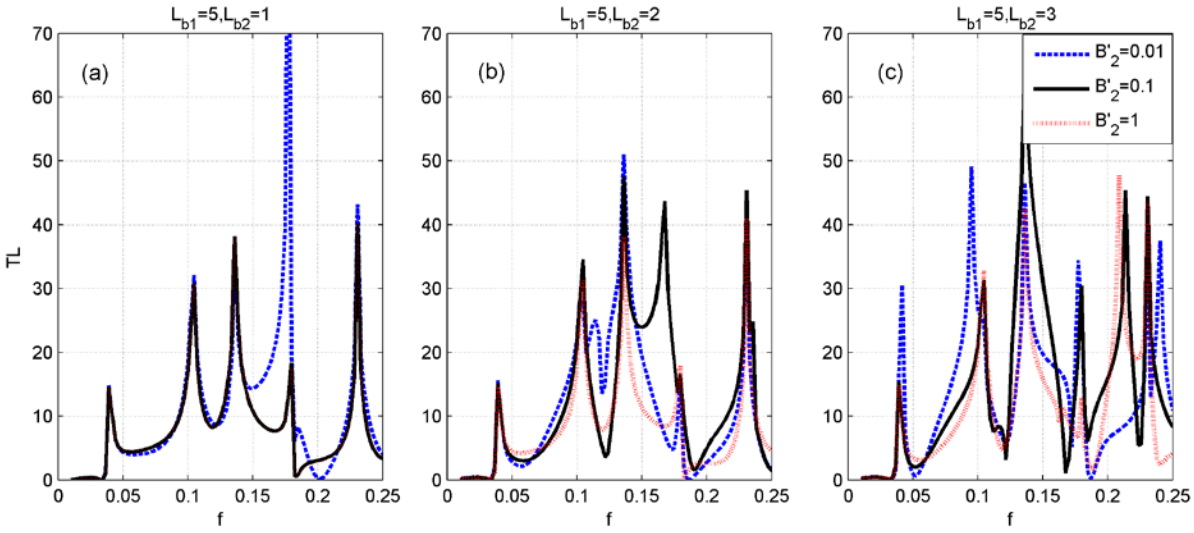

Fig.5.12 Variation of TL with different $B_2^{'}$.

5.6 Optimization for the hybrid silencer in passive mode

Optimization of the hybrid silencer in passive mode is described in this section. From Sec.5.5, there are two important observations: 1) When L_{b1} is fixed as 5, if L_{b2} is small, such as 1, the system performance is dominated by plate I, and the effect of plate II on

the system can be ignored, especially at a low frequency f < 0.1; 2). $m_2^{'}$ and $B_2^{'}$ will affect the system as it determines the resonance frequency of plate II. By tuning $m_2^{'}$ or $B_2^{'}$, the resonance of plate II may occur within the working range of the system originally governed by plate I, resulting in extra TL peaks. This phenomenon can be realized by increasing $m_2^{'}$ or decreasing $B_2^{'}$.

These observations give some directions for the system optimization of the structural properties. Firstly, if the coupling between the two plates is very small, it is more flexible to choose the parameters of the two plates. Secondly, the length of plate II is an important factor influencing the overall performance. If L_{b2} is smaller, the effect of plate II on the system becomes less significant. However, for considering active control on the system, plate II is forced to vibrate. If the length is too small, its effect on the system is small, and this consequently leaves a very high requirement for the external excitation. In order to achieve good performance with a small excitation force on the plate, the length L_{b2} should be as long as possible. So the optimization process is conducted in order to determine the appropriate length $L_{b2.}$

Optimization is carried out in two steps. The first step is to optimize the system only with plate I (plate II excluded). The optimization procedure is the same as that of the two-side-branch silencer in Chapter 2. And the second step is to search for the value of L_{b2} by studying its effect on the passive system with optimized plate I.

Fig. 5.13 shows the TL spectra for three different configurations by conducting the first step. The dashed line shows the optimal TL without perforations with m_{b1}=1,B_{b1}=0.129 and L_{b1}=5. There are four peaks from f=0.037 to 0.17. When B_{b1} is reduced, a trough appears in the medium frequency range (solid line). However, micro-perforations can compensate for the insufficient reflection (solid line with cross). The working principle is the same as that in the previous study on a two-side-branch silencer. The optimal set of parameters is therefore derived as m_{b1}=1, B_{b1}=0.105, d_{b1}=0.005, σ_{b1}=0.5% and τ_{b1}=0.04. The bending stiffness is also released by about 20%. There are four peaks within the bandwidth, instead of three. The working band extension is not as obvious as that of the two-side-branch silencer in Chapters 2 and 3; however, the trends are exactly the same.

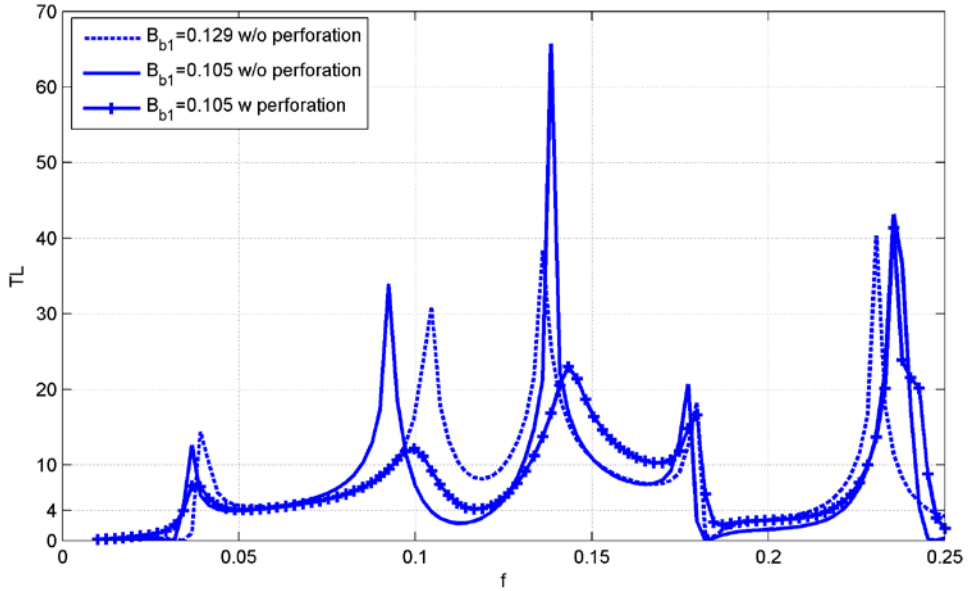

Fig.5.13 TL performance under three configurations for the system with only plate I. Dashed line: m_{b1}=1, B_{b1}=0.129 and L_{b1}=5, without perforations; Solid line: m_{b1}=1, B_{b1}=0.105 and L_{b1}=5, with perforations; Solid line with cross: m_{b1}=1, B_{b1}=0.105, L_{b1}=5,d_{b1}=0.005, σ_{b1}=0.5%,and $\tau_{b1}=0.04$.

Having completed the optimization of plate I, the effect by adding plate II on the system is analyzed. Fig.5.14 shows TL performance when taking plate II into consideration. By maintaining the optimal parameters derived from the previous step for plate I, the length of plate II L_{b2} varies from 1 to 2.5. The TL results for plate II with $m_2^{'}$=1 and $B_2^{'}$=0.129 is shown in Fig. 5.14 (a) and $m_2^{'}$=20, $B_2^{'}$=1 is shown in Fig. 5.14 (b), respectively. The purpose is to study the effect of L_{b2} on the system with different mass ratios and bending stiffnesses of plate II. This is a qualitative study as the exact mass and bending stiffness of plate II with attachment are unknown as yet.

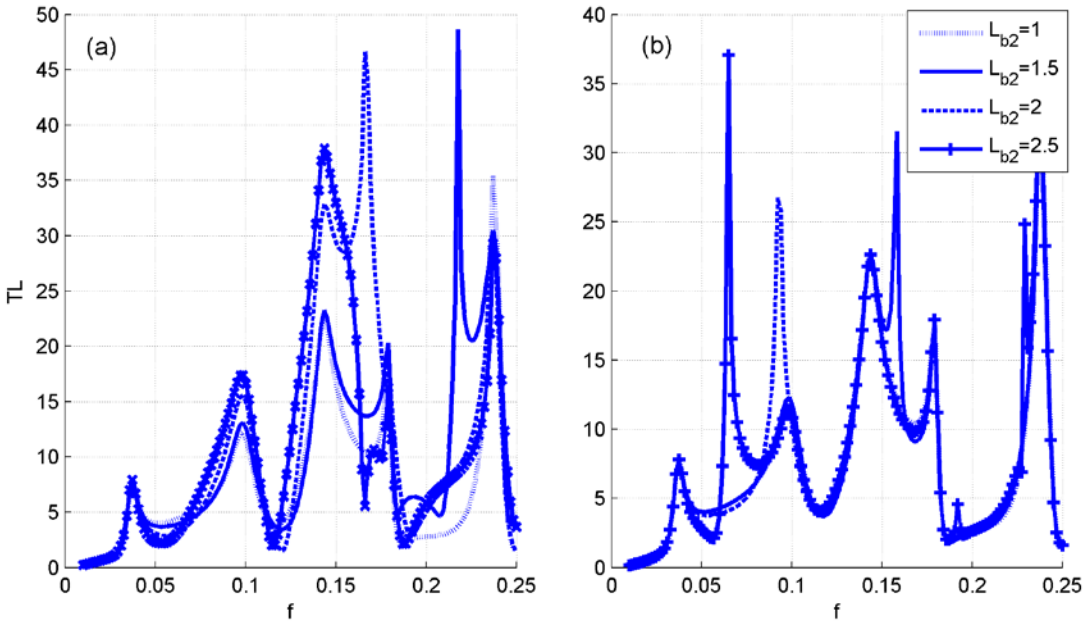

Fig.5.14 Variation of TL with different L_{b2} under two different sets of plate II

(a) $m_2^{'}$=1 and $B_2^{'}$=0.129; (b) $m_2^{'}$=20 and $B_2^{'}$=1.

As shown in Fig.5.14 (a), TL in the region between the first and second peak as well as that between the second and third peak deteriorates with an increase of L_{b2}. When L_{b2} is larger than 2, TL is below 4 dB within these two ranges. The same trends can be seen

from Fig. 5.14 (b); however it is not as obvious as that in Fig. 5.14 (a), which may because Plate II with a larger mass ratio and a higher bending stiffness is more difficult to be excited, thus its influence on plate I is less significant. Furthermore, it is noted that in Fig 5.14 (b), an extra peak is observed at $f = 0.07$ when $L_{b2} = 2.5$. This is due to the resonance of plate II which was illustrated before.

With TL_{cr}= 4dB, by referring to Fig.5.14, a maximum L_{b2}=1.6 is obtained, and further increase in L_{b2} deteriorates TL performance as the troughs become more serious. Another significant phenomenon to be noted is that, extra peaks caused by resonances of plate II may arise within the original working band dominated by plate I , which depends on the selection of $m_2^{'}$ and $B_2^{'}$. Therefore, by conducting the two steps, the optimized results are shown as m_{b1}=1, B_{b1}=0.105, and L_{b1}=5, with perforation ratio σ_{b1}=0.5%, diameter d_{b1}=0.005, and $\tau_{b1} = 0.04$ for plate I. Also before exact $m_2^{'}$ and $B_2^{'}$ can be selected (the material properties of plate II and actuators should be decided first), a maximal length of plate II is achieved as L_{b2}=1.6.

5.7 Performance of the hybrid system in active mode

The motivation for designing active control is to improve TL performance in very low frequency which is beyond the working range of the hybrid system in passive mode. As the passive system is already complex and bulky due to integrating two plates, two cavities, micro-perforations and actuators, it is necessary to conduct active control in a

simple way with a simple algorithm.

5.7.1 Control strategy

The advantage of this study is that the plates' vibration and the inter-couplings are well-known, and also the modal force provided by actuators is already calculated and rewritten here:

$$F_{piezo,j} = 8\Delta\varphi_{p_1} e_{31\_p_1} \cdot (h_{p_1} + h_{b2}) \cdot \frac{j\pi}{L_{b2}} \sin(\frac{j\pi x_{p_1}}{L_{b2}} + \frac{j\pi}{2}) \sin(\frac{j\pi L_{p_1}}{2L_{b2}}) \qquad (5.73)$$

If x_{p1}=0, which means the centres of the actuators are placed at x=0, the second mode of the force is zero. Under this condition, the first vibration mode of plate II is easy to be excited while there is no force working on the second vibration mode. Based on this information, the aim of the active control can be designed to excite the first mode of plate II. By exciting the first vibration mode of plate II in a well designed way, the target TL performance is attempted to be obtained.

Assuming the target frequency range for the active control is set as f < 0.035. Below f=0.035, the passive mechanism does not work effectively. It is also noted that a lower limit should be set, f=0.016 is chosen here, in a dimensional way, f*=54 Hz. Therefore, in the current work, f=0.016 to 0.035 is set to be the target frequency range of the active control.

Within this target frequency range, a target TL is set as

$$TL_{tar} = n \quad dB \qquad (5.74)$$

where *n* can be set as any value based on the system configuration. Different from the very common controlled source, the vibrations of plate I and plate II have been analyzed in detail. The amplitude and angle of every single mode is known, especially the dominant first two modes. The advantage is that once the target TL performance is set, the required plate vibration status can be derived. Thus no feedback is used here. Also, there is another reason to use a relatively simple control method: the system is complex by integrating two plates, two cavities and micro-perforations, so finding an easier active control algorithm gives the system more potential in practical application.

The target TL can be rewritten in the form of transmitted sound pressure

$$\left|\frac{p_t}{p_i}\right| = \left|1 + \sum_{j=1}^{N} \bar{V}_{b1,j} T_{1,j} + \sum_{j=1}^{N} V_{b2,j} T_{2,j}\right| = 10^{-\frac{n}{20}} \tag{5.75}$$

The dynamic equation of the hybrid system is referred to Eq.(5.71). The vibration modal amplitudes of the two plates are affected by the modal force of $F_{piezo,1}$. In the current study, the modal amplitudes of the two plates are written as the function of $F_{piezo,1}$, therefore Eq.(5.75) can be re-arranged as

$$\left|\frac{p_t}{p_i}\right| = \left|1 + \sum_{j=1}^{N} \bar{V}_{b1,j} T_{1,j} + \sum_{j=1}^{N} V_{b2,j} T_{2,j}\right| = \left|a + bi + (c + di) F_{piezo,1}\right| = 10^{-\frac{n}{20}} \tag{5.76}$$

Later sections show how to figure out the values of *a*, *b*, *c* and *d* by solving the dynamic equation of the system, where $a + bi$ is the complex constant and $(c + di)$ is the coefficient of $F_{piezo,1}$. As a result, the problem of achieving TL_{tar} is converted into searching for a proper external modal force $F_{piezo,1}$.

Once *a*, *b*, *c* and *d* are solved, there are numerous solutions of $F_{piezo,1}$ from Eq. (5.76). Assuming $F_{piezo,1} = x + yi$, Fig.5.15 gives the result of *x* and *y*. (*x*,*y*) is on a circle centred at (*p*,*q*), in which, $p = real(\frac{a+bi}{c+di})$, $q = imag(\frac{a+bi}{c+di})$, with the radius $\frac{10^{-\frac{n}{20}}}{|c+di|}$. For practical application, an additional restrict is adopted: the minimal $|F_{piezo,1}|$ is required, which means that the smallest $|F_{piezo,1}|$ drives plate II to vibrate in a way that achieves the target TL. In Fig. 5.15, The point nearest to the zero point is the final solution, which is denoted as (x_w,y_w). It represents the smallest force reaching the required transmitted sound pressure. From a practical view, the smallest force is easiest to realize, referring to the formula of $F_{piezo,1}$ of Eq. (5.73), once the geometry of plate I and actuators are determined, there is a linear relationship between the input voltage and the modal force.

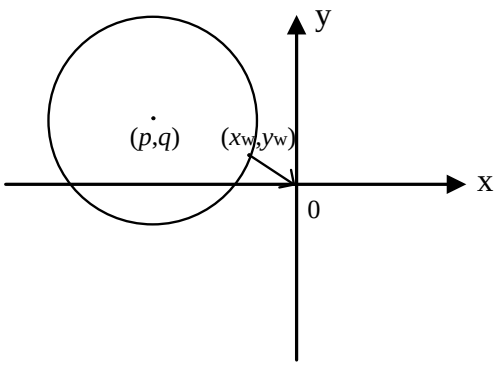

Fig.5.15 Solution of (*x*,*y*) and (x_w,y_w).

5.7.2 Model Truncation

The number of plate vibration modes is set to be 25 for the previous calculation. Further increase makes no significant improvement. However, based on the study, the first and second modes of the two plates play dominant roles. For the hybrid system in passive

mode, as shown in Fig.5.16, taking m_{b1}=1, B_{b1}=0.105, L_{b1}=5, d_{b1}=0.005, σ_{b1}=0.5% and τ_{b1}=0.04 for plate I, and $m_2^{'}$=1, $B_2^{'}$=0.129 and L_{b2}=1.6 for plate II. By setting the performance with N=25 as the reference (dashed line), when N equals 4, the difference from the reference is generally acceptable, as within the working range, the curves are superpositioned for the most part, except a little deviation at the second and third peaks. Further reducing N to 2, shown in solid line, the curve cannot present the real TL. However, when f < 0.05, it is coincident with the reference curve. This implies that within this range, only two modes involved can simulate the system behavior accurately enough. It has significant meaning as the complex system of plate vibration and couplings can be modelled with only two vibration modes of the two plates in the frequency range for active control.

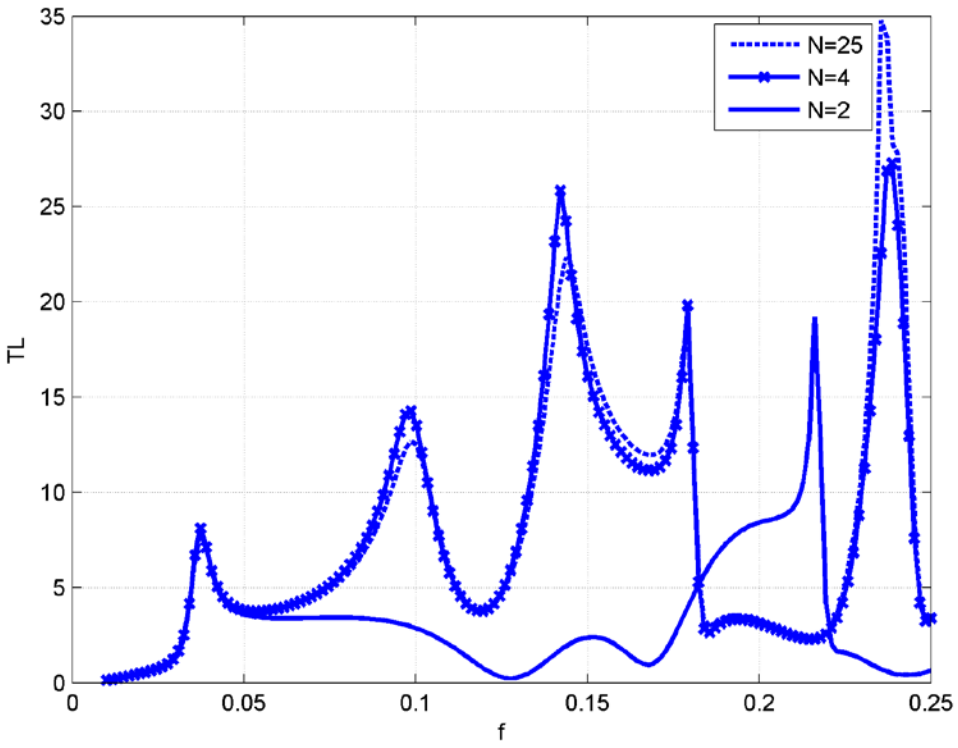

Fig.5.16 TL spectrum with different numbers of vibration modes involved.

Dashed line: N=25; Solid line with cross: N=4; Solid line: N=2.

The transmitted pressure p_t used to be the summation of $V_{1,j}T_{1,j}$ and $V_{2,j}T_{2,j}$ for j=1,2,…,25. Under this simplification, p_t is expressed as:

$$\frac{p_t}{p_i} = 1 + \bar{V}_{b1,1}T_{1,1} + \bar{V}_{b1,2}T_{1,2} + V_{b2,1}T_{2,1} + V_{b2,2}T_{2,2} \tag{5.77}$$

And in turns, Eq.(5.76) is simplified as

$$|1 + \bar{V}_{b1,1}T_{1,1} + \bar{V}_{b1,2}T_{1,2} + V_{b2,1}T_{2,1} + V_{b2,2}T_{2,2}| = |a + bi + (c + di)F_{piezo,1}| = 10^{-\frac{n}{20}} \tag{5.78}$$

5.7.3 Evaluation of the coupling between the first two vibration modes

With N=2, Eq. (5.71) can be truncated into six equations with nine unknowns, as shown in Eq. (5.79), which are $V_{p1,1}, V_{p1,2}, V_{01,1}, V_{01,2}, V_{p2,1}, V_{p2,2}, F_{piezo,1}$, $m_2^{'}$ and $B_2^{'}$, in which $m_2^{'}$ and $B_2^{'}$ can be determined if the size and material of plate II and actuators are selected. At this stage $m_2^{'}$ and $B_2^{'}$ are set with specific values in order to focus on the relationship between modal amplitude and the modal driving force $F_{piezo,1}$.

$$\begin{bmatrix} Q_{11} & Q_{12} & Q_{13} & Q_{14} & Q_{15} & Q_{16} \\ Q_{21} & Q_{22} & Q_{23} & Q_{24} & Q_{25} & Q_{26} \\ Q_{31} & Q_{32} & Q_{33} & Q_{34} & Q_{35} & Q_{36} \\ Q_{41} & Q_{42} & Q_{43} & Q_{44} & Q_{45} & Q_{46} \\ Q_{51} & Q_{52} & Q_{53} & Q_{54} & Q_{55} & Q_{56} \\ Q_{61} & Q_{62} & Q_{63} & Q_{64} & Q_{65} & Q_{66} \end{bmatrix} \begin{bmatrix} V_{p1,1} \\ V_{p1,2} \\ V_{01,1} \\ V_{01,2} \\ V_{p2,1} \\ V_{p2,2} \end{bmatrix} = - \begin{bmatrix} I_{1,1} \\ I_{1,2} \\ I_{1,1} \\ I_{1,2} \\ I_{2,1} + F_{piezo,1} \\ I_{2,2} \end{bmatrix} \tag{5.79}$$

where

$$
\begin{aligned}
&Q_{11}=L_{1,1}+(Z_{duct1\_1,11}-Z_{cav1,11})(1-\sigma);\quad Q_{12}=(Z_{duct1\_1,12}-Z_{cav1,12})(1-\sigma);\\
&Q_{13}=(Z_{duct1\_1,11}-Z_{cav1,11})\sigma;\quad Q_{14}=(Z_{duct1\_1,12}-Z_{cav1,12})\sigma;\quad Q_{15}=Z_{duct2\_1,11};\\
&Q_{16}=Z_{duct2\_1,12};\quad Q_{21}=(Z_{duct1\_1,21}-Z_{cav1,21})(1-\sigma);\\
&Q_{22}=L_{1,2}+(Z_{duct1\_1,22}-Z_{cav1,22})(1-\sigma);\quad Q_{23}=(Z_{duct1\_1,21}-Z_{cav1,21})\sigma;\\
&Q_{24}=(Z_{duct1\_1,22}-Z_{cav1,22})\sigma;\quad Q_{25}=Z_{duct2\_1,21};\quad Q_{26}=Z_{duct2\_1,22};\\
&Q_{31}=(Z_{duct1\_1,11}-Z_{cav1,11})(1-\sigma)-Z_{resist,0};\quad Q_{32}=(Z_{duct1\_1,12}-Z_{cav1,12})(1-\sigma);\\
&Q_{33}=Z_{resist,0}+Z_{react,0}+\sigma(Z_{duct1\_1,11}-Z_{cav1,11});\quad Q_{34}=(Z_{duct1\_1,12}-Z_{cav1,12})\sigma;\\
&Q_{35}=Z_{duct2\_1,11};\quad Q_{36}=Z_{duct2\_1,12};Q_{41}=(Z_{duct1\_1,21}-Z_{cav1,21})(1-\sigma);\\
&Q_{42}=(Z_{duct1\_1,22}-Z_{cav1,22})(1-\sigma)-Z_{resist,0};\quad Q_{43}=(Z_{duct1\_1,21}-Z_{cav1,21})\sigma;\\
&Q_{44}=Z_{resist,0}+Z_{react,0}+\sigma(Z_{duct1\_1,22}-Z_{cav1,22});\quad Q_{45}=Z_{duct2\_1,21};\quad Q_{46}=Z_{duct2\_1,22};\\
&Q_{51}=Z_{duct1\_2,11}(1-\sigma);\quad Q_{52}=Z_{duct1\_2,12}(1-\sigma);\quad Q_{53}=Z_{duct1\_2,11}\sigma;\quad Q_{54}=Z_{duct1\_2,12}\sigma;\\
&Q_{55}=i\omega m_2^{'}+\frac{B_2^{'}}{i\omega}+(Z_{duct2\_2,11}-Z_{cav2,11});\quad Q_{56}=(Z_{duct2\_2,12}-Z_{cav2,12});\\
&Q_{61}=Z_{duct1\_2,21}(1-\sigma);\quad Q_{62}=Z_{duct1\_2,22}(1-\sigma);\quad Q_{63}=Z_{duct1\_2,21}\sigma;\quad Q_{64}=Z_{duct1\_2,22}\sigma;\\
&Q_{65}=(Z_{duct2\_2,21}-Z_{cav2,21});\quad Q_{66}=i\omega m_2^{'}+\frac{B_2^{'}}{i\omega}+(Z_{duct2\_2,22}-Z_{cav2,22});
\end{aligned}
\tag{5.80}
$$

If the first and second mode decouple, Eq. (5.79) can be truncated into two matrices for solving first and second modal vibration independently, shown as

$$
\begin{bmatrix} Q_{11} & Q_{13} & Q_{15} \\ Q_{31} & Q_{33} & Q_{35} \\ Q_{51} & Q_{53} & Q_{55} \end{bmatrix}
\begin{bmatrix} V_{p1,1} \\ V_{01,1} \\ V_{p2,1} \end{bmatrix}
=-\begin{bmatrix} I_{1,1} \\ I_{1,1} \\ I_{2,1}+F_{piezo,1} \end{bmatrix}
\tag{5.81}
$$

and

$$
\begin{bmatrix} Q_{22} & Q_{24} & Q_{26} \\ Q_{42} & Q_{44} & Q_{46} \\ Q_{62} & Q_{64} & Q_{66} \end{bmatrix}
\begin{bmatrix} V_{p1,2} \\ V_{01,2} \\ V_{p1,2} \end{bmatrix}
=-\begin{bmatrix} I_{1,2} \\ I_{1,2} \\ I_{2,2} \end{bmatrix}
\tag{5.82}
$$

The effect of ignoring the coupling between the first two modes is evaluated by calculating TL of the hybrid system in passive mode by taking $m_{b1}= m_2^{'} =1$, $B_{b1}= B_2^{'} =0.105$, $L_{b1}=5$, $L_{b2}=1.6$, $d_{b1}=0.005$, $\sigma_{b1}=0.5\%$ and $\tau_{b1}=0.04$. As shown in Fig.5.17, The dashed line shows the result from the accurate calculation by using 25 coupling modes. The dotted line is the result of involving only two modes with the coupling between the two modes, and the solid line shows the result calculated from

Eq.(5.81) and (5.82) by assuming that the first and second modes are decoupled. The result starts deviating from the accurate value from f = 0.06, and a negative value even appears which is incorrect. However, below f = 0.06, the decoupled model can approximate the system performance. Since the active control is targeted at an even lower frequency of f < 0.035, this approximation can be used for modelling the hybrid system in passive mode within this target range.

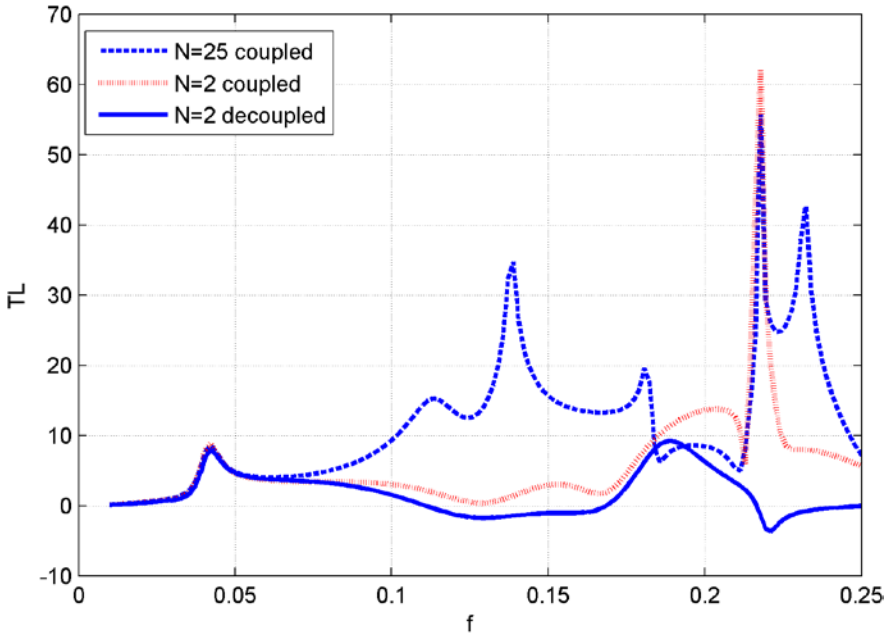

Fig.5.17 TL performance under three conditions. Dashed line: N=25 with all the modes coupled; Dotted line: N=2 with the two modes coupled; Solid line: N=2 with the two modes decoupled.

By solving Eq. (5.81) and (5.82), the modal amplitude can be expressed as functions of $F_{piezo,1}$, and also by combining with Eq. (5.78), the constant a, b, c and d can be obtained. Once TL_{tar} is set, $F_{piezo,1}$ can be solved correspondingly. This is a relative simply method to derive $F_{piezo,1}$. Therefore, based on this assumption, $F_{piezo,1}$ is calculated and shown by the dashed line in Fig.5.18. Fig 5.18 (1a) and Fig.5.18 (1b)

show the amplitude and phase of $F_{piezo,1}$ respectively with $m_2^{'}=1$ and $B_2^{'}=0.129$. Fig 5.18 (2a) and Fig 5.18 (2b) show the amplitude and phase of $F_{piezo,1}$ respectively with $m_2^{'}=100$ and $B_2^{'}=2$. Correspondingly, the solid line in Fig.5.18 represents the calculated results of $F_{piezo,1}$ from Eq. (5.71) by involving 25 coupling modes. As shown in Fig.5.18, the forces calculated from the decoupling assumption have the same trends as the accurate results; however, the amplitude is always a little larger than the accurate result. This may because by assuming the decoupling between the first and second modes, the influence on the second mode by external force is then ignored. The phases match well at frequencies of $f < 0.026$, but undergo some deviation at higher frequencies.

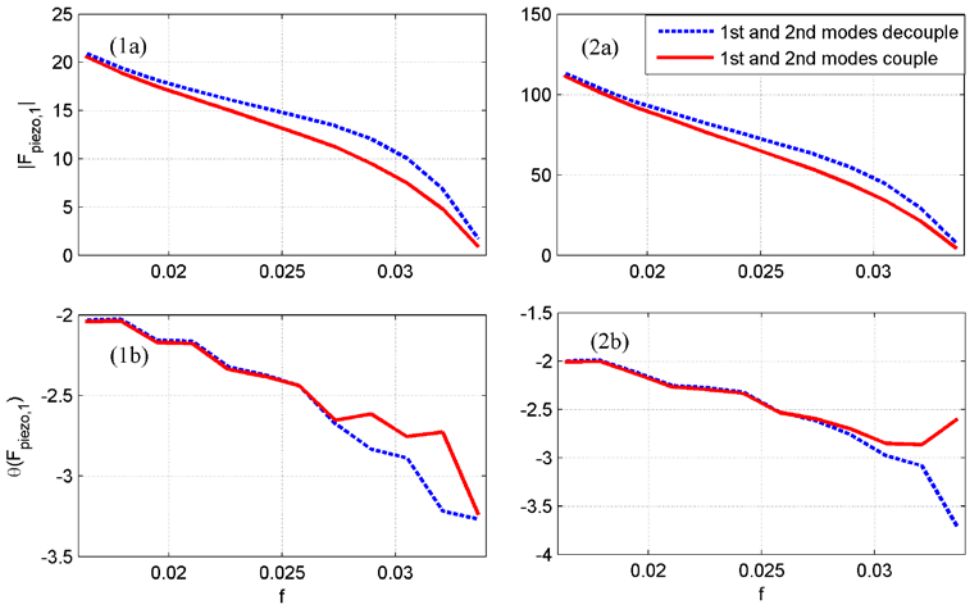

Fig.5.18 Amplitude and phase of $F_{piezo,1}$. Dashed line: results from the assumption of the first two modes decoupled . Solid line: results from the accurate model.

(1a) amplitude of $F_{piezo,1}$, and (1b) phase of $F_{piezo,1}$ with $m_2^{'}=1$ and $B_2^{'}=0.129$;

(2a) amplitude of $F_{piezo,1}$, and (2b) phase of $F_{piezo,1}$ with $m_2^{'}=100$ and $B_2^{'}=2$.

Fig.5.19 shows the TL performance of the hybrid system driven by $F_{piezo,1}$. The dashed line shows the TL results of the system driven by $F_{piezo,1}$ from the accurate model by calculating with the 25 coupling vibration modes. The solid line shows the TL result with $F_{piezo,1}$ derived from the assumption that the first two vibration modes are decoupled. By setting TL_{tar}=4 dB, the TL derived from the assumption is higher than 4 dB, since the force calculated from the decoupling assumption is larger, as shown in Fig 5.18.

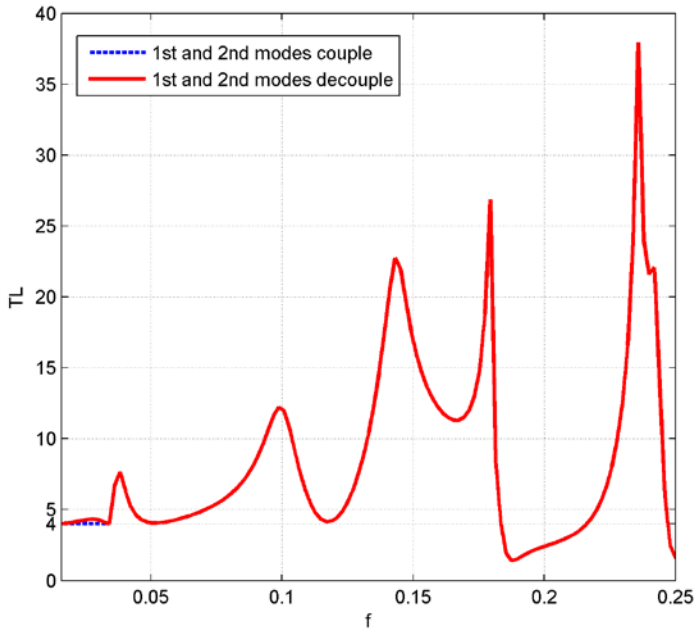

Fig.5.19 TL performance of the hybrid system driven by $F_{piezo,1}$.

Dashed line: $F_{piezo,1}$ is calculated from the accurate model by involving 25 coupling modes;

Solid line: $F_{piezo,1}$ is calculated from the model with first two decoupling modes.

Even though there are deviations of the TL spectra when ignoring the coupling between the first and second mode, the force calculated from the decoupling assumption can drive the system to satisfy the TL criterion of 4 dB. The decoupling

assumption can be used for qualitative analysis. Sec. 5.7.4 will use this assumption to tune the external modal force provided by actuators.

5.7.4 Structure impedance of plate II and the driving force

A target TL performance is proposed by set TL_{tar}. Meanwhile, the modal amplitude of two plates can be expressed as the functions of $F_{piezo,1}$. As derived from Sec. 5.7.2, at very low frequency, only the first two modes can describe the performance of the hybrid system. From Sec. 5.7.3, further ignoring the coupling between the first and second modes has little effect on the system in the target frequency range for active control. Through these two steps, the relationship between the modal force and the vibration modes is greatly simplified. Based on the two steps, the first modal vibration of plate II can be expressed as:

$$Z_{duct1\_2,11}[(1-\sigma)V_{p1,1}+\sigma V_{01,1}]+[i\omega m_2^{'}+\frac{B_2^{'}}{i\omega}+Z_{duct2\_2,11}-Z_{cav2,11}]V_{p2,1}=-[I_{2,1}+F_{piezo,1}] \quad (5.83)$$

A. Coupling force of plate I on plate II

Eq.(5.83) shows the governing equation of the first modal vibration of plate II. An approximation is further proposed as:

$$[i\omega m_2^{'}+\frac{B_2^{'}}{i\omega}+Z_{duct2\_2,11}-Z_{cav2,11}]V_{p2,1}\approx-[I_{2,1}+F_{piezo,1}] \quad (5.84)$$

where the radiation pressure of plate I on plate II, the term

$Z_{duct1\_2,11}[(1-\sigma)V_{p1,1}+\sigma V_{01,1}]$ is ignored. This approximation is acceptable by plotting the two terms of Eq.(5.83), which are $Z_{duct1\_2,11}[(1-\sigma)V_{p1,1}+\sigma V_{01,1}]$, denoted as term 1, and $[i\omega m_2^{'}+\frac{B_2^{'}}{i\omega}(\frac{\pi}{L_{b2}})^4+Z_{duct2\_2,11}-Z_{cav2,11}]V_{p2,1}$, denoted as term 2, with $F_{piezo,1}=0$. The parameters for the two plates are set as $m_{b1}=1$, $B_{b1}=0.105$, $L_{b1}=0.105$, d_{b1}=0.005 and $\sigma_{b1}=0.5\%$ for plate I, and $L_{b2}=1.6$ for plate II. $m_2^{'}=1$ and $B_2^{'}=0.1$ are adopted in Fig.5.20 (a), while $m_2^{'}=90$ and $B_2^{'}=0.5$ are used in Fig.5.20 (b). As shown by both two subfigures of Fig.5.20, the amplitude of term 1 is much smaller than that of term 2. The purpose of Fig.5.20 is to reveal that before inputting the external excitation $F_{piezo,1}$, the coupling between plate I and plate II is relatively small. If the first vibration mode of plate II is excited by the actuator, the amplitude of term 2 is greatly improved, and then the effect of plate I on plate II is even smaller.

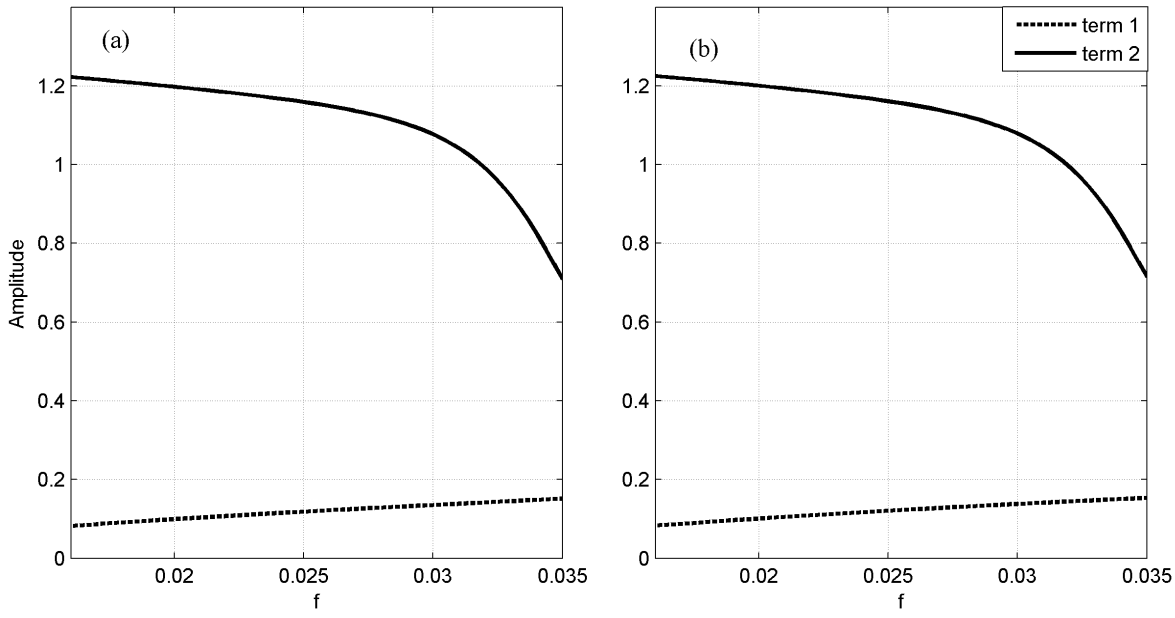

Fig.5.20 Amplitude of term 1 and term 2 of Eq.(5.83),

with (a) $m_2^{'}=1$ and $B_2^{'}=0.1$ (b) $m_2^{'}=90$ and $B_2^{'}=0.5$.

B. Modal force tuning with the structure impedance of plate II

The approximation of Eq.(5.84) gives a guideline for investigating the relationship between the external modal force $F_{piezo,1}$ and the structure impedance of plate II. The overall structure impedance $[i\omega m_2^{'} + \frac{B_2^{'}}{i\omega}]$ of plate II, denoted as $L_{2,1}^{'}$, only has an imaginary part. Fig.5.21 shows the real part and imaginary part of $(Z_{duct2\_2,11} - Z_{cav2,11})$, denoted as $Z_{dc2,1}$, which is independent from the material of the plate and actuators. Therefore, the total impedance $[L_{2,1}^{'} + Z_{dc2,1}]$ has a constant real part, while the imaginary part varies with $m_2^{'}$ and $B_2^{'}$.

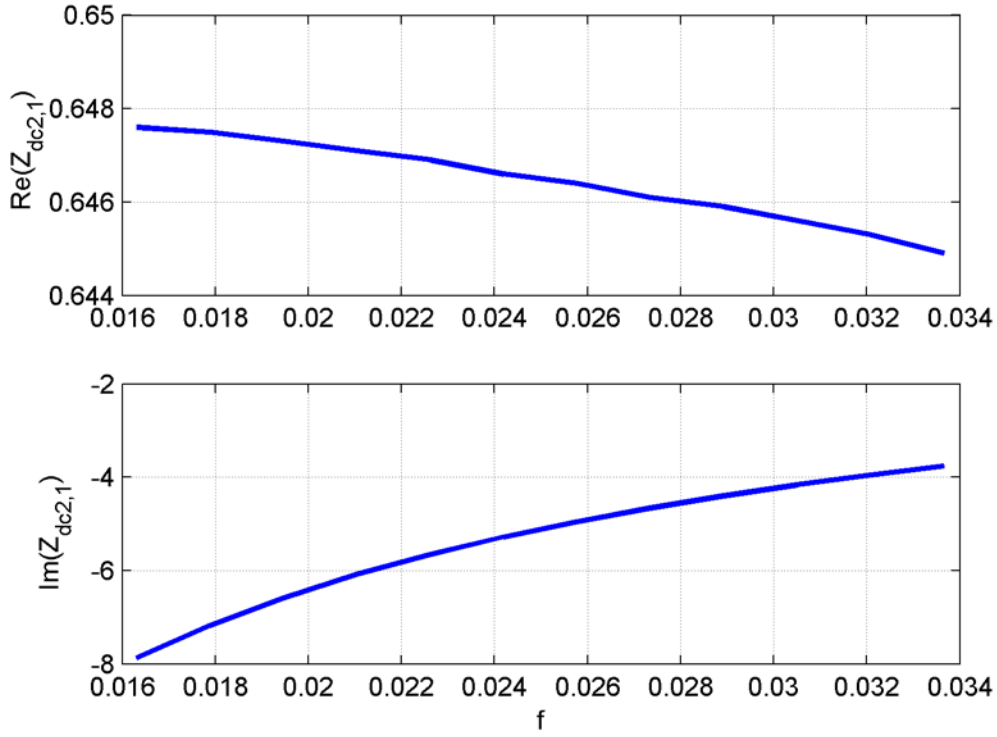

Fig.5.21 Resistant and reactant part of $Z_{dc2,1}$.

The relationship between $\mathrm{Im}(L_{2,1}^{'} + Z_{dc2,1})$ and $F_{piezo,1}$ is illustrated both in Fig.5.22 and Fig.5.23. In Fig.5.22, $m_2^{'}$ is fixed to be 10 with $B_2^{'}$ varying from 0.03 to 0.2. With an

increase of $B_2^{'}$, $\mathrm{Im}(L_{2,1}^{'}+Z_{dc2,1})$ decreases, shown in Fig.5.22(a). Since it is negative within the frequency range, the amplitude thus increases. The corresponding $|F_{piezo,1}|$ is shown in Fig.5.22 (b). if TL_{tar}=4 dB, $|F_{piezo,1}|$ increases with $B_2^{'}$. A conclusion can be drawn that with an increase of the amplitude of $\mathrm{Im}(L_{2,1}^{'}+Z_{dc2,1})$, $|F_{piezo,1}|$ increases correspondingly. This is because, once the target TL is set, the required $V_{2,1}$ is known. So the trends of $|F_{piezo,1}|$ are the same as that of $|\mathrm{Im}(L_{2,1}^{'}+Z_{dc2,1})|$. Fig.5.23 also proves this point. As shown in Fig.5.23 (b), when $m_2^{'}$ equals 60, there is a minimum value of $|F_{piezo,1}|$ at f=0.023. Around this frequency $\mathrm{Im}(L_{2,1}^{'}+Z_{dc2,1})$ reaches zero, which means that the impedance reaches its minimum. Based on the observation above, $|F_{piezo,1}|$ can be tuned with $\mathrm{Im}(L_{2,1}^{'}+Z_{dc2,1})$.

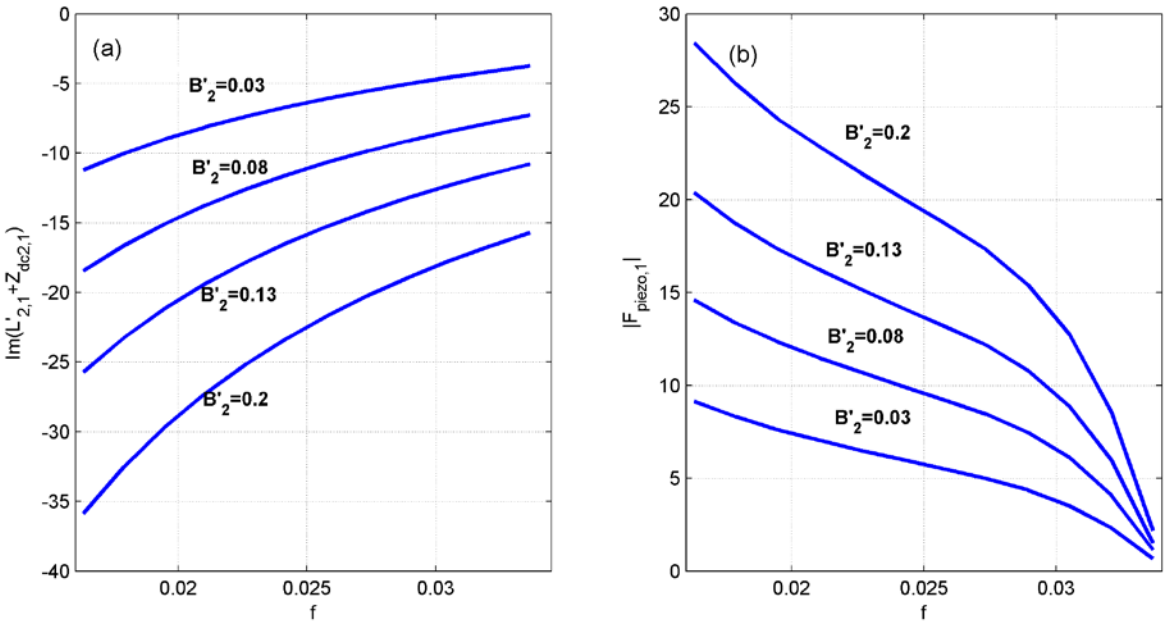

Fig.5.22 (a) $\mathrm{Im}(L_{2,1}^{'}+Z_{dc2,1})$ with $m_2^{'}=10$; (b) the corresponding $|F_{piezo,1}|$.

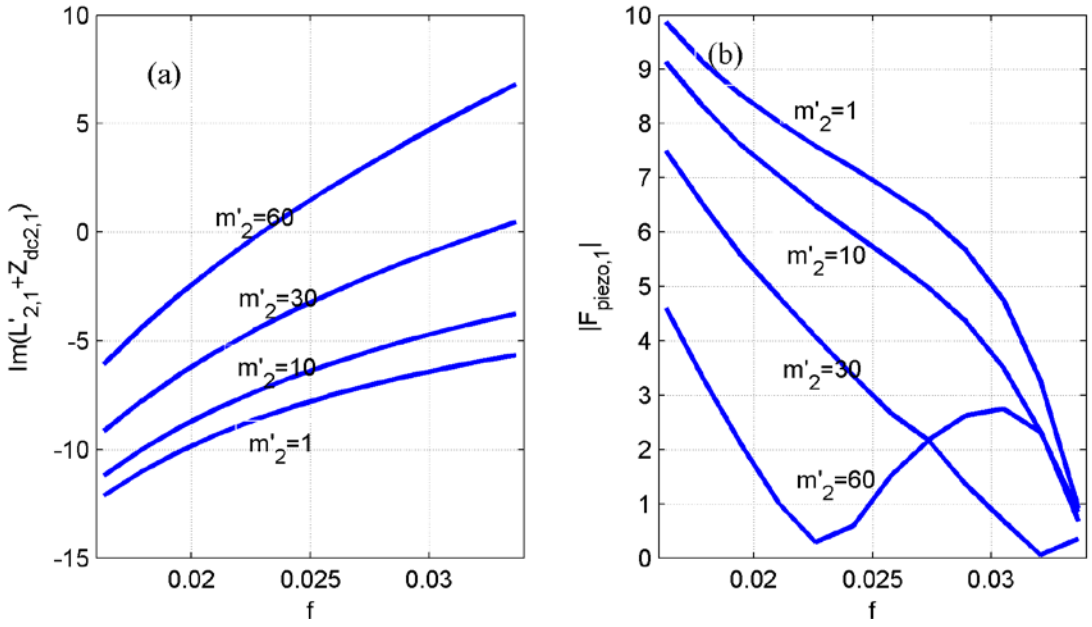

Fig.5.23 (a) $\mathrm{Im}(L_{2,1}^{'}+Z_{dc2,1})$ with $B_2^{'}=0.03$; (b) the corresponding $|F_{piezo,1}|$.

For practical application, the smallest $|F_{piezo,1}|$ is preferred due to its simple realization and for the consideration of the maximum voltage acting upon the piezoelectric actuators. In an ideal case, $\mathrm{Im}(L_{2,1}^{'}+Z_{dc2,1})$ equals zero, which makes the total impedance minimum, expressed as

$$\mathrm{Im}(L_{2,1}^{'})=-\mathrm{Im}(Z_{dc2,1}) \tag{5.85}$$

However, referring to the spectrum of $\mathrm{Im}(Z_{dc2,1})$ in Fig. (5.21), Eq.(5.85) cannot be realized. Since $\frac{\partial[\mathrm{Im}(L_{2,1}^{'}]}{\partial\omega}=m_2^{'}+\frac{B_2^{'}}{\omega^2}$, $\mathrm{Im}(L_{2,1}^{'})$ is monotonically increasing with frequency, while $-\mathrm{Im}(Z_{dc2,1})$ decreases within this range. As a result, $\mathrm{Im}(L_{2,1}^{'})$ cannot fit the ideal value.

Therefore, one of the desired trends of $\mathrm{Im}(L_{2,1}^{'})$ is given in Fig.5.24, with $m_2^{'}=90$ and $B_2^{'}=0.4$. It should be pointed out that this is not the optimized set for

achieving the minimum $\mathrm{Im}(L'_{2,1})$. However, it gives some basic guidelines for achieving a relatively small $\mathrm{Im}(L'_{2,1})$: m'_2,and B'_2 are chosen in a manner so as to 1) let $\mathrm{Im}(L'_{2,1}+Z_{dc2,1})$ spectrum pass through zero; 2) to set the slope of $\mathrm{Im}(L'_{2,1})$ small so that the deviation of $\mathrm{Im}(L'_{2,1})$ from zero is not too large.

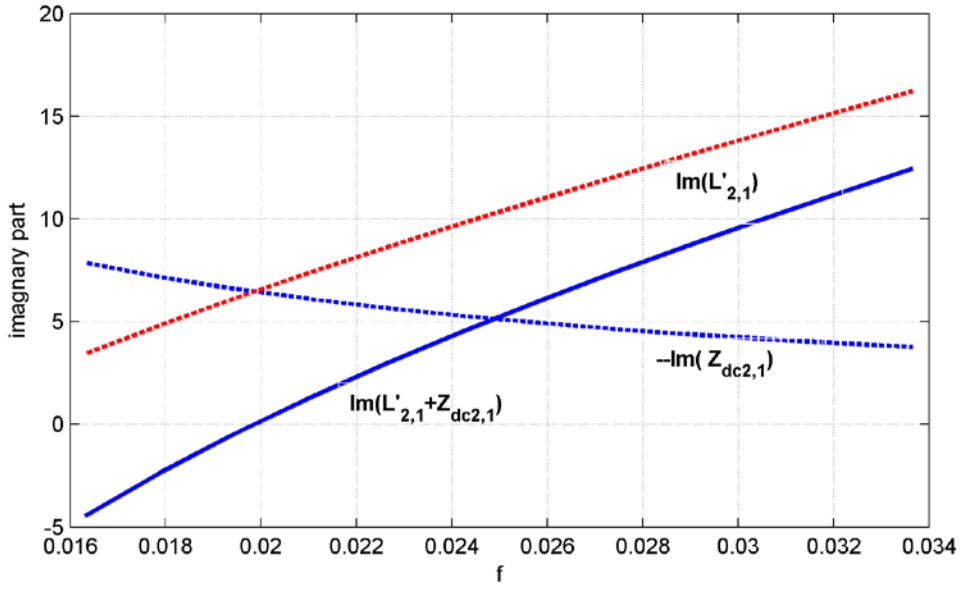

Fig.5.24 Imaginary part of the structure impedance of plate II $\mathrm{Im}(L'_{2,1})$ and the duct and cavity impedance $-\mathrm{Im}(Z_{dc2,1})$, for the first mode with $m'_2 = 90$ and $B'_2 = 0.4$.

C. Voltage derived and material selection

Based on the analysis in Part B, if a small $|F_{piezo,1}|$ is desired, $\mathrm{Im}(L'_{2,1}+Z_{dc2,1})$ should be tuned close to zero. Since its trend is always increasing, a possible way to obtain relatively small value is to define proper m'_2 and B'_2, so that the starting point of the spectrum of $\mathrm{Im}(L'_{2,1}+Z_{dc2,1})$ is negative while the curve will reach zero and become positive. Also it is hoped that the slope of the curve is not too steep. Therefore, $m'_2 = 90$ and $B'_2 = 0.4$ are chosen.

$|F_{piezo,1}|$ is calculated with $m_2^{'}=90$ and $B_2^{'}=0.4$, shown in Fig.5.25. Compared with the corresponding $\mathrm{Im}(L_{2,1}^{'}+Z_{dc2,1})$ shown in Fig. 5.24, within the range *f*=0.016 to 0.021, the amplitude of $\mathrm{Im}(L_{2,1}^{'}+Z_{dc2,1})$ is reduced, and $|F_{piezo,1}|$ is reduced conrrespondingly. While from *f*=0.021 to 0.03, $|F_{piezo,1}|$increases as the amplitude of $\mathrm{Im}(L_{2,1}^{'}+Z_{dc2,1})$ increases.

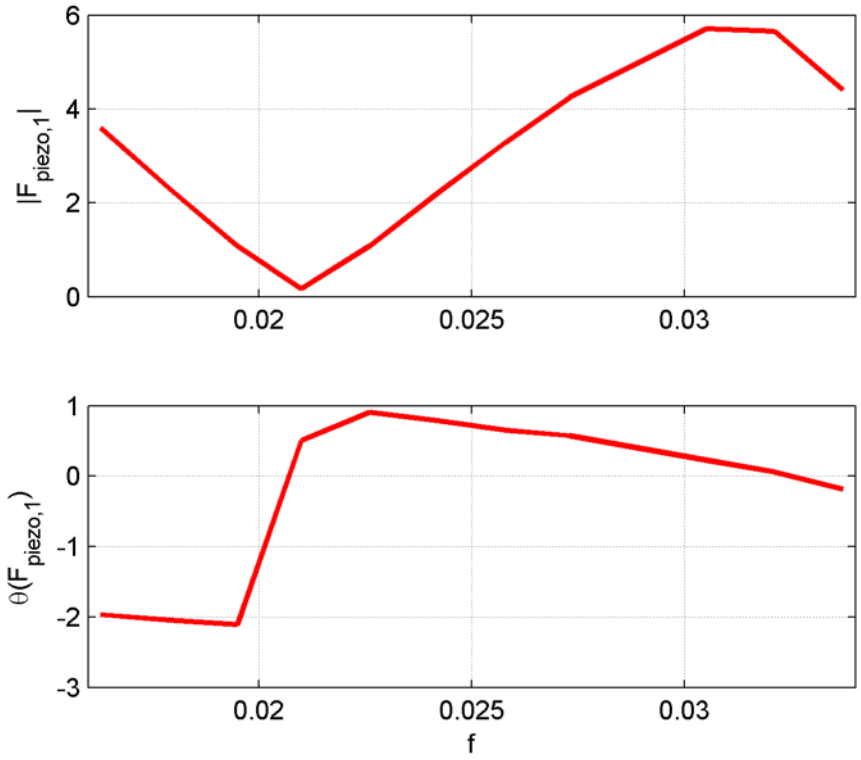

Fig.5.25 Amplitude and phase of $F_{piezo,1}$ with $m_2^{'}=90$ and $B_2^{'}=0.4$.

Referring to Eq. (A.24) and Eq.(A.27) in the Appendix, a possible set of parameters for the plate and actuators is given to satisfy the requirement of $m_2^{'}=90$ and $B_2^{'}=0.4$:as follows

Table 5.5 Properties of plate II and actuators

Thickness of plate II (mm)	2
Length of plate II (mm)	160
Width of plate II (mm)	100
Density of plate II (kg/m^3)	1600
Young's modulus of plate II (Pa)	3×10^9
Thickness of the actuator (mm)	0.7
Length of the actuator (mm)	160
Width of the actuator (mm)	100
Density of the actuator (kg/m^3)	5700
Young's modulus of the actuator(Pa)	7×10^{10}
e_{31} of the actuator (N/Vm)	500

Once the properties of plate II and the actuators are decided, the voltage is obtained from Eq. (5.73), and shown in Fig.5.26.

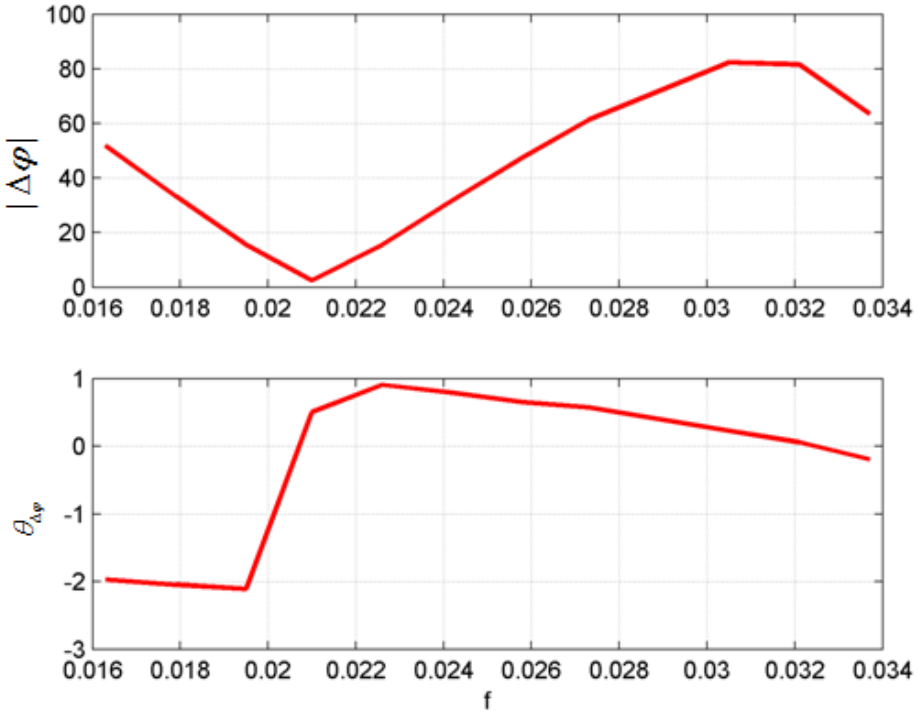

Fig.5.26 Amplitude and phase of the external voltage $\Delta\varphi$.

As a result, the overall performance of the hybrid passive and active noise control system is given in Fig.5.27 by comparison with a pure plate silencer. The dashed line represents the TL performance of a silencer with only plate I without perforations, with m_{b1}=1, B_{b1}=0.105and L_{b1}=5. The working bandwidth is from 0.034 to 0.104. By introducing an absorption mechanism by micro-perforation to plate I with perforation ration 0.5% and diameter 0.005, and by the active control mechanism with plate II driven by piezoelectric actuators with the external input voltage shown in Fig.5.26, the TL performance in the very low frequency range as well as the medium range are both improved, with the working range from 0.016 to 0.184. Therefore, the working band is increased by 377%. It is noted that there is a peak arising between the original first and second TL peaks, which is due to the resonance frequency of the composite plate II decided by $m_2^{'}$ and $B_2^{'}$,.the principle is already explained in Sec.5.3.

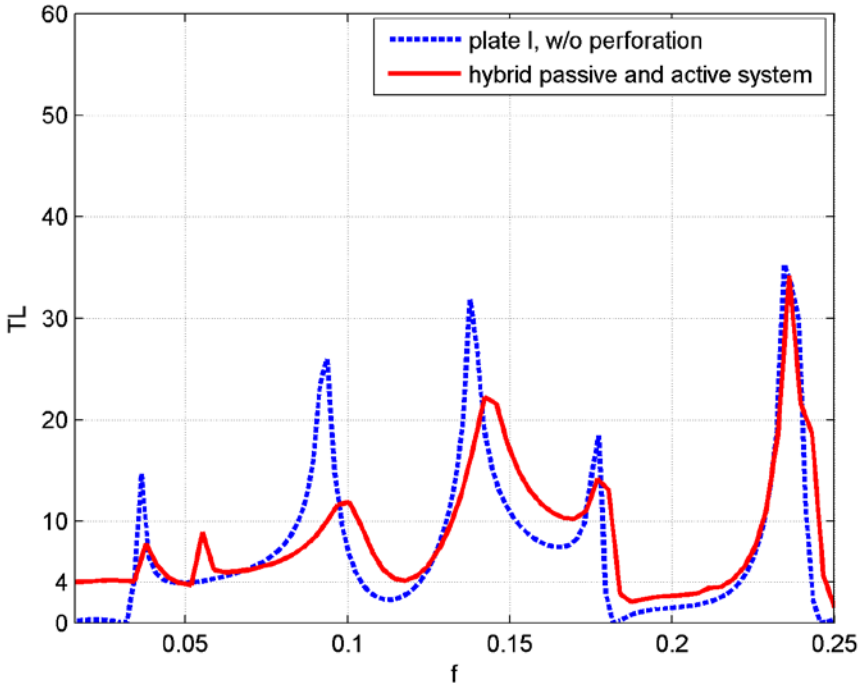

Fig.5.27 Performance of the hybrid passive and active noise control system.

5.8 Summary

A hybrid passive and active noise control device is developed based on the model of plate silencer with micro-perforations. An extra plate is used for attaching piezoelectric actuators. The study mainly proceeded as follows

1) A theoretical model of the hybrid system has been developed. The model takes the mass and bending stiffness of piezoelectric actuators as well as the coupling between two plates into consideration.

2) A parametric study of the hybrid system in passive mode is carried out. It turns out that the length of plate II is a very important factor influencing theTL performance. If the length of plate II is very small such as L_{b2}=1 when L_{b1}=5, the coupling can be ignored. A small L_{b2} gives two plates flexible and relatively independent parameter choices. Moreover, the overall mass and bending stiffness of plate II affect the system with extra TL peak arising within the original working range dominated by plate I.

3) The active mode of the system has been established based on the several simplifications. Firstly, only the first two modes are used to describe the system performance. Secondly, within this range, the coupling between the first two modes can be ignored. The tuning process of the external electrical force with the variation of the structure impedance of plate II has been

discussed. It turns out that if the reactant part of the structure impedance of plate II is set to be small, the driving force provided by actuators is relatively small. A possible set of the properties of plate II and the actuators is proposed to indicate the possibility for realization of the hybrid noise control system.

4) The performance of the hybrid system is determined by using optimal values for plates I and II. By integrating micro-perforations to one plate and an active control method on another plate, the bandwidth outperforms the original single plate by about three-fold.

CHAPTER 6

CONCLUSION AND FURTHER STUDY

6.1 Conclusion

A hybrid passive and active noise control system by adopting strong coupling between the structure and acoustic waves has been developed through mathematical analysis, physical explanation and experimental validation. The hybrid device in this study is proposed based on a plate silencer. The plate silencer is composed of a plate backed by a rigid cavity inserted into the duct wall. When incident sound waves arrive, the plate is induced to vibrate. Upon proper tuning of the plate parameters, the plate, flush-mounted with the inner duct wall, reflects the sound, creating favourable interference with the incoming sound. However, there are some limitations, such as 1) The plate should have a very high bending stiffness and a very low mass ratio. Failure to ensure this results in a significant reduction in both the Transmission Loss (TL) level and the stopband. 2) The performance of the silencer is highly non-uniform across the frequency range, as demonstrated by the drastic fluctuation as well as the existence of troughs (passband) in the medium frequency range of the TL curve. This not only directly contributes to narrowing the stopband of the device, but also limits the use of the device for broadband noise control.

In order to achieve a wider stopband, a plate silencer with micro-perforations is

proposed in this work as the first step towards developing the hybrid control system. Micro-perforations are introduced into a very light and moderately stiff plate. The purpose of the micro-perforations is to introduce sound absorptions to compensate for the deficiency in the passband caused by the insufficient sound reflection due to the plate with a weaker strength to mass ratio. The proposed silencer differs from the existing plate silencer in that sound reflection and absorption have a dominant effect at different frequency ranges to provide a more flattened/uniformed TL curve. A two-dimensional theoretical model is established for a plate silencer with micro-perforations. The leading and trailing edges of the plate are clamped, while the other two lateral edges are set free. The performance of the plate silencer with micro-perforations is studied. The focus is on the differences in performance before and after introducing the micro-perforations. The effects of the micro-perforations are threefold:

1) Micro-perforation introduces absorptions to the system. By doing so, the original TL trough point between the second and third peaks due to the insufficient sound reflection of the plate with weaker bending stiffness can be lifted up, contributing to a broadening of the stopband.

2) Micro-perforation allows reduction of the reactance of the equivalent structural impedance like a virtual negative mass. This results in a shift of the system resonance to higher frequencies, adding its contribution to the

stopband broadening.

3) Along with the micro-perforations, the sound radiation and structural response of the plate are compromised through a dual process of pressure balance between the two sides of the plate and impaired sound radiation efficiency of the perforated plate. As a result, the sharp peaks on the TL curve provided by original plate silencers are smoothed out. Together with the effects mentioned in a) and b), a more flattened/uniformed broadband silencer can be achieved. The theoretical study reveals that the proposed silencer of rectangular shape with two plates with micro-perforations can work effectively over a wide bandwidth. A stopband over 10 dB with the ratio f_2/f_1=3.45 can be achieved when the plate has unit mass ratio and dimensionless bending stiffness of 0.057 with a micro-perforation hole size of d=0.007 and perforation ratio of 0.7%.

Optimization for the balance between absorption and reflection of the plate silencer with micro-perforations is carried out. The micro-perforation effect can be best seen when a minimum level of bending stiffness of the plate is ensured to substantiate a reasonable level of sound radiation. When properly designed, the silencer can provide a stopband which is even larger than that of a conventional plate silencer with much higher stiffness.

Experimental studies are carried out. A composite plate satisfying the requirement for the mass and bending stiffness is fabricated. PMI is chosen as the core material while carbon fibre is the reinforcement used due to its light and stiff characteristics. Different quantities of carbon fiber tows can render high flexibility in varying the bending stiffness of the composite plate with slight variation in the weight. There is roughly agreement between the experimental data and the theoretical predictions.

For the second step in developing the hybrid system, piezoelectric actuators are attached symmetrically to both the top and the bottom of an extra plate, which is denoted as plate II while the previous micro-perforated plate is denoted as plate I. The reason for adding another plate is not to deteriorate the performance of plate I for extra mass and bending stiffness of the actuators. A theoretical model is established to predict the hybrid system with two plate coupling as well as the effect of the actuator on the system both in a passive and active way. Two modes are defined for the hybrid system, which are the passive mode (external voltage is zero) and the active mode (external voltage is non-zero). Parametric study reveals that by properly choosing the properties of the two plates, they can undertake different tasks in different frequency ranges. Plate I is longer with a dimensionless length of 5 and micro-perforated. It works in a similar way to that of the plate silencer studied in Chapters 2 and 3. Plate II is shorter with a length of 1.6, and it works in the low frequency range which is beyond the working range of plate I. The difference between the two lengths ensures that the couplings between the two plates are very small. Optimization is also carried out for

the hybrid system in passive mode. The method is the same as for the plate silencer with micro-perforations.

A very simple active control algorithm is then proposed based on several simplifications, such as in the very low frequencies, the performance of the hybrid system in passive mode can be described with only the first two modes and further by ignoring the coupling between the first two modes. Therefore, the problem of how to obtain a target TL is simplified into how to obtain a target first mode of plate II. Also due to the simplifications, there is a linear relationship between the driving force provided by the actuator and structure impedance of the composite plate II. By selecting the structure impedance of plate II, the external driving force can be tuned. Attempts are also made to give a guideline for choosing the material for the plate and actuator for practical application. As a result, the hybrid system can improve the TL performance by widening the working bandwidth 3.7 times that of the original plate silencer.

6.2 Further study

Based on the present study, there is some further work that can be done as follows

1) Experiments can be carried out to validate the hybrid passive and active noise control systems. The relationship between the input external electrical signal and the final TL performance is studied using sensitivity analysis

between the amplitude / phase of the voltage and the TL.

2) For the hybrid active and passive noise control device, a pair of identical actuators is adhered to plate I, and is driven out of phase to induce pure transverse vibration. However, for practical application, the actuator in the duct side will influence the reflection of sound due to the sudden change of the plate surface. This effect is excluded in the present study. For more practical purposes, only one actuator can be used. In this case, both the transverse displacement and extensional displacement should be calculated.

3) Only one side-branch plate silencer is studied in Chapter 5 for simpler calculation. Thus the TL criterion has to be reset. For further study, two side branch plate silencers can be modelled and the result can be compared with the plate silencer with micro-perforations in Chapters 2 and 3.

4) Optimization can be conducted for the external driving force and the structure impedance of plate II. For the current study, only one desired trends is proposed.

APPENDIX

Double integration in Eq. (2.22):

$$\Pi_{1,1}=\frac{k_0(e^{\beta_j+\beta_l}-1)}{(\beta_j+ik_nL)(\beta_j+\beta_l)}-\frac{k_0(e^{\beta_j+\beta_l}-1)}{(\beta_j-ik_nL)(\beta_j+\beta_l)}-\frac{k_0(e^{\beta_l-ik_nL}-1)}{(\beta_j+ik_nL)(\beta_l-ik_nL)}+\frac{k_0(e^{\beta_l}-e^{-ik_nL})}{(\beta_j-ik_nL)}e^{\beta_j},(j=l) \tag{A.1}$$

$$\Pi_{1,1}=\frac{k_0(e^{\beta_l-\beta_j}-1)}{(\beta_j-ik_nL)(\beta_j-\beta_l)}-\frac{k_0(e^{\beta_l-\beta_j}-1)}{(\beta_j+ik_nL)(\beta_j-\beta_l)}+\frac{k_0(e^{\beta_l-ik_nL}-1)}{(\beta_j-ik_nL)(\beta_l-ik_nL)}-\frac{k_0(e^{\beta_l}-e^{-ik_nL})e^{-\beta_j}}{(\beta_j+ik_nL)(\beta_l+ik_nL)},(j\neq l) \tag{A.2}$$

$$\Pi_{1,2}=\frac{k_0(e^{\beta_l-ik_nL}-1)}{(\beta_j-ik_nL)(\beta_l-ik_nL)}-\frac{k_0(e^{\beta_l}-e^{-ik_nL})e^{-\beta_j}}{(\beta_j+ik_nL)(\beta_l+ik_nL)}+\frac{k_0}{(\beta_j+ik_nL)}-\frac{k_0}{(\beta_j-ik_nL)} \tag{A.3}$$

$$\Pi_{1,3}=\frac{2ik_0k_nL((\beta_l\sin\beta_j-\beta_j\cos\beta_j)e^{\beta_j}+\beta_j)}{(\beta_j^2-(k_nL)^2)(\beta_j^2+\beta_l^2)}-\frac{k_0(e^{\beta_l}-e^{-ik_nL})}{(\beta_j^2-(k_nL)^2)(\beta_l+ik_nL)}(ik_nL\sin\beta_j+\beta_j\cos\beta_j) \tag{A.4}$$

$$\Pi_{1,4}=\frac{ik_0k_nL(1-e^{\beta_l-ik_nL})}{(\beta_j^2-(k_nL)^2)(\beta_l-ik_nL)}+\frac{k_0\beta_j((\beta_l\sin\beta_j-\beta_j\cos\beta_j)e^{\beta_j}+\beta_j)}{(\beta_j^2-(k_nL)^2)(\beta_j^2+\beta_l^2)}+\frac{ik_0k_nL((\beta_l\sin\beta_j+\beta_j\cos\beta_j)e^{\beta_j}-\beta_j)}{(\beta_j^2-(k_nL)^2)(\beta_j^2+\beta_l^2)}+\frac{k_0(\beta_j\sin\beta_j-ik_nL\cos\beta_j)(e^{\beta_j}-e^{-ik_nL})}{(\beta_j^2-(k_nL)^2)(\beta_l+ik_nL)}-\frac{k_0\beta_j((\beta_l\sin\beta_j-\beta_j\cos\beta_j)e^{\beta_j}+\beta_j)}{(\beta_j^2-(k_nL)^2)(\beta_j^2+\beta_l^2)}+\frac{ik_0k_nL((\beta_j\sin\beta_j+\beta_l\cos\beta_j)e^{\beta_l}+\beta_l)}{(\beta_j^2-(k_nL)^2)(\beta_j^2+\beta_l^2)},(j=l) \tag{A.5}$$

$$\Pi_{1,4}=\frac{k_0(e^{\beta_j-\beta_l}-1)}{(\beta_j+ik_nL)(\beta_j-\beta_l)}+\frac{k_0(e^{-ik_nL-\beta_l}-1)}{(\beta_j+ik_nL)(\beta_l+ik_nL)}-\frac{k_0(e^{\beta_j-\beta_l}-1)}{(\beta_j-ik_nL)(\beta_j-\beta_l)}+\frac{k_0(e^{-ik_nL}-e^{-\beta_l})e^{-\beta_j}}{(\beta_j-ik_nL)(\beta_l-ik_nL)}\frac{ik_nL(1-e^{\beta_l-ik_nL})}{(\beta_j^2-(k_nL)^2)}+\frac{k_0\beta_j((\beta_l\sin\beta_j-\beta_j\cos\beta_j)e^{\beta_j}+\beta_j)}{(\beta_j^2-(k_nL)^2)},(j\neq l) \tag{A.6}$$

$$\Pi_{2,1}=\frac{k_0}{(\beta_j+ik_nL)}+\frac{k_0(e^{-\beta_l-ik_nL}-1)}{(\beta_j+ik_nL)(\beta_l+ik_nL)}-\frac{k_0}{(\beta_j-ik_nL)}-\frac{k_0(e^{-\beta_l}-e^{-ik_nL})e^{-\beta_j}}{(\beta_j-ik_nL)(\beta_l-ik_nL)} \tag{A.7}$$

$$\Pi_{2,2}=\frac{k_0(1-e^{-(\beta_j+\beta_l)})}{(\beta_j-ik_nL)(\beta_j+\beta_l)}+\frac{k_0(1-e^{-\beta_l+ik_nL})}{(\beta_j-ik_nL)(\beta_l+ik_nL)}+\frac{k_0(1-e^{-(\beta_j+\beta_l)})}{(\beta_j+ik_nL)(\beta_j+\beta_l)}$$
$$-\frac{k_0(e^{-ik_nL}-e^{-\beta_l})e^{-\beta_j}}{(\beta_j+ik_nL)(\beta_l-ik_nL)} \quad \text{(A.8)}$$

$$\Pi_{2,3}=\frac{2ik_0k_nL(\beta_j-(\beta_l\sin\beta_j+\beta_j\cos\beta_j)e^{-\beta_l})}{(\beta_j^2-(k_nL)^2)(\beta_j^2+\beta_l^2)}$$
$$+\frac{\beta_jk_0(1-e^{-\beta_l-ik_nL})}{(\beta_j^2-(k_nL)^2)(\beta_l+ik_nL)}+\frac{k_0(e^{-\beta_l}-e^{-ik_nL})(ik_nL\sin\beta_j+\beta_j\cos\beta_j)}{(\beta_j^2-(k_nL)^2)(\beta_l-ik_nL)} \quad \text{(A.9)}$$

$$\Pi_{2,4}=-\frac{ik_0k_nL(1-e^{-\beta_l-ik_nL})}{(\beta_j^2-(k_nL)^2)(\beta_l+ik_nL)}+\frac{2ik_0k_nL(\beta_l+(\beta_j\sin\beta_j-\beta_l\cos\beta_j)e^{-\beta_l})}{(\beta_j^2-(k_nL)^2)(\beta_j^2+\beta_l^2)}$$
$$-\frac{k_0(\beta_j\sin\beta_j-ik_nL\cos\beta_j)(e^{-\beta_l}-e^{-ik_nL})}{(\beta_j^2-(k_nL)^2)(\beta_l-ik_nL)} \quad \text{(A.10)}$$

$$\Pi_{3,1}=\frac{k_0(\beta_l-(ik_nL\sin\beta_l+\beta_l\cos\beta_l)e^{-ik_nL})}{(\beta_j+ik_nL)(\beta_l^2-(k_nL)^2)}+\frac{k_0((\beta_j\sin\beta_l+\beta_l\cos\beta_l)e^{\beta_l}+\beta_l)}{(\beta_j+ik_nL)(\beta_j^2+\beta_l^2)}$$
$$+\frac{k_0e^{\beta_j}(ik_nL\sin\beta_l-\beta_l\cos\beta_l+\beta_le^{-ik_nL})}{(\beta_j-ik_nL)(\beta_l^2-(k_nL)^2)}-\frac{k_0(\beta_j\sin\beta_le^{\beta_l}-e^{\beta_l}\beta_l\cos\beta_l+\beta_l)}{(\beta_j-ik_nL)(\beta_j^2+\beta_l^2)} \quad \text{(A.11)}$$

$$\Pi_{3,2}=\frac{k_0(\beta_l-(ik_nL\sin\beta_l+\beta_l\cos\beta_l)e^{-ik_nL})}{(\beta_j-ik_nL)(\beta_l^2-(k_nL)^2)}+\frac{k_0(-(\beta_j\sin\beta_l+\beta_l\cos\beta_l)e^{\beta_j}+\beta_l)}{(\beta_j-ik_nL)(\beta_j^2+\beta_l^2)}$$
$$-\frac{k_0e^{\beta_j}(ik_nL\sin\beta_l-\beta_l\cos\beta_l+\beta_le^{-ik_nL})}{(\beta_j+ik_nL)(\beta_l^2-(k_nL)^2)}-\frac{k_0(-\beta_j\sin\beta_le^{\beta_l}-e^{\beta_l}\beta_l\cos\beta_l+\beta_l)}{(\beta_j-ik_nL)(\beta_j^2+\beta_l^2)} \quad \text{(A.12)}$$

$$\Pi_{3,3}=\frac{k_0\beta_j(\beta_l-(ik_nL\sin\beta_l+\beta_l\cos\beta_l)e^{-ik_nL})}{(\beta_j^2-(k_nL)^2)(\beta_l^2-(k_nL)^2)}$$
$$-\frac{k_0(ik_nL\sin\beta_j+\beta_l\cos\beta_j)(ik_nL\sin\beta_l-\beta_l\cos\beta_j+\beta_le^{-ik_nL})}{(\beta_j^2-(k_nL)^2)(\beta_l^2-(k_nL)^2)}$$
$$+\frac{ik_0k_nL}{(\beta_j^2-(k_nL)^2)}[\frac{\sin(\beta_j-\beta_l)}{\beta_j-\beta_l}-\frac{\sin(\beta_j+\beta_l)}{\beta_j+\beta_l}],\ j\neq l \quad \text{(A.13)}$$

$$\Pi_{3,3}=\frac{k_0\beta_j(\beta_l-(ik_nL\sin\beta_l+\beta_l\cos\beta_l)e^{-ik_nL})}{(\beta_j^2-(k_nL)^2)(\beta_l^2-(k_nL)^2)}$$
$$-\frac{k_0(ik_nL\sin\beta_j+\beta_l\cos\beta_j)(ik_nL\sin\beta_l-\beta_l\cos\beta_j+\beta_l e^{-ik_nL})}{(\beta_j^2-(k_nL)^2)(\beta_l^2-(k_nL)^2)} \tag{A.14}$$
$$+\frac{ik_0k_nL}{(\beta_j^2-(k_nL)^2)}[1-\frac{\sin(\beta_j+\beta_l)}{\beta_j+\beta_l}],\ j=l$$

$$\Pi_{3,4}=\frac{-ik_0k_nL[\beta_l-(ik_nL\sin\beta_l+\beta_l\cos\beta_l)e^{-ik_nL}]}{(\beta_j^2-(k_nL)^2)(\beta_l^2-(k_nL)^2)}$$
$$+\frac{k_0(\beta_j\sin\beta_j-ik_nL\cos\beta_j)[ik_nL\sin\beta_l-\beta_l\cos\beta_l+\beta_l e^{-ik_nL}]}{(\beta_j^2-(k_nL)^2)(\beta_l^2-(k_nL)^2)} \tag{A.15}$$
$$+\frac{ik_0k_nL}{(\beta_j^2-(k_nL)^2)}[\frac{1-\cos(\beta_j+\beta_l)}{\beta_j+\beta_l}-\frac{1-\cos(\beta_j-\beta_l)}{\beta_j-\beta_l}],\ j\neq l$$

$$\Pi_{3,4}=\frac{-ik_0k_nL[\beta_l-(ik_nL\sin\beta_l+\beta_l\cos\beta_l)e^{-ik_nL}]}{(\beta_j^2-(k_nL)^2)(\beta_l^2-(k_nL)^2)}$$
$$+\frac{k_0(\beta_j\sin\beta_j-ik_nL\cos\beta_j)[ik_nL\sin\beta_l-\beta_l\cos\beta_l+\beta_l e^{-ik_nL}]}{(\beta_j^2-(k_nL)^2)(\beta_l^2-(k_nL)^2)} \tag{A.16}$$
$$+\frac{ik_0k_nL}{(\beta_j^2-(k_nL)^2)}[\frac{1-\cos(\beta_j+\beta_l)}{\beta_j+\beta_l}],\ j=l$$

$$\Pi_{4,1}=-\frac{k_0[(\beta_l\sin\beta_l-ik_nL\cos\beta_l)e^{-ik_nL}+ik_nL]}{(\beta_j+ik_nL)(\beta_l^2-(k_nL)^2)}+\frac{k_0[(\beta_l\sin\beta_l+\beta_j\cos\beta_l)e^{\beta_j}-\beta_j]}{(\beta_j+ik_nL)(\beta_j^2+\beta_l^2)} \tag{A.17}$$
$$+\frac{k_0e^{\beta_j}[\beta_l\sin\beta_l+ik_nL\cos\beta_l-ik_nLe^{-ik_nL}]}{(\beta_j-ik_nL)(\beta_l^2-(k_nL)^2)}-\frac{k_0[(\beta_l\sin\beta_l+\beta_j\cos\beta_l)e^{\beta_j}-\beta_j]}{(\beta_j-ik_nL)(\beta_j^2+\beta_l^2)}$$

$$\Pi_{4,2}=\frac{k_0[(\beta_l\sin\beta_l-ik_nL\cos\beta_l)e^{-ik_nL}+ik_nL]}{(\beta_j-ik_nL)(\beta_l^2-(k_nL)^2)}-\frac{k_0[(\beta_l\sin\beta_l-\beta_j\cos\beta_l)e^{-\beta_j}+\beta_j]}{(\beta_j-ik_nL)(\beta_j^2+\beta_l^2)} \tag{A.18}$$
$$-\frac{k_0e^{-\beta_j}[\beta_l\sin\beta_l+ik_nL\cos\beta_l-ik_nLe^{-ik_nL}]}{(\beta_j+ik_nL)(\beta_l^2-(k_nL)^2)}+\frac{k_0[(\beta_l\sin\beta_l-\beta_j\cos\beta_l)e^{-\beta_j}+\beta_j]}{(\beta_j+ik_nL)(\beta_j^2+\beta_l^2)}$$

$$\Pi_{4,3}=\frac{k_0\beta_j[\beta_l\sin\beta_l e^{-ik_nL}-ik_nL\cos\beta_l e^{-ik_nL}+ik_nL]}{(\beta_j^2-(k_nL)^2)(\beta_l^2-(k_nL)^2)}$$
$$-\frac{k_0(ik_nL\sin\beta_l+\beta_l\cos\beta_l)[\beta_l\sin\beta_l+ik_nL\cos\beta_l-ik_nLe^{-ik_nL}]}{(\beta_j^2-(k_nL)^2)(\beta_l^2-(k_nL)^2)} \tag{A.19}$$
$$+\frac{ik_nLk_0}{(\beta_j^2-(k_nL)^2)}[\frac{1-\cos(\beta_j+\beta_l)}{\beta_j+\beta_l}],\ j=l$$

$$\Pi_{4,3}=\frac{k_0\beta_j[\beta_l\ \sin\beta_l\, e^{-ik_nL}-ik_nL\cos\beta_l\, e^{-ik_nL}+ik_nL]}{(\beta_j^2-(k_nL)^2)(\beta_l^2-(k_nL)^2)}$$
$$-\frac{k_0(ik_nL\sin\beta_l+\beta_l\ \cos\beta_l)[\beta_l\ \sin\beta_l+ik_nL\cos\beta_l-ik_nLe^{-ik_nL}]}{(\beta_j^2-(k_nL)^2)(\beta_l^2-(k_nL)^2)} \tag{A.20}$$
$$+\frac{ik_nLk_0}{(\beta_j^2-(k_nL)^2)}[\frac{1-\cos(\beta_j+\beta_l)}{\beta_j+\beta_l}+\frac{1-\cos(\beta_j-\beta_l)}{\beta_j-\beta_l}],\ j\neq l$$

$$\Pi_{4,4}=\frac{-k_0ik_nL[\beta_l\ \sin\beta_l\, e^{-ik_nL}-ik_nL\cos\beta_l\, e^{-ik_nL}+ik_nL]}{(\beta_j^2-(k_nL)^2)(\beta_l^2-(k_nL)^2)}$$
$$-\frac{k_0(\beta_l\ \sin\beta_l-ik_nL\cos\beta_j)[\beta_l\ \sin\beta_l+ik_nL\cos\beta_l-ik_nLe^{-ik_nL}]}{(\beta_j^2-(k_nL)^2)(\beta_l^2-(k_nL)^2)} \tag{A.21}$$
$$+\frac{ik_nLk_0}{(\beta_j^2-(k_nL)^2)}[\frac{\sin(\beta_j+\beta_l)}{\beta_j+\beta_l}+\frac{\sin(\beta_j-\beta_l)}{\beta_j-\beta_l}],\ j\neq l$$

$$\Pi_{4,4}=\frac{-k_0ik_nL[\beta_l\ \sin\beta_l\, e^{-ik_nL}-ik_nL\cos\beta_l\, e^{-ik_nL}+ik_nL]}{(\beta_j^2-(k_nL)^2)(\beta_l^2-(k_nL)^2)}$$
$$-\frac{k_0(\beta_l\ \sin\beta_l-ik_nL\cos\beta_j)[\beta_l\ \sin\beta_l+ik_nL\cos\beta_l-ik_nLe^{-ik_nL}]}{(\beta_j^2-(k_nL)^2)(\beta_l^2-(k_nL)^2)} \tag{A.22}$$
$$+\frac{ik_nLk_0}{(\beta_j^2-(k_nL)^2)}[\frac{\sin(\beta_j+\beta_l)}{\beta_j+\beta_l}+1],\ j=l$$

The coefficients of Eq.(5.57)~(5.66):

$$K_{b2,j}=\frac{L_{b2}\rho_{b2}b_{b2}h_{b2}}{4} \tag{A.23}$$

$$K_{piezo1,jl}=\begin{cases}\frac{\rho_{p1}b_{p1}h_{p1}L_{b2}}{4}[\frac{\sin((j-l)\pi\xi)}{(j-l)\pi}-\frac{\sin((j+l)\pi\xi)}{(j+l)\pi}]\Big|_{\frac{(x_{p1}-\frac{L_{p1}}{2})}{L_{b2}}+\frac{1}{2}}^{\frac{(x_{p1}+\frac{L_{p1}}{2})}{L_{b2}}+\frac{1}{2}}, & j\neq l\\ \frac{\rho_{p1}b_{p1}h_{p1}L_{b2}}{4}[\xi-\frac{1}{2j\pi}\sin(2j\pi\xi)]\Big|_{\frac{(x_{p1}-\frac{L_{p1}}{2})}{L_{b2}}+\frac{1}{2}}^{\frac{(x_{p1}+\frac{L_{p1}}{2})}{L_{b2}}+\frac{1}{2}}, & j=l\end{cases} \tag{A.24}$$

$$K_{piezo2,jl}=\begin{cases}\frac{\rho_{p2}b_{p2}h_{p2}L_{b2}}{4}[\frac{\sin((j-l)\pi\xi)}{(j-l)\pi}-\frac{\sin((j+l)\pi\xi)}{(j+l)\pi}]\Big|_{\frac{(x_{p2}-\frac{L_{p2}}{2})}{L_{b2}}+\frac{1}{2}}^{\frac{(x_{p2}+\frac{L_{p2}}{2})}{L_{b2}}+\frac{1}{2}}, & j\neq l\\ \frac{\rho_{p2}b_{p2}h_{p2}L_{b2}}{4}[\xi-\frac{1}{2j\pi}\sin(2j\pi\xi)]\Big|_{\frac{(x_{p2}-\frac{L_{p2}}{2})}{L_{b2}}+\frac{1}{2}}^{\frac{(x_{p2}+\frac{L_{p2}}{2})}{L_{b2}}+\frac{1}{2}}, & j=l\end{cases} \tag{A.25}$$

$$P_{b2,j} = \frac{L_{b2} b_{b2} {Y_{b2}}^4 {h_{b2}}^3}{48} (\frac{j\pi}{L_{b2}})^4 \tag{A.26}$$

$$P_{piezo11,jl} = \frac{L_{b2} Y_{11\_p1} b_{p1}}{4} \cdot (\frac{h_{p1}^3}{12} + (\frac{h_{p1}+h_{b2}}{2})^2 \cdot h_{p1})(\frac{\pi}{L_{b2}})^4 \begin{cases} j^2 l^2 [\frac{\sin((j-l)\pi\xi)}{(j-l)\pi} - \frac{\sin((j+l)\pi\xi)}{(j+l)\pi}] \Big|_{\frac{(x_{p1}-\frac{L_{p1}}{2})}{L_{b2}}+\frac{1}{2}}^{\frac{(x_{p1}+\frac{L_{p1}}{2})}{L_{b2}}+\frac{1}{2}}, & j \neq l \\ j^4 [\xi - \frac{1}{2j\pi}\sin(2j\pi\xi)] \Big|_{\frac{(x_{p1}-\frac{L_{p1}}{2})}{L_{b2}}+\frac{1}{2}}^{\frac{(x_{p1}+\frac{L_{p1}}{2})}{L_{b2}}+\frac{1}{2}}, & j = l \end{cases} \tag{A.27}$$

$$P_{piezo12,jl} = L_{b2} \frac{(e_{31\_p1} \Delta\varphi_{p1} b_{p1})(h_{p1}+h_{b2})}{2} \cdot (\frac{\pi}{L_{b2}})^2 j^2 [-\frac{\cos(j\pi\xi)}{j\pi}] \Big|_{\frac{(x_{p1}-\frac{L_{p1}}{2})}{L_{b2}}+\frac{1}{2}}^{\frac{(x_{p1}+\frac{L_{p1}}{2})}{L_{b2}}+\frac{1}{2}} \tag{A.28}$$

$$P_{piezo13} = -\frac{\varepsilon_{33\_p1} b_{p1} h_{p1} L_{p1}}{2} (\frac{\Delta\varphi_{p1}}{h_{p1}})^2 \tag{A.29}$$

$$P_{piezo21,jl} = \frac{1}{2} L_{b2} \frac{Y_{11\_p2} b_{p2}}{2} \cdot (\frac{h_{p2}^3}{12} + (\frac{h_{p2}+h_{b2}}{2})^2 \cdot h_{p2})(\frac{\pi}{L_{b2}})^4 \begin{cases} j^2 l^2 [\frac{\sin((j-l)\pi\xi)}{(j-l)\pi} - \frac{\sin((j+l)\pi\xi)}{(j+l)\pi}] \Big|_{\frac{(x_{p2}-\frac{L_{p2}}{2})}{L_{b2}}+\frac{1}{2}}^{\frac{(x_{p2}+\frac{L_{p2}}{2})}{L_{b2}}+\frac{1}{2}}, & j \neq l \\ j^4 [\xi - \frac{1}{2j\pi}\sin(2j\pi\xi)] \Big|_{\frac{(x_{p2}-\frac{L_{p2}}{2})}{L_{b2}}+\frac{1}{2}}^{\frac{(x_{p2}+\frac{L_{p2}}{2})}{L_{b2}}+\frac{1}{2}}, & j = l \end{cases} \tag{A.30}$$

$$P_{piezo22,jl} = -L_{b2} \frac{(e_{31\_p2} \Delta\varphi_{p2} b_{p2}) \cdot (h_{p2}+h_{b2})}{2} \cdot (\frac{\pi}{L_{b2}})^2 j^2 [-\frac{\cos(j\pi\xi)}{j\pi}] \Big|_{\frac{(x_{p2}-\frac{L_{p2}}{2})}{L_{b2}}+\frac{1}{2}}^{\frac{(x_{p2}+\frac{L_{p2}}{2})}{L_{b2}}+\frac{1}{2}} \tag{A.31}$$

$$P_{piezo23} = -\frac{\varepsilon_{33\_p2} b_{p2} h_{p2} L_{p2}}{2} (\frac{\Delta\varphi_{p2}}{h_{p2}})^2 \tag{A.32}$$

$$F_{cav2,jl} = \frac{i\omega L_{b2} b_{b2}}{4} Z_{cav2,jl} \tag{A.33}$$

$$F_{pduct2,jl} = \frac{i\omega L_{b2} b_{b2}}{4} Z_{duct2\_2,jl} \tag{A.34}$$

$$F_{p^+_{duct1},jl} = \frac{i\omega L_{b2} b_{b2}}{2} Z_{duct1\_2,jl} \tag{A.35}$$

$$F_{p_i} = L_{b2} b_{b2} j\pi e^{\frac{ik_0 L_{b2}}{2}} \frac{[1 - e^{j(-k_0 L_{b2} + j\pi)}]}{(j\pi)^2 - (k_0 L_{b2})^2} \tag{A.36}$$

REFERENCES

ANSI/IEEE Standard 176, Piezoelectricity (1978). New York.

Asdrubali, F., and Pispola, G. (2007). "Properties of transparent sound-absorbing panels for use in noise barriers," *the Journal of the Acoustical Society of America* **121**, 214-221.

Attenborough, K.(1983), "Acoustical characteristics of rigid fibrous absorbents and granular materials," *the Journal of the Acoustical Society of America* **73**,785-799.

Beyene, S., and Burdisso, R. A. (1997). "A new hybrid passive/active noise absorption system," *the Journal of the Acoustical Society of America***.101**, 1512–1515.

Bies, D.A., and Hansen, C.H. (1980). "Flow resistance information for acoustical design," *Appl. Acoust.***13**, 357-391.

Brennan, M.J., Elliott, S.J., Pinnington, R.J.(1997). "The dynamic coupling between piezoceramic actuations and a beam," *the Journal of the Acoustical Society of America***.102**, 1931-1942.

Champoux, Y and Allard, J.F. (1979). "Dynamic tortuosity and bulk modulus in air saturated porous media," Journal of Applied Physics **70(4)**,1975-1979.

Charette, F., Guigou, C., Berry, A. and Plantier, G. (1994). “Asymmetric actuation and sensing of a beam using piezoelectric materials”, *the Journal of the Acoustical Society of America***96(4)**,2272-2283.

Cheng, L., and Nicolas,J..(1992). “Radiation of sound into a cylindrical enclosure from a point-driven end plate with general boundary conditions,” *the Journal of the Acoustical Society of America***91** (3), 1504-1513.

Cheng, L., Li, Y.Y., and Gao, J.X. (2005). “Energy transmission in a mechanically-linked double-wall structure coupled to an acoustic enclosure,” *the Journal of the Acoustical Society of America***117**(5),2742-2751.

Chiu, M. C., and Chang, Y. C. (2008). “Numerical studies on venting system with multi-chamber perforated mufflers by GA optimization,” *Appl. Acoust.* **69**, 1017–1037.

Choy, Y.S., and Huang, L.X. (2002). ”Experimental studies of a drumlike silencer”, *the Journal of the Acoustical Society of America* **112(5)**, 2026-2035.

Choy, Y.S., and Huang, L.X. (2005). ”Drum silencer with shallow cavity filled with helium,” *the Journal of the Acoustical Society of America* **114(3)**, 1477-1486.

Choy, Y.S., Liu, Y., Cheung, H.Y, Xi, Q., and Lau, K.T.(2012). “Development of composite plate for compact silencer design,” *Journal of Sound and Vibration* **331,** 2348-2364.

Clark, R. L., Fuller, C. R. and Wicks, A.(1991). “Characterization of multiple

piezoelectric actuators for structural excitation," *the Journal of the Acoustical Society of America.* **90(1)**, 346-357.

Cobo, P., Fernández, A., and Doutres, O. (2003). "Low frequency absorption using a two-layer system with active control of input impedance," *the Journal of the Acoustical Society of America***.114**, 3211–3216.

Cobo, P., Pfretzschner, J., Cuesta, M., and Anthony, D. K. (2004). "Hybrid passive-active absorption using microperforated panels," *the Journal of the Acoustical Society of America***.116**, 2118–2125.

Cobo,P., M.Cuesta.(2007). "Hybrid passive-active absorption of a microperforated panel in free field conditions," *the Journal of the Acoustical Society of America***.121**, EL251–255.

Crandall, I.B. (1926). *Theory of Vibrating System and Sound*, Vam Nostrand, 229.

Crawley, E.F., and Luis, J.de (1987)."Use of piezoelectric actuators as elements of intelligent structures,"*AIAA J.* **25**,1373-1385.

Delany, M.E., and Bazley,E.N.(1970). "Acoustical properties of fibrous absorbent materials," *Applied Acoustics***3**,105-116.

Dimitriadis, E.K., Fuller, C.R. and Rogers, C.A. (1991). "Piezoelectric actuators for distributed vibration excitation of thin plates," *Journal of Sound and Vibration* **113** 117.

Doak,P.E.(1973).”Excitation, transmission and radiation of sound from source distributions in hard-walled ducts of finite length.I. The effects of duct cross-section geometry and source distribution space-time patteryn, ” *Journal of Sound and Vibration* **31**, 1-72.

Droltleff, H. and Zhou, X. (2001). “Attractive room acoustic design for multi-purpose halls,” *Acta Acust.* **87**, 500-504.

Du, G.H.,Zhu,Z.M.,and Gong,X.F., fundamental Acoustics. Nanjing University Press

Fahy,F. and Gardonio,P..(2007).Sound and structural radiation, transmission and response. Academic Press.

Fry, A.(1988), *Noise Control in Building Services*, Pergamon, Oxford.

Fuchs, H. V. and Zha, X. (1997). “Acrylic-glass sound absorbers in the plenum of the Deutscher Bundestag,” *Appl. Acoust.* **51**, 211-217.

Furstoss, M., Thenail, D., and Galland, M. A. (1997). “Surface impedance control for sound absorption: Direct and hybrid passive/active strategies,” *Journal of Sound and Vibration* **203**, 219–236.

Gentry, C.A, Guigou, C., and Fuller, C.R.(1996). “Smart foam for applications in passive-active noise radiation control,” *the Journal of the Acoustical Society of America***.101**(4), 1771-1778.

Guigou, C., and Fuller, C.R.(1999). “Control of aircraft interior broadband noise with foam-pvdf smart skin,” *Journal of Sound and Vibration.***220**, 541-557.

Guigou, C. and Fuller, C.R.(1998). ”Adaptive feedforward and feedback methods for active/passive sound radiation control using smart foam,” *the Journal of the Acoustical Society of America***.104**, 226-234.

Guigou, C., Berry, A., Charette, F., and Nicolas, J.(1996).”Active control of finite beam volume velocity using shaped PVDF sensor,” *Acustica.* **82**, 772-783.

Guo Y., Allam S. and Mats Åbom (2008). “Micro-perforated plate for vehicle applications,” Proceedings of the 2008 Congress and exposition of noise control engineering, Inter-Noise 2008, 26-29 Oct, Shanghai, China.

Gibbs, G.P., Fuller, C.R.(1992). “Excitation of thin beams using asymmetric piezoelectric actuator,” *the Journal of the Acoustical Society of America***. 96**, 3221-3227.

Guicking, D., and Lorentz, E. (1984). “An active sound absorber with porous plate,” *Trans. ASME, J. Vib.,Acoust., Stress, Reliab. Des*. **106**, 389–392.

Hansen, C.H., and Snyder, S.D.(1997). *Active control of sound and vibration*. Spon, London.

Huang, L.X. (1999), “A theoretical study of duct noise control by flexible panels”, *the*

Journal of the Acoustical Society of America **106(4)**, 1801-1809.

Huang, L.X. (2002), ”Modal analysis of a drumlike silencer”, *the Journal of the Acoustical Society of America* **112(5)**, 2014-2025.

Huang, L.X. (2006). ”Broadband sound reflection by plates covering side-branch cavities in a duct”, *the Journal of the Acoustical Society of America* **119(5)**, 2628-2638.

Ingard, U., and Pridmore-Brown, D. (1951), “The effect of partitions in the absorptive lining of sound attenuation ducts,” *the Journal of the Acoustical Society of America* **23**, 589-590.

Ingard, U.(1953). “On the theory and design of acoustic resonators”, *the Journal of the Acoustical Society of America* **25,** 1037-1061.

Ingard, K.U. (1994). *Notes on Sound Absorption Technology*, Noise Control foundation, U.S.A.

Johnson， D.L.,Koplik,J.,and Dashen,R.(1987).”Theory of dynamic permeability in fluid-saturated porous media,” *Journal of Fluid Mechanics***176**,379-402.

Kang, J. and Fuchs, H. V. (1999). “Predicting the absorption of open weave textiles and microperforated membranes backed by an air space,” *Journal of Sound and Vibration* **220**, 905-920.

Kim, H.-S., Hong, J.-S.,and Oh, J.-E. (1998). “Active noise control with active muffler

in automotive exhaust systems," *Noise Control Eng. J.* **41(2)**, 178-183.

Koshigoe, S., Mudock, J.W.(1993). "A unified analysis of both active and passive damping for plates with piezoelectric transducers," *the Journal of the Acoustical Society of America***. 93**, 346-355.

Lee J. (1992). "Compact sound absorbers for low frequencies," *Noise Control Engineering Journal* **38(3)**, 109-117.

Lee C.K., and Moon, F.C. (1990). "Modal sensors/actuators," *Journal of applied mechanics*. **57**, 434-441.

Lee, C.K. (1990). "Theory of laminated piezoelectric plates for the design of distributed sensors/actuators. Part I: Governing equations and reciprocal relationships," *the Journal of the Acoustical Society of America* **87(3)**, 1144-1158.

Lee, C.K., Chiang, W.W., and O'Sullivan, T.C.(1991). "Piezoelectric modal sensor/actuator pairs for critical active damping vibration control," *the Journal of the Acoustical Society of America***.90**, 374-384.

Lee, Y.Y. and Lee, E.W.M. (2007). "Widening the sound absorption bandwidths of flexible micro-perforated curved absorbers using structural and acoustic resonances," *Journal of Mechanical Sciences* **49**, 925-934.

Leroy, P., Atalla, N., Berry A. and Herzog, P.(2009). "Three dimensional finite element modeling of smart foam," *the Journal of the Acoustical Society of*

*America***.126**(6), 2873-2885.

Li, D. and Cheng,L. (2007).”Acoustically coupled model of an enclosure and a Helmholtz resonator array,” *Journal of Sound and Vibration* **305**, 272-288.

Lighthill. M.J. (1978). *Waves in Fluids*, Cambridge U.P., Cambridge.

Liu, F., Horowitz, S., N. Toshikazu, Louis N. Cattafesta, and Sheplak, M.(2003). “A tunable electromechanical Helmholtz resonator,” *AIAA*, 2003-3145.

Liu,F., Horowitz,S., Toshikazu, N., Louis, N., Cattafesta, Sheplak, M.(2007). “A multiple degree of freedom electromechanical Helmholtz resonator,” *the Journal of the Acoustical Society of America***.122**(1), 291-301.

Lueg,P.(1938). *United States Patent* 2,043,416.

Lung,T.Y.,and Doige,A.G.(1983).”A time-averaging transient testing method for acoustic properties of piping systems and mufflers with flow,” *the Journal of the Acoustical Society of America***.73**, 867-876.

Maa, D.Y. (1975). ”Theory and design of microperforated panel sound-absorption construction,” *Scientia Sinica* **18**,55-71.

Maa, D.Y. (1998). ”Potential of microperforated panel absorber,” *the Journal of the Acoustical Society of America* **104**, 2861-2866.

Masson F., Kogan P., Herrera G. (2008). “Optimization of muffler transmission loss by

using microperforated panels," FIA2008-A168.

Mechel, F.P. (1988). "Design charts for sound absorber layers," *the Journal of the Acoustical Society of America* **83**, 1002-1013.

Moretti, P.M..(2002). Modern vibrations primer. CRC press.

Munjal, M.L.(1987). *Acoustics of ducts and mufflers with application to exhause ventilation systemdesign*, John Eiley and Sons.

Nelson, P.A., and Eilliot, S. J.(1993). *Active control of sound*. Academic Press, London.

Petyt, M..(2010). Introduction to finite element vibration analysis. Cambrige University Press.

Plantier,G.,Guigou,C.,Nicolas,J., Piaud,B., and Charette, F. (1995). 'Variational analysis of thin beam excitation with a single asymmetric piezoelectric film, including bonding layer dynamical effects," *Acta acustica***3**(2),135-151

Proulx, B., and Cheng, L.(2000). "Dynamic analysis of piezoceramic actuation effects on plate vibrations," *Thin-walled Structures* **37**,147-162.

Putra, A and Thompson,D.J..(2010)."Sound radiation from perforated plates," *Journal of Sound and Vibration* **329**, 4227-4250.

Rayleigh (1929). *Theory of Sound*, Vol.**2**, MacMillan,323-487.

Sakagami, K., Morimoto, M., and Yairi M.(2009) "A note on the relationship between the sound absorption by microperforated panels and panel/membrane-type absorbers,"

*Applied Acoustics***70**,1131-1136.

Selament, A. and Lee, I. J. (2003). “Helmholtz resonator with extended neck,” *the Journal of the Acoustical Society of America* **113**, 1975-1985.

Sellen, N., Cuesta, M., and Galland, M. A. (2006). “Noise reduction in a flow duct: Implementation of a hybrid passive/active solution,” *Journal of Sound and Vibration* **297**, 492–511.

Seo, S.H. and Kim, Y.H. (2005). “Silencer design by using array resonators for low-frequency band noise reduction,” *the Journal of the Acoustical Society of America* **118**, 2332-2338.

St-Amant, Y., and Cheng, L.(2000). “Simulations and experiments on active vibration control of a plate with integrated piezoceramics,” *Thin-walled Structures* **38,** 105-123.

Takahashi, D. (1997). ”A new method for predicting the sound absorption of perforated absorber system,” *Applied Acoustics***51**, 71-84.

Takahashi D., Tanaka, M. (2002). ”Flexural vibration of perforated plated and porous elastic materials under acoustic loading,” *the Journal of the Acoustical Society of America* **112(4)**,1456-1464.

Tang, S.K. (2005). ”On Helmholtz resonators with tapered necks,” *Journal of Sound and Vibration* **279**, 1085-1096.

Wang, C. (1995). ”Timoshenko Beam-Bending Solutions in Terms of Euler-Bernoulli Solutions.” *Journal of Engineering Mechanics***121**(6), 763–765.

Wang, C.Q., Huang, L.X. (2007). ”Optimization of a clamped plate silencer”, *the Journal of the Acoustical Society of America* **121(2)**, 949-959.

Wang, C.Q., Cheng, L., and Huang, L.X. (2008). ”Realization of a broadband low-frequency plate silencer using sandwich plates”, *the Journal of Sound and Vibration* **318**, 792-808.

Wang, C.Q., and Huang, L.X. (2008). ”Analysis of absorption and reflection mechanisms in a three-dimensional plate silencer”, *the Journal of the Acoustical Society of America* **313**, 510-524.

Wu, M. Q. (1997). “Micro-perforated panels for duct silencing,” *Noise Control Eng. J.* **45**, 69-77.